The Structure and Dynamics of the Hurricane's Inner Core Region

By

Dennis J. Shea

Project Leader

William M. Gray

Department of Atmospheric Science
Colorado State University
Fort Collins, Colorado

Colorado State University

Department of Atmospheric Science

Paper No. 182

THE STRUCTURE AND DYNAMICS OF THE HURRICANE'S INNER CORE REGION

by

Dennis J. Shea

Preparation of this report

has been supported by

NOAA Grant N22-65-72 (G)

NSF Grant GA 19937

Principal Investigator: William M. Gray

Department of Atmospheric Science

Colorado State University

Fort Collins, Colorado

April 1972

Atmospheric Science Paper No. 182

FORWARD

This paper represents the research portion of Mr. Dennis Shea's M.S. thesis. Since coming to Colorado State University in September 1969, Mr. Shea has worked very diligently on this research topic. He has been supported on the principal investigator's NOAA and NSF Research Grants. He has had a substantial amount of subprofessional data reduction and other assistance.

This research represents part of a continuing research effort by the principal investigator with the RFF hurricane flight data which started in 1958 when I spent my first summer in Florida as a graduate student under the direction and encouragement of Professor Herbert Riehl. Since that time I have developed and maintained an ever growing belief in the ultimate validity and usefulness of the hurricane flight data, not only for describing the character of the inner hurricane circulation, but also for shedding light on the cumulus-broader scale flow interaction problem with applicability to other nonhurricane cumulus convective environments.

I have been appreciative of the open access to the NOAA Miami Hurricane data files which have been rendered me over the years and by the cooperation and friendliness of so many of the Hurricane Research personnel. I am particularly grateful to the help rendered me by the Research Projects' past and present directors, Drs. Robert H. Simpson, R. Cecil Gentry and Harry F. Hawkins.

Two important conclusions are emerging from the decade-and-a-half of research missions

(1) although the general structure and dynamics of the typical hurricane can be well specified by the flight data, large differences (in motion, radius of maximum winds, eye wall convection, asymmetry, etc.) exist between the separate storms. The individaul hurricane at separate time intervals typically has a complicated structure and dynamic character which is often substantially different from the mean hurricane circulation. We must better understand these differences if we are to continue in our efforts for better individual storm forecasting. We should not make generalizations on hurricane structure from a few individual case studies.

(2) the hurricane flight data, overall, appears to be of high quality. The observational quality cannot, however, be well judged by those who have worked only with some portions of data. Because the structure of each storm can be so different from the average, one must work with many of the storms over a long

period and make many instrumental and dynamical consistency checks, etc. before the data's limitations can be ascertained. Few researchers have had the interest or patience for this.

There is much more meaningful research which can be accomplished with the hurricane flight data. Only a small fraction of what can be done has been done. It would seem that the government's expenditure of many tens of millions of dollars in the aircraft data collection program over the last 15 years would justify continued or increased research support on the data evaluation both in the government and in the University.

William M. Gray
Department of Atmospheric Science
Colorado State University

ABSTRACT

Observational information from approximately 100 flight missions (533 radial legs) flown into twenty-one hurricanes on forty-one storm days over a thirteen year period by aircraft of the NOAA's Research Flight Facility is used to present a unified view of the structure, dynamics, and variability of the hurricane's inner core region. Most flight missions were made between the 900 and 500 mb levels.

Utilizing this information, a steady state schematic model of the mean flow conditions in the hurricane's inner core region is presented. The variability of the inner core meteorological parameters of wind speed, radius of maximum wind, inner radar radius and equivalent potential temperature is discussed. Wind-pressure acceleration balance information is shown. An estimate of the effect water motion has on the Doppler measured winds is made.

Results show that the maximum winds occur within the eye wall cloud area. The slope of the radius of maximum wind with elevation is shown to be small and a function of intensity. Analysis of the mean storm shows: i) wind shears are much smaller than the cylindrical thermal wind equation would indicate; ii) the strongest convergence and the largest ascending vertical motions are concentrated in a narrow region about the radius of maximum winds; iii) large subsidence occurs just inside the inner cloud wall; iv) maximum warming does not occur at the radius of maximum updraft, thus, the eye heating cannot be thought of as resulting from direct sensible temperature diffusion from the updrafts; v) in the lower half of the troposphere the maximum winds, regardless of Doppler wind correction, are almost always super-gradient; and vi) lapse conditions remain unstable in the inner cloud core area. Many other features are shown and discussed.

TABLE OF CONTENTS

SYMBOLS AND ABBREVIATIONS

Basic Physical Parameters

^{o}C - degrees celsius

f - coriolis parameter (sec^{-1})

g - acceleration of gravity

p - pressure (mb)

R - gas constant for dry air

T - adjusted temperature (^{o}C) - observed temperature after being adjusted to a constant pressure surface with typical hurricane lapse rates

Length

D - D-value (difference between the absolute altitude and the pressure altitude in feet)

km - kilometer

n. mi. - nautical mile

r - radius

Velocity

V_{θ} - actual tangential winds

$V_{\theta r}$ - relative tangential winds

V_{r} - actual radial winds (positive values indicate outflow; negative values indicate inflow)

V_{rr} - relative radial winds (positive values indicate outflow; negative values indicate inflow)

V_{max} - maximum wind

V_{min} - minimum wind

$\overline{V}$ - mean wind

Velocity Transport

$\overline{V_\theta' V_r'}$ - eddy transport of momentum

$\overline{V}_\theta \overline{V}_r$ - mean transport of mementum

Dynamic Symbols

DIV - divergence

KE - kinetic energy

M - absolute angular momentum

ζ_r - relative vorticity

Thermodynamic Symbols

θ_e - equivalent potential temperature (^oA)

Derived Symbols Used in the Study

RMW - radius at which the maximum wind occurs

IRR - inner radar eye radius

Miscellaneous

w. r. t. - with respect to

σ - standard deviation

x - exponent

Government and Project Symbols

NHRP - National Hurricane Research Project

NHRL - National Hurricane Research Laboratory

NOAA - National Oceanographic and Atmospheric Administration

RFF - Research Flight Facility

I. INTRODUCTION

Background

History. The National Hurricane Research Project (NHRP) was established in the middle 1950's at the instigation of Congress following the devastating flooding caused by hurricane Carol in the Connecticut Valley in 1954. Dr. Robert Simpson (present Director of the National Hurricane Center) was the driving force behind the initial organization and functioning of the NHRP as it was then called[1]. The first flights were accomplished in late 1956. Except for the year 1959 (during the change over from Air Force to civilian aircraft) an almost continuous monitoring of the hurricane by the Weather Bureau's (now NOAA's) Research Flight Facility (RFF) was accomplished in the decade from 1956 through 1966. From 1966-67 onward the interest of NOAA has steadily shifted to hurricane modification and the typical radial or cloverleaf flight patterns have been modified.

Character of Flight Missions. From 1957 through 1966 the majority of flight missions were flown into the hurricane eye and out again. This was repeated at individual flight levels four to six times with a rather even balance between the storm quadrants. Figs. 1a-h show several typical flight patterns. Most of these flights in and out of the hurricane occurred at inner radii of less than 100 nautical miles (n. mi.). Voluminous data is available from the center to the 50-60 n. mi. radius.

---

[1] In 1960 the name was changed to the National Hurricane Research Laboratory (NHRL).

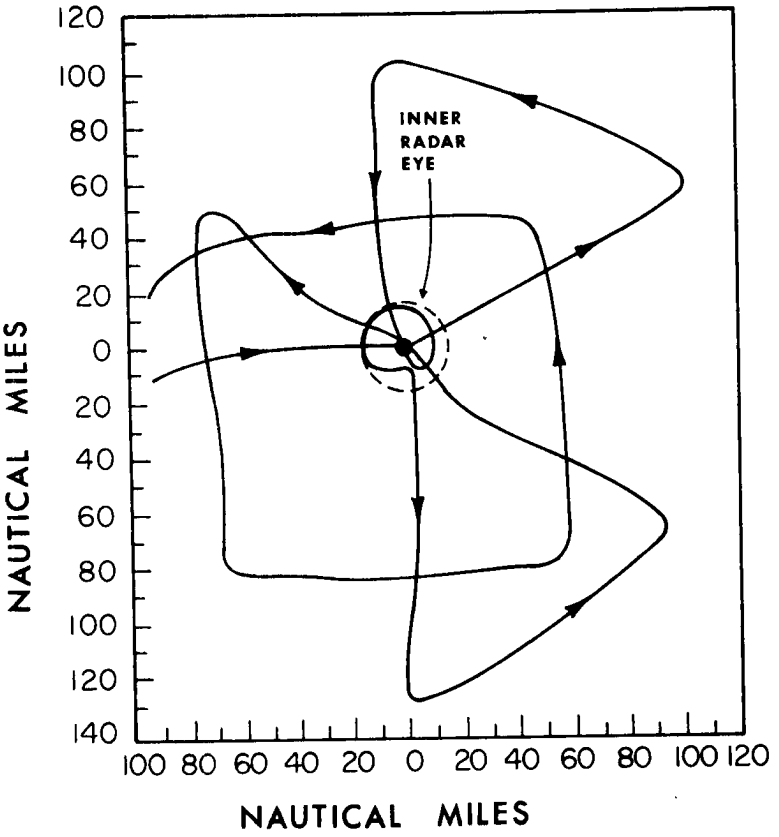

Fig. 1a. Cleo 18 Aug. 1958 560 mb.

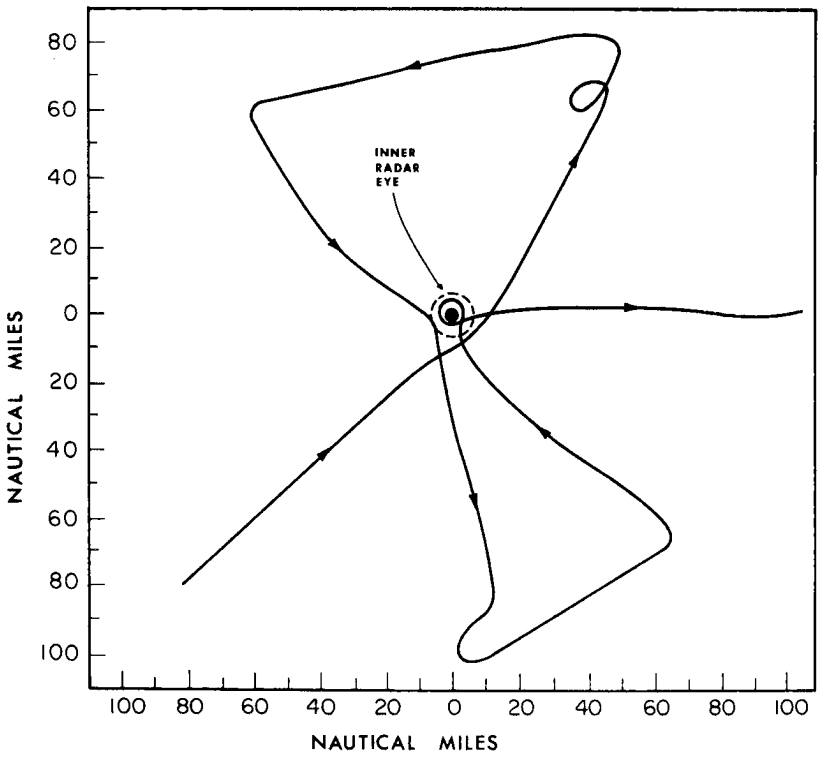

Fig. 1b. Daisy 27 Aug. 1958 620 mb.

Figs. 1a-h. Typical flight patterns.

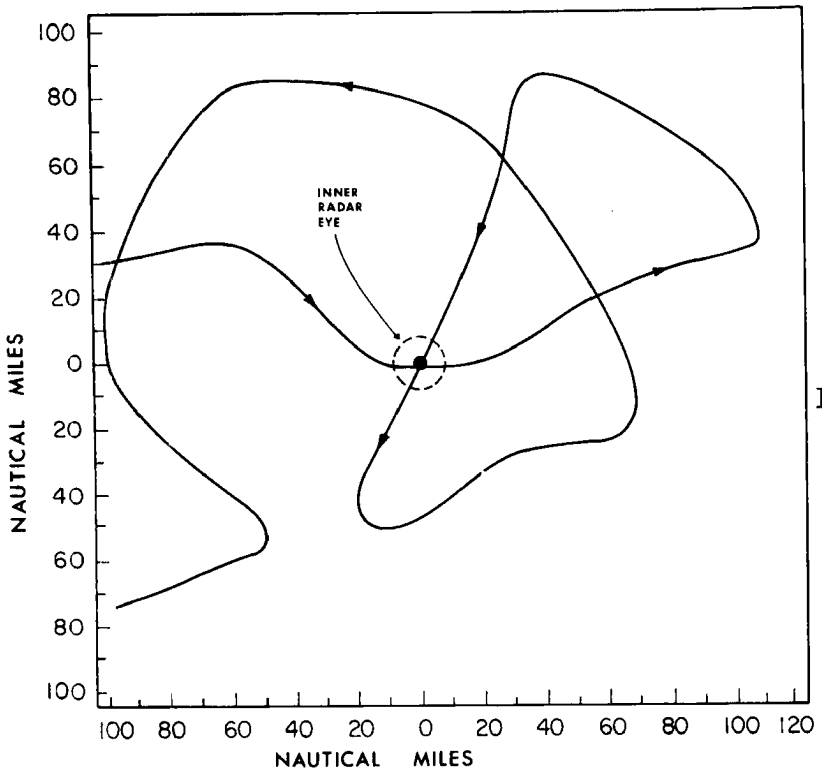

Fig. 1c. Helene 26 Sept. 1958 250 mb.

Fig. 1d. Carla 10 Sept. 1961 600 mb.

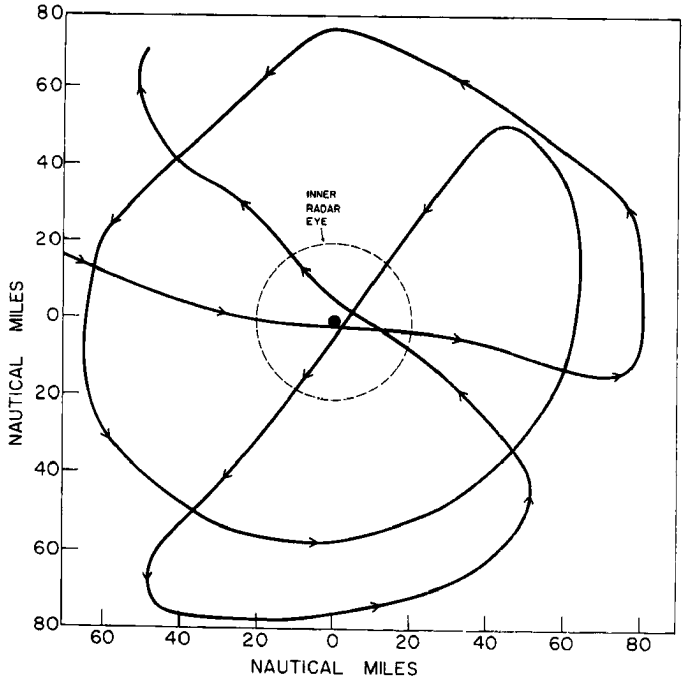

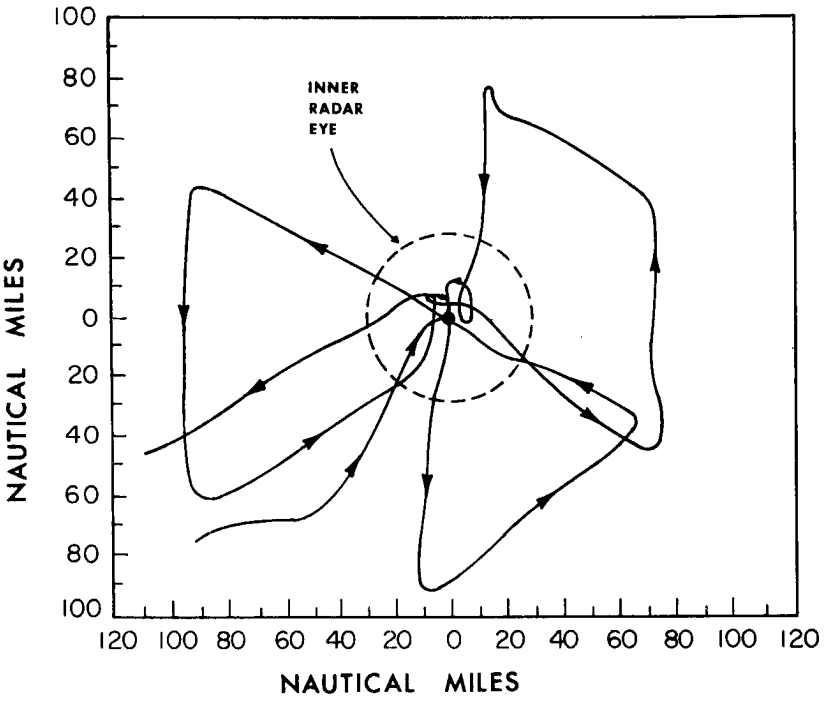

Fig. 1e. Ella 19
Oct. 1962
900 mb.

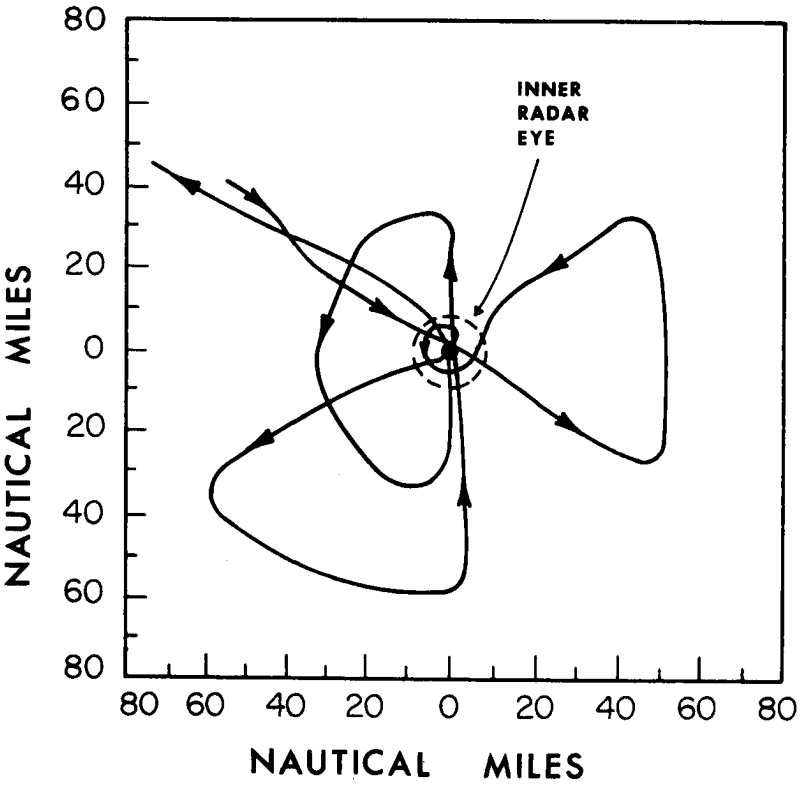

Fig. 1f. Hilda 10
Oct. 1964
500 mb.

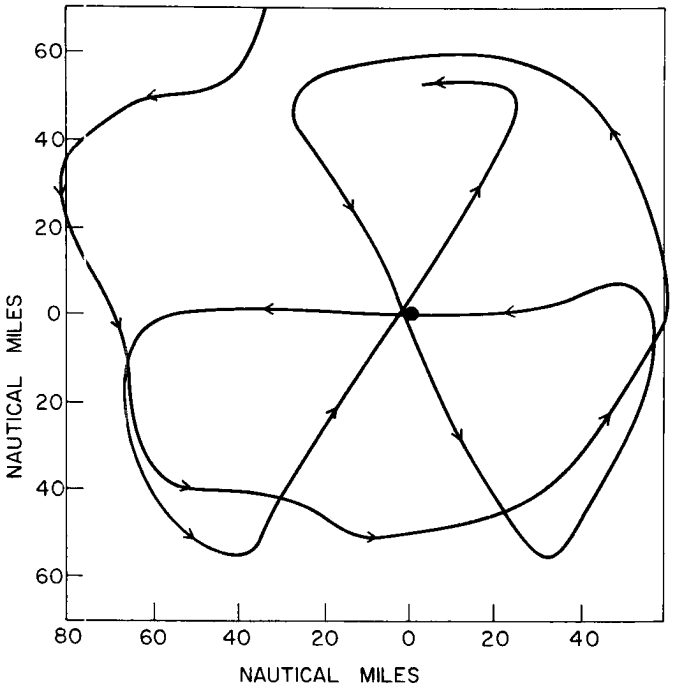

Fig. 1g. Betsy 3
Sept. 1965
500 mb.

Fig. 1h. Inez 27
Oct. 1966
750 mb.

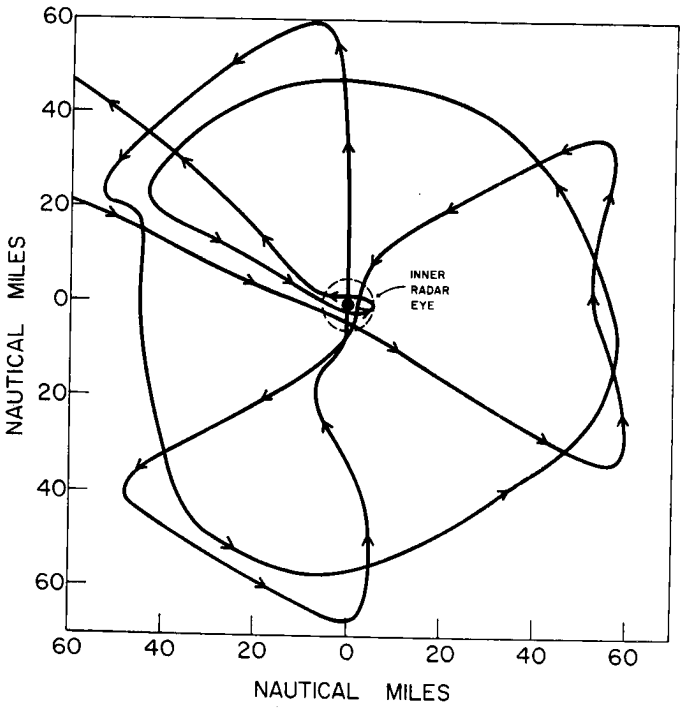

Beyond this radius the quantity of flight data drops off. A small sample of individual radial legs[2] from two different layers (900 to 700 mb and 700 to 500 mb) have been superimposed to illustrate this (See Figs. 2 and 3).

The data has been gathered by prop aircraft (B-50's from 1956 through 1958, and DC-6's from 1960 to the present). This has restricted operations to below the 500 mb level. Also, due to safety restrictions on low level flight missions most of the data was taken above 900 mb. In this tropospheric range from 500 to 900 mb there have been approximately 700-800 radial legs flown. Of these, the processed reliable data at this time comes to 492 radial legs.

Upper tropospheric sampling was accomplished between the 180 and 260 mb levels by B-47 aircraft in 1957 and 1958 and by a B-57 after 1960. The number of B-57 flights has not been large because of range and instrumental difficulties. For this reason there are only 11 evaluated upper level missions (41 radial legs).

Combining upper and lower levels there are 533 radial legs. This report concentrates on the flight data between the 500 and 900 mb levels.

Character of the Measurements

Winds and Pressure. The perfection of the Doppler navigation instrument in the mid-1950's and the simultaneous measurement of

[2] A radial leg is the portion of the plane's flight pattern during which the plane was flying directly into or out of the storm center. For example, the flight pattern shown in Fig. 1a has six radial legs.

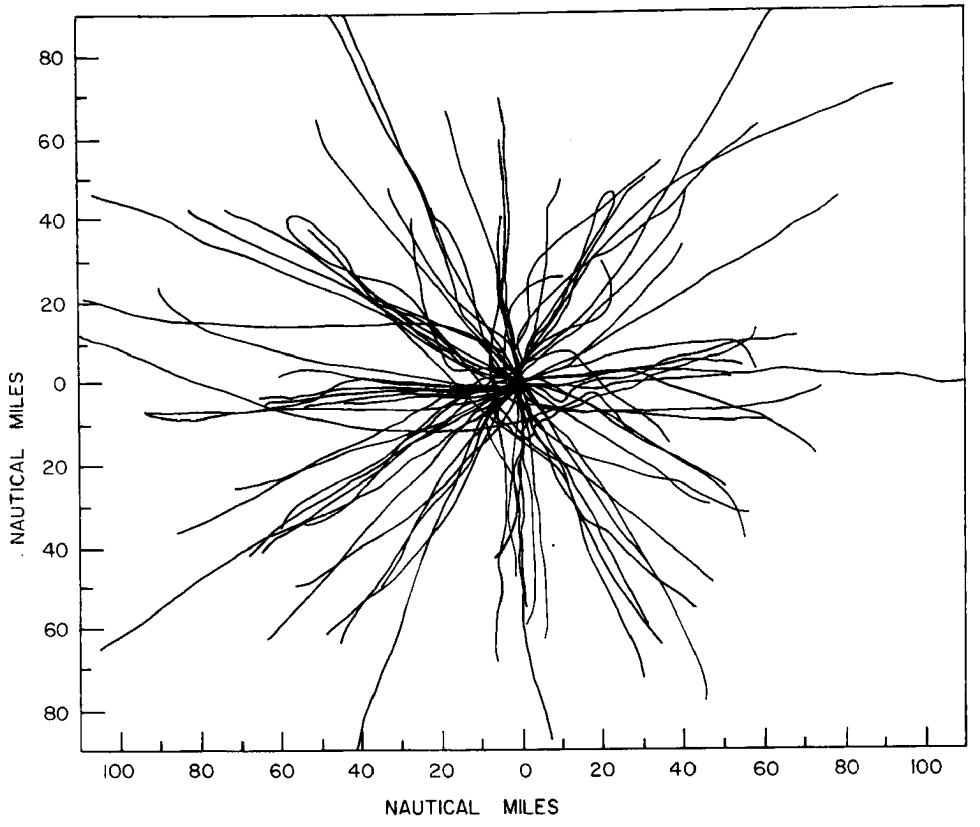

Fig. 2. Small sample of superimposed individual radial legs for the 900-700 mb layer.

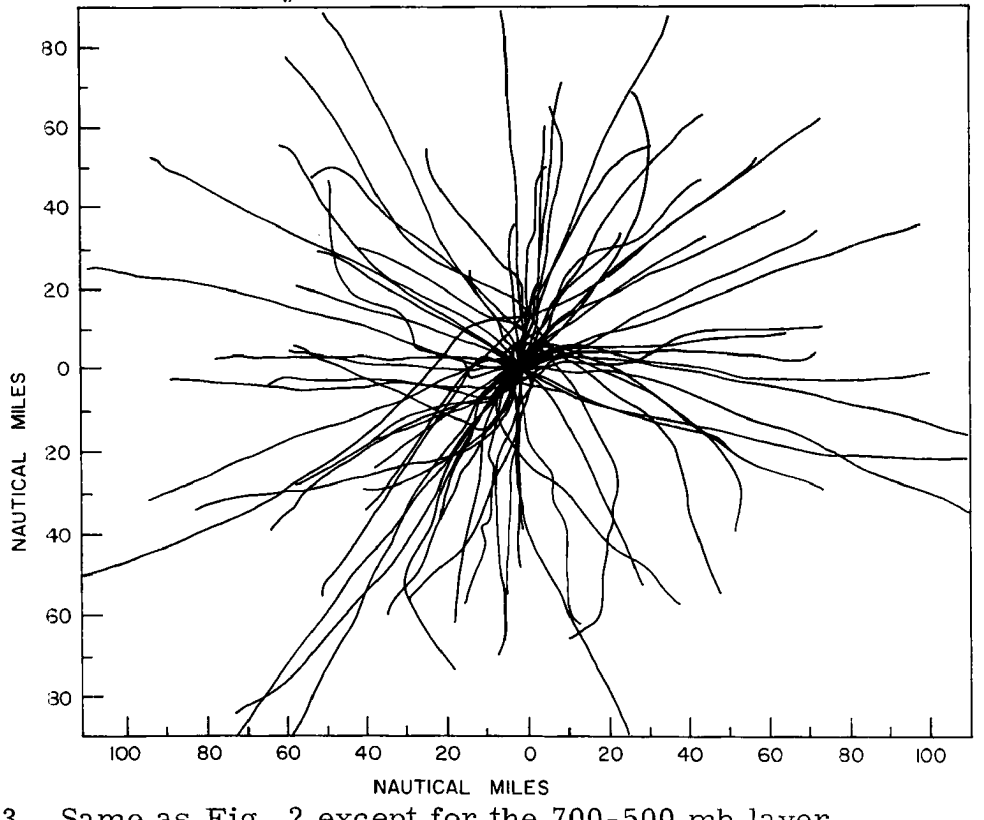

Fig. 3. Same as Fig. 2 except for the 700-500 mb layer.

pressure and absolute altitude (possible over water where terrain features do not interfere) have allowed accurate wind and D-value[3] measurements down to the cumulus scales of motion.

Doppler wind measurements are much more reliable in high wind conditions where the noise to signal ratio is much smaller than in weak wind conditions. The general validity of these Doppler determined winds has been demonstrated on many occassions when navigation errors after many hours of flight proved to be but a few nautical miles.

Temperature. The vortex temperature measurements have shown a very strong reliability. It is possible to obtain an independent check on the observed inward radial temperature gradients by measurement of the pressure level thickness changes when simultaneous double level missions were flown. When compared the hydrostatically calculated temperature gradients and the directly measured temperature gradients proved to be quite close.

Processing of Data. Only in the last few years has this complete set of processed and checked flight data become available. The data reducing, cross checking, navigation corrections, hydrostatic consistency checks, etc., that had to be made have required a rather lengthy and painstaking evaluation procedure. This large data sample is now available for close scrutiny.

---

[3]The D-value is the difference between the absolute altitude and the pressure altitude (in the mean tropical atmosphere).

Purposes of Study

Storm Variability. Perhaps the most outstanding characteristic of hurricanes is the large variability of conditions in their inner core[4] area. Not only is one storm different from another (e.g., intensity, asymmetries, storm motion, etc.) but day to day and even hour to hour changes in the individual storm's inner core are frequently substantial. Fig. 4 presents a small sample of observed tangential wind profiles. Note the differences. Some profiles exhibit sharp peaks, whereas others show a slow increase to the maximum wind and then a flat profile.

Obviously, results drawn from individual storm case studies [e.g., Staff, NHRP (1958), Jordan, et al. (1960), Colón and Staff (1961), Riehl and Malkus (1961), Miller (1962), LaSeur and Hawkins (1963), Colón (1964), Sheets (1967a, 1967b, 1968), and Hawkins and Rubsam (1968a, 1968b, 1968c)], may not necessarily be representative of the majority of storms. Generalizations of typical hurricane dynamics from individual storm data can be misleading. Yet, most of our hurricane concepts have come from individual storm evaluations.

The primary purpose of this research is to utilize the large amounts of aircraft observations collected by the Hurricane Project in order to present a unified view of the structure, dynamics and

---

[4]The term inner core refers to the inner 50 n. mi. of the hurricane. This region includes (1) the area of high winds, clouds, and intense vertical motions and (2) the calmer, clearer area inside (i. e., the eye).

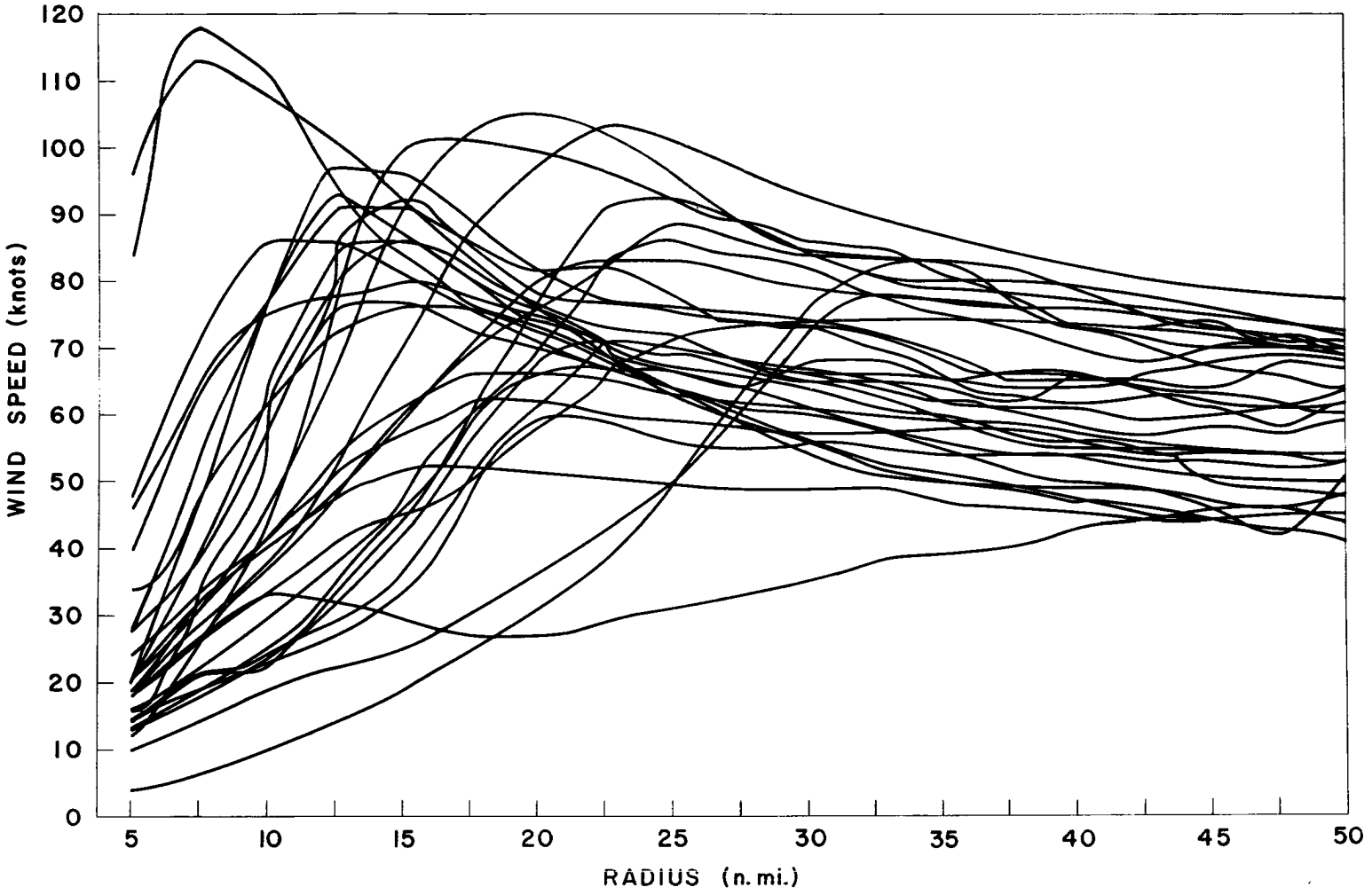

Fig. 4. Sample of observed tangential wind profiles.

variability of the hurricane's inner core region. This portion of the storm is of special interest because of its potential destructiveness and its concentration of cyclone dynamics.

Cumulus Scale-Broader Scale Flow Interaction. The eye wall or inner core area of the hurricane has the highest concentration of cumulus and cumulonimbus activity that is to be found in the earth's atmosphere. Perhaps by using this large data sample available for the convective inner core region it will be possible to improve our understanding of cumulus convection and its interaction with the broader-scale flow. We may then be able to throw light on what the individual clouds are doing to the broad scale and vice versa. Even though the eye wall cumulus density is higher than anywhere else, so too are wind and pressure accelerations. The ratio of cumulus convection to wind-pressure accelerations may not be so different in the inner hurricane core as in other areas where both cumulus convection and wind pressure accelerations are less.

The second purpose of this study, then, is to use the hurricane data to obtain information on cumulus convection and its interaction with the broader scale. It is hoped that this information will have a degree of applicability to the general problem of effects of cumuli on other scales of atmospheric motion.

II. DATA COLLECTION AND ACCURACY

Data

Discussions of the instruments and aircraft used to obtain the meteorological data of this study have been made by Hilleary and Christensen (1957), Hawkins et al. (1962), Gray (1962, 1965a, 1965b, 1966, 1967), Gentry (1964), Reber and Friedman (1964) and Friedman et al. (1969). For detailed descriptions of the instruments and the character of the data collected the reader is referred to these reports.

After a flight into a storm has been completed, the raw data is composited with respect to the moving storm center by computer. This data is processed and the computer prints out the plane's distance from the storm center, the actual tangential wind (V_θ), the actual radial wind (V_r), the relative tangential wind ($V_{\theta r}$), the relative radial wind (V_{rr}), and the D-value (D) and the adjusted temperature (T) at that radius. The actual winds include the effects of storm motion whereas the relative winds have had the storm motion subtracted from the data. The adjusted temperature is the observed temperature adjusted to a constant pressure surface using typical hurricane lapse rates.

This study does not treat the humidity measurements. Nevertheless, an estimate of the effect a virtual temperature correction would have on observed temperatures and temperature gradients has been made and is discussed in section III.

This data is unique in that we have simultaneous wind, temperature and pressure measurements down to the cumulus scale. Over land, where terrain features obscure D-value measurements, this is not possible. The simultaneous pressure and wind measurements allow examination of radial wind and pressure balances. Where double level flights were made, an examination of the cylindrical thermal wind balance can be made.

Data Errors. In general, the final processed data is quite reliable. Two non-instrument factors can contribute to errors in the wind reports, however. These are (1) positioning of the aircraft relative to the storm center and (2) water motion under the aircraft.

The positioning of the aircraft is quite important. Hawkins and Rubsam (op. cit.) have discussed the sensitivity of the radial winds to the aircraft's position to the storm center. They note that even small changes in position can result in significant changes in the radial winds. Thus, along individual radial legs the radial winds are believed to be only marginally acceptable. If these positioning errors are random, however, a large data sample will tend to average them out. The mean radial wind data should then be acceptable.

The AN/APN-82 Doppler Navigation system is used to determine the motion of the aircraft relative to the ocean. The wind speed is obtained from the vector difference between the true airspeed and the aircraft motion relative to the ocean. Because the aircraft measurements were made over the ocean which moves under wind stress, the

Doppler winds have been suspected of underestimating the true wind speeds by 5-10 percent [Grocott (1963), Gray (1967)] and upwards to 20% by Black et al. (1967). The observational evidence of this paper supports the former estimates of only 6-7% water motion.

Temperatures are measured with a vortex thermometer which requires no dynamic correction. Comparison of the observed vortex temperature gradients with those calculated from flight D-value thickness gradients (using the hydrostatic equation) show a strikingly close similarity. For this reason the radial temperature gradients and D-value gradients are felt to be quite accurate. (See Appendix II).

Data Available. All the fully processed and checked reconnaissance data from the hurricane flights of 1957 to 1969 has been gathered. Table 1 lists the twenty-one hurricanes[5], the forty-one storm days, the number of radial legs (total - 533), the pressure levels at which the data was collected, the maximum actual winds at flight levels, the central pressures, etc., for the storms used in this study.

The data was collected on days when storms were deepening and filling and while the storms were in a quasi-steady state. The combined data sample is felt to be large enough to assume a steady-state condition.

Besides the information listed in Table 1 several other types of information were recorded. These include time interval during which

---

[5]Hurricane Hannah's data of 1959 was obtained by Air Force research planes.

TABLE 1. Storms, dates, levels, etc., used in this study. The letters following the inner radar eye are: A - approximate, WD - well defined, P - poor.

STORM	DATE	LAT.	MOTION DIR/SPD (Kts)	INTENSITY CHANGE	CENTRAL PRESS. (mb)	MAX. WIND (Kts)	(RAD OF MAX. WINDS)	INNER RADAR EYE RADIUS	APPROX. FLIGHT LEVEL (mb)	NO. OF RADIAL LEGS
CARRIE	15 Sept. 57	30	310/11	Steady	963	80	(22)	--	610	6
						84	(22)	--	525	4
						54	(35)	--	240	2
	17 Sept. 57	35	65/8	S	978	84	(32)	25A	680	6
						42	(47)	25A	240	6
CLEO	18 Aug. 58	33	15/13	S	972	86	(22)	17	800	6
						82	(22)	17	560	6
						49	(50)	17	240	5
DAISY	27 Aug. 58	29	25/5	Deepening	942	109	(10)	6	620	6
		"			943	69	(10)	6	250	4
	28 Aug. 58	33	0/17	Filling	950	101	(20)	--	620	6
HELENE	25 Sept. 58	29	335/6	D	982	76	(27)	15	800	6
	26 Sept. 58	30	315/9	D	948	99	(25)	9	800	8
						97	(20)	9	700	1
						119	(15)	9	560	5
						81	(12)	9	250	4
HANNAH	01 Oct. 59	31	335/11	S	959	95	(20)	--	700	4
	02 Oct. 59	34	75/8	S	959	96	(22)	--	700	4
	04 Oct. 59	37	85/10	S	955	108	(30)	--	700	6
DONNA	04 Sept. 60	17	290/15	S	952	120	(12)	--	600	2
	07 Sept. 60	22	270/9	S	935	129	(22)	10-13WD	760	4
						128	(15)	13WD	620	4
	09 Sept. 60	23	305/10	S	930	131	(15)	--	800	2
ANNA	21 July 61	13	280/16	S	983	98	(12)	--	700	9
CARLA	08 Sept. 61	23	300/6	D	964	98	(32)	31WD	850	4
						96	(35)	31WD	700	4
	09 Sept. 61	24	310/8	D	948	109	(22)	21WD	850	4
						111	(17)	21WD	850	4
						94	(22)	22WD	700	4
	10 Sept. 61	27	300/8	S	940	96	(20)	20A	600	6
	11 Sept. 61	28	340/6	S	940	102	(15)	--	600	4
ESTHER	16 Sept. 61	23	295/13	D	935	128	(12)	10A	800	8
						109	(12)	10A	470	9
						106	(12)	10A	470	5
	17 Sept. 61	24	300/10	S	940	112	(10)	--	800	5
						108	(10)	--	800	2
						108	(10)	--	800	3
ELLA	19 Oct. 62	31	65/8	D	966	102	(30)	30	900	8
						89	(40)	30	600	8
BEULAH	23 Aug. 63	21	340/8	D	962	82	(17)	13	800	5
	24 Aug. 63	24	350/7	F	961	100	(25)	13A	800	10
						108	(20)	13A	520	13
FLORA	03 Oct. 63	17	330/9	D	936	135	(8)	8-9	700	14
						122	(10)	8	650	12
	10 Oct. 63	28	50/25	S	970	117	(42)	25	700	12
						101	(50)	25	650	15
CLEO	23 Aug. 64	17	275/12		--	133	(7)	--	700	13
					--	126	(7)	--	650	16

(continued)

TABLE 1. (continued)

STORM	DATE	LAT.	MOTION DIR/SPD (Kts)	INTENSITY CHANGE	CENTRAL PRESS. (mb)	MAX. WIND (Kts)	(RAD OF MAX. WINDS)	INNER RADAR EYE RADIUS	APPROX. FLIGHT LEVEL (mb)	NO. OF RADIAL LEGS
DORA	05 Sept. 64	24	320/10	D	966	98	(27)	8-15	700	7
					960	95	(25)	18	600	6
	07 Sept. 64	28	285/10	S	963	75	(25)	14	700	6
					960	89	(50)	14	700	8
					960	88	(25)	14	650	16
	08 Sept. 64	29	285/12	S	963	88	(35)	17P	700	4
					962	82	(40)	14	650	2
	09 Sept. 64		280/10	S	965	82	(42)	25A	860	5
						80	(35)	25A	700	6
						69	(30)	25A	600	2
GLADYS	17 Sept. 64	24	300/9	S	954	111	(12)	13	900	6
					950	102	(15)	13	700	4
					945	107	(15)	13	700	2
			300/10		945	105	(15)	13	560	4
HILDA	01 Oct. 64	24	310/5	D	950	110	(12)	10	900	4
					947	109	(12)	7-9	750	5
					950	90	(15)	7	650	4
						90	(12)	9	500	7
		24	310/5			47	(15)	9	180	2
	02 Oct. 64	26	0/5	F	956	103	(20)	9	900	4
						89	(35)	9	700	2
						93	(40)	9	650	4
						50	(27)	9	200	2
ISBELL	14 Oct. 64	24	35/11	S	970	108	(10)	13	850	6
						102	(12)	13	700	7
						87	(20)	13	570	1
BETSY	03 Sept. 65	25	315/10	S	952	98	(22)	13-28	750	6
						100	(25)	10-15	650	6
						91	(17)	10	500	6
						56	(37)	10	200	4
	05 Sept. 65	29	180/3	F	973	93	(37)	28	900	2
					968	75	(40)	10	800	2
		25				72	(37)	10	650	2
		29			970	57	(22)	10	500	4
						47	(42)	10	200	4
INEZ	27 Sept. 66	16	275/10	D	962	108	(5)	5	750	6
						104	(7)	5	650	6
					971	74	(12)	5	500	6
					962	46	(25)	5	200	4
INEZ	28 Sept. 66	17	275/12	D	934	142	(5)	4	950	6
					928	150	(7)	7	750	6
					934	126	(7)	4	650	6
			275/14		930	137	(7)	7	500	5
					934	67	(15)	7	200	4
BEULAH	18 Sept. 67	22	295/11	D	967	78	(12)	7	950	4
						80	(20)	7	850	4
DEBBIE	18 Aug. 69	24	300/1	S	971	93	(22)	--	650	4
	20 Aug. 69	25	305/11	S	950	99	(22)	--	650	4
					954	99	(12)	--	650	4
TOTAL	21	41							97	533
MEAN		25								

the data was obtained, the ground track of the aircraft, the octant in which the aircraft was flying both with respect to (w.r.t.) geographic north and w.r.t. storm motion, and whether the plane was flying towards or away from the storm center.[6] A sample listing of this information for an individual radial leg is included in Appendix I.

Although the wind, pressure, and temperature data were recorded every few hundred meters, it was decided that the very small scale data fluctuations should be smoothed out. This was accomplished by printing out information from five to fifty nautical miles (n. mi.) from the storm center using a 2.5 n. mi. overlapping data interval. This interval was felt to offer enough horizontal resolution for the purposes of this study.

Contained in the data sample are twenty storm days on which simultaneous multilevel flights were made.[7] These are listed in Table 2. Examination of these flights will allow a check of the vertical wind shears and the degree of cylindrical thermal wind balance. Gray (1967) has used a smaller and earlier data sample of these double level flights to check this balance. He noted that even with the large baroclinicity

---

[6]This allowed investigation of the data to see if individual parameters exhibited any systematic differences between data gathered by inward penetration as opposed to outward penetration of the eye wall. Appendix III shows that there are no systematic differences.

[7]In order to be used, each flight level was required to have at least four approximately equally spaced radial legs and the data at each level had to be taken within a reasonable time interval of each other i.e., 5-6 hours. This greatly reduced the number of usable double level flights.

TABLE 2.

Storms, dates and flight levels for the 20 storm days on which multilevel flight missions were made.

Storm	Date	Approximate Flight Levels (mb)
Carrie	15 Sept 1957	610, 525
	17 Sept 1957	680, 240
Cleo	18 Aug 1958	800, 560, 240
Daisy	27 Aug 1958	620, 250
Helene	26 Sept 1958	800, 560, 250
Donna	7 Sept 1960	760, 620
Carla	8 Sept 1961	850, 700
	9 Sept 1961	850, 700
Beulah	24 Sept 1963	800, 520
Flora	3 Oct 1963	700, 650
	10 Oct 1963	700, 650
Dora	5 Sept 1964	700, 600
	9 Sept 1964	850, 600
Gladys	17 Sept 1964	900, 700, 560
Hilda	1 Oct 1964	750, 650, 500
Isbell	14 Oct 1964	850, 700
Betsy	3 Sept 1965	750, 650, 200
	5 Sept 1965	500, 200
Inez	27 Sept 1966	750, 650, 500, 200
Beulah	18 Sept 1967	950, 850

in the core region the vertical wind shears were much smaller than the cylindrical thermal wind equation would indicate. Based upon this finding he has hypothesized that the role of vertical transfer of horizontal momentum by the cumuli is fundamental in producing an 'unbalanced' larger baroclinicity than vertical wind shear within the eye wall region. This lack of thermal wind balance is believed to be of fundamental importance in the hurricane's growth. This larger data sample allows a better check on the degree of thermal wind imbalance in existence.

Distribution of Data. Originally it had been hoped that enough flight data (perhaps 300 radial legs) would be available to allow the construction of a two level (lower and upper) and a three level (low, middle and upper) 'mean storm'. An examination of Table 1 shows that we have more than exceeded this original estimate. As a result it was decided to build a five level mean storm, in addition to, the two and three level mean storms. This allowed for a much better vertical storm resolution. Fig. 5 shows the manner in which the data was combined by levels. The number of radial legs at each level and the pressure level which the data best represents is indicated.

Using this information a five level mean asymmetric storm was built. Fig. 6 shows the distribution of radial legs by octant. Several of the octants contained only a few radial legs. In order to increase the amount of data in each octant it was decided that the individual octant data at each level should be combined with the data in each

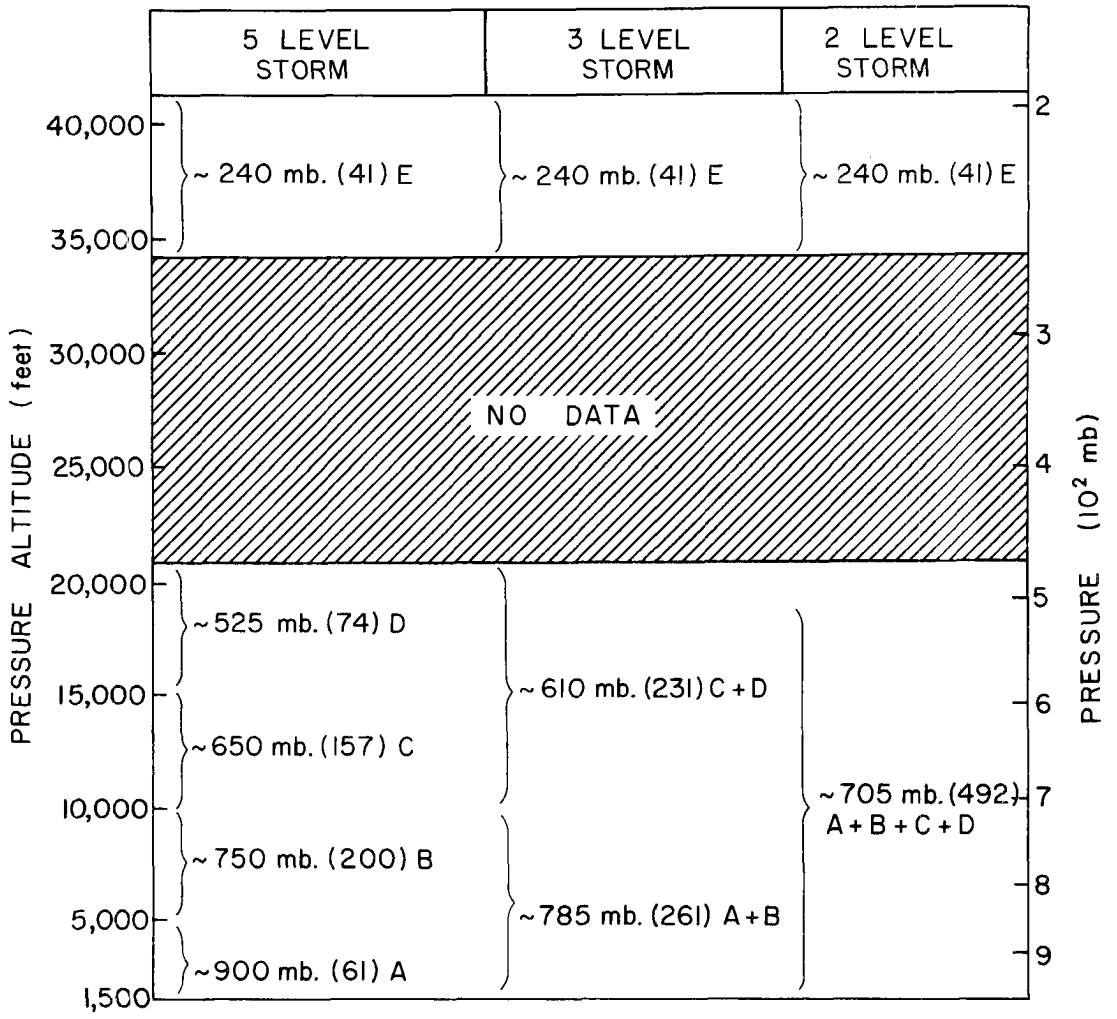

Fig. 5. Distribution of radial leg data in the vertical for the five, three and two level mean storms. The number in parenthesis is the number of radial legs in each layer average. The pressure level is the level which the data best represents.

adjacent octant. For example, in Fig. 6 the four radial legs in octant 1 of the 1500' to 5000' data would be combined with the radial leg data in octants 2 and 8 making a total of 22 octant radial legs. The data in octant 2 would be combined with the data in octants 1 and 3, etc. This overlapping technique will slightly underestimate the degree of asymmetry in the mean asymmetric storm, but should make the data more representative.

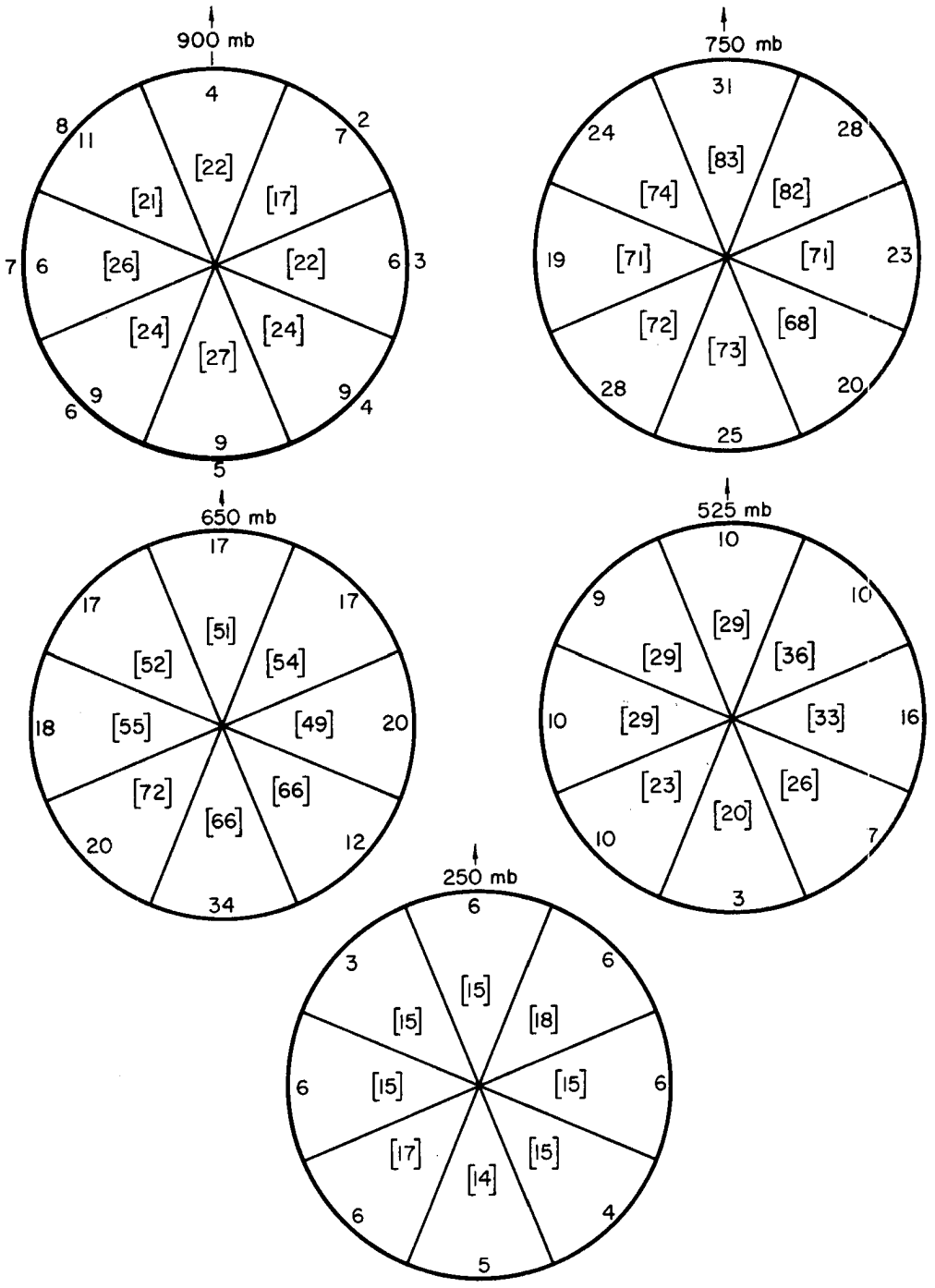

Fig. 6. Distribution of radial legs by octant. The number without brackets represents the raw number of radial legs in each octant for each level. The number with brackets represents the overlapping average where radial legs in the surrounding two octants has been included.

Compositing Methods

The data compositing was accomplished in two ways:

Method I consisted of compositing data and performing dynamic calculations with respect to (w.r.t.) the Radius of Maximum Wind (RMW). This method is illustrated in Fig. 7 using tangential wind profiles from five different storms.

Method II consisted of arranging all the data and dynamic calculations w.r.t. the absolute radius. This method is illustrated in Fig. 8.

Method I has the advantage of allowing the dynamics of the region outside the RMW[8] to be separated from the region inside the RMW. This is necessary because the two regions are dynamically quite different. At and outside the RMW convergence and high winds are present. Inside the RMW, high vorticity values, divergence and subsidence are present. In general, compositing method I has more physical relevence for understanding the hurricane's inner core dynamics. Most of the data presentations which follow were made by use of method I. Dynamic calculations involving the radius are, of course, always made before compositing w.r.t. the RMW.

---

[8]The expressions "inside the RMW" and "outside the RMW" will be used throughout this report. The former expression refers to radii less than the RMW (e.g., RMW - 5n.mi., RMW - 10 n.mi., etc.). The latter expression refers to radii larger than the RMW (e.g., RMW + 5 n.mi., RMW + 10 n.mi., etc.).

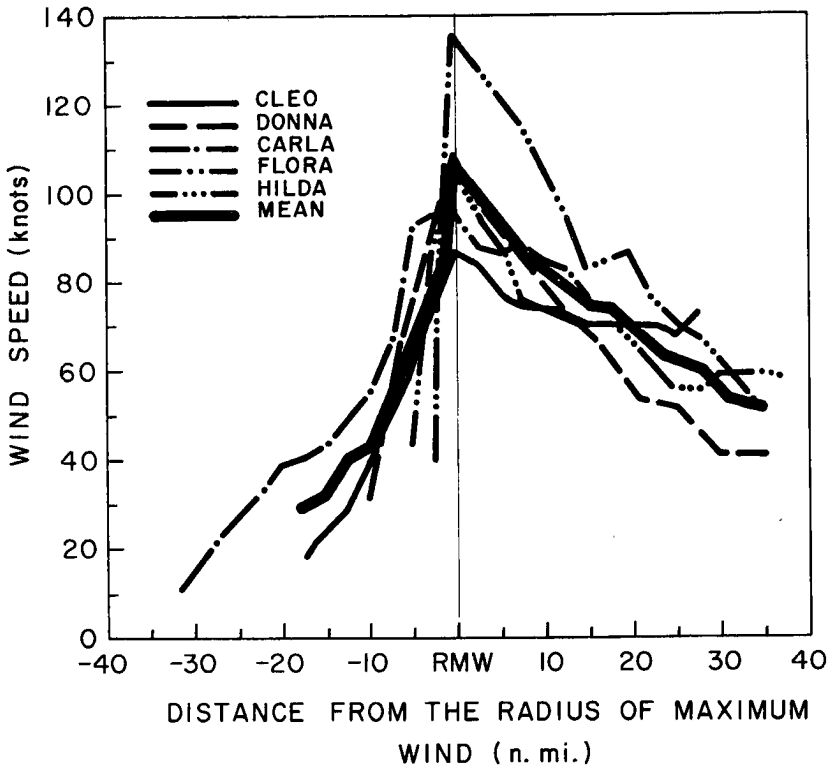

Fig. 7. Illustration of compositing method I where data is averaged with respect to the Radius of Maximum Winds (RMW).

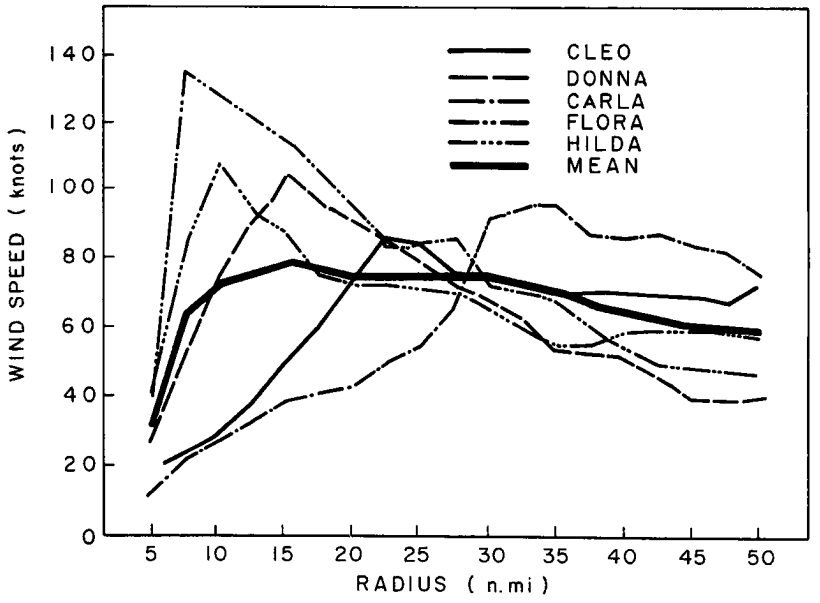

Fig. 8. Illustration of compositing method II where the data is averaged with respect to the absolute radius.

III. STRUCTURE AND DYNAMICS OF THE MEAN SYMMETRIC STORM

Structure with Respect to the Radius of Maximum Wind

The structure of the mean symmetric storm obtained by compositing parameters w.r.t. the radius of maximum wind (method I) will now be discussed. At least twenty radial legs were required for a point to be plotted.

Tangential Winds. Radial profiles of the mean tangential wind are shown in Figs. 9-13 for each of the five levels. The similarity of the wind profiles in the lower half of the troposphere should be noted (See Fig. 14). All exhibit sharp peaks at the RMW and show large anticyclonic shears outside the RMW. A vertical cross section of the tangential winds (Fig. 15) shows that the winds decrease with height, but the decrease is much smaller than one would expect from the cylindrical thermal wind relationship - in agreement with the findings of Jordan (1958b), Hawkins (1962) and Gray (1967). The mean wind profile and standard deviation for the whole 900 to 500 mb layer is shown in Fig. 16.

Radial Winds. Radial wind profiles are shown in Figs. 9-12. The lowest layer exhibits inflow from the outer regions into the area around the RMW. The magnitude of this inflow is largest at distances far from the RMW and decreases sharply as the RMW is approached. Inside the RMW we have outflow. Thus, in the lowest layer at and

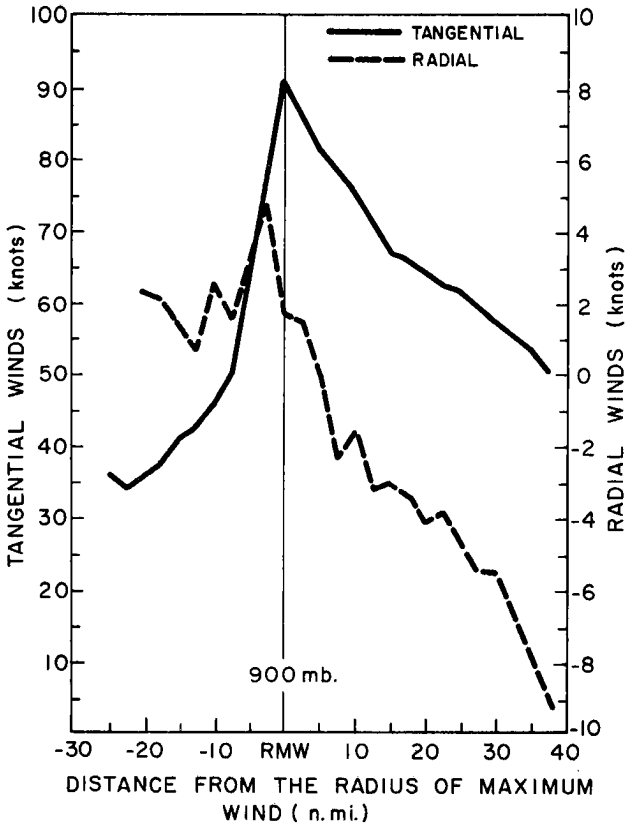

Fig. 9. Tangential and radial wind profiles for the mean symmetric storm averaged with respect to the Radius of Maximum Wind ($\overline{RMW}$) at 900 mb (method I). Positive radial winds indicate outflow.

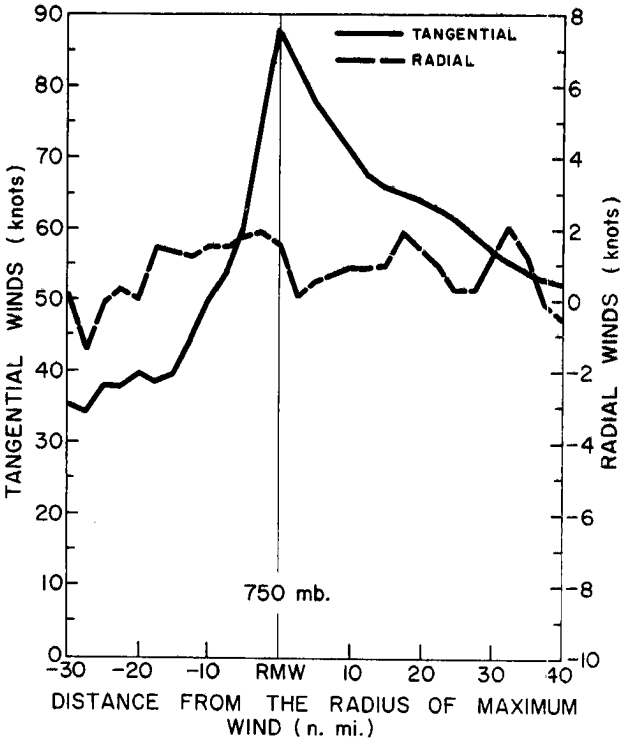

Fig. 10. The same as Fig. 9 except at 750 mb.

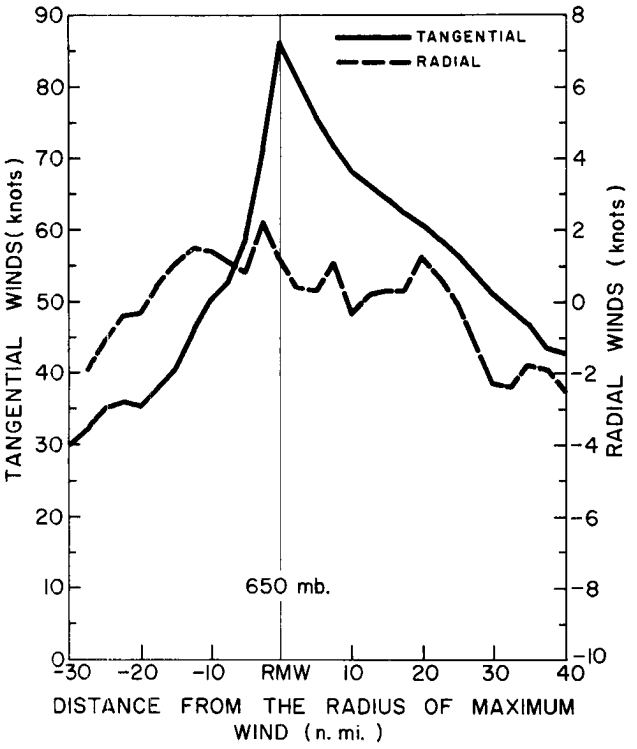

Fig. 11. The same as Fig. 9 except at 650 mb.

Fig. 12. The same as Fig. 9 except at 525 mb.

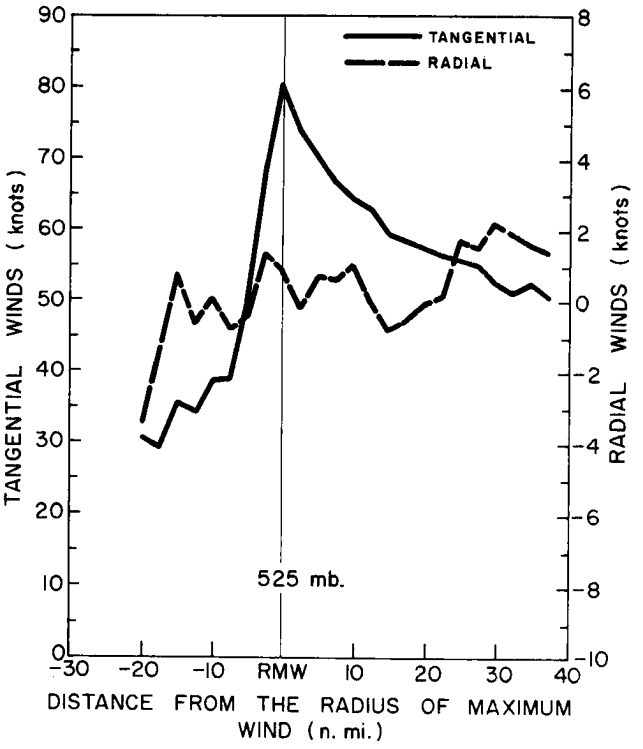

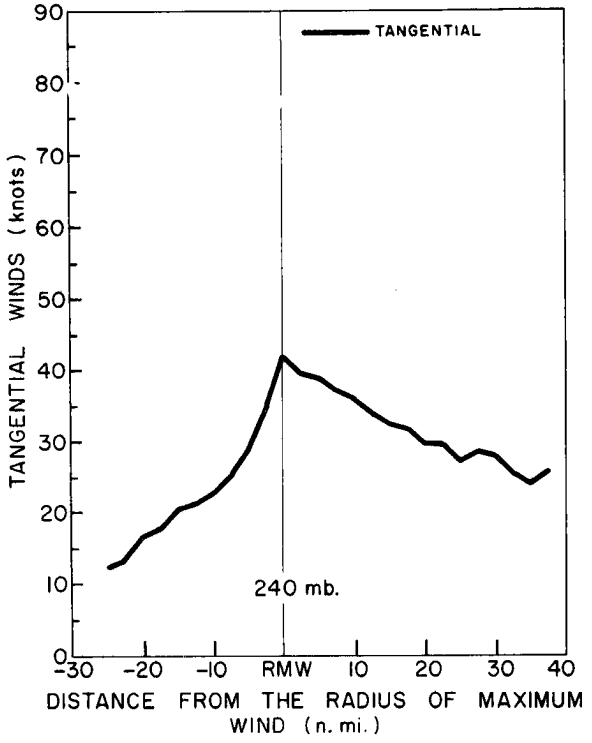

Fig. 13. The same as Fig. 9 except at 240 mb.

Fig. 14. Tangential wind profiles for the mean symmetric storm averaged with respect to the radius of maximum wind (method I).

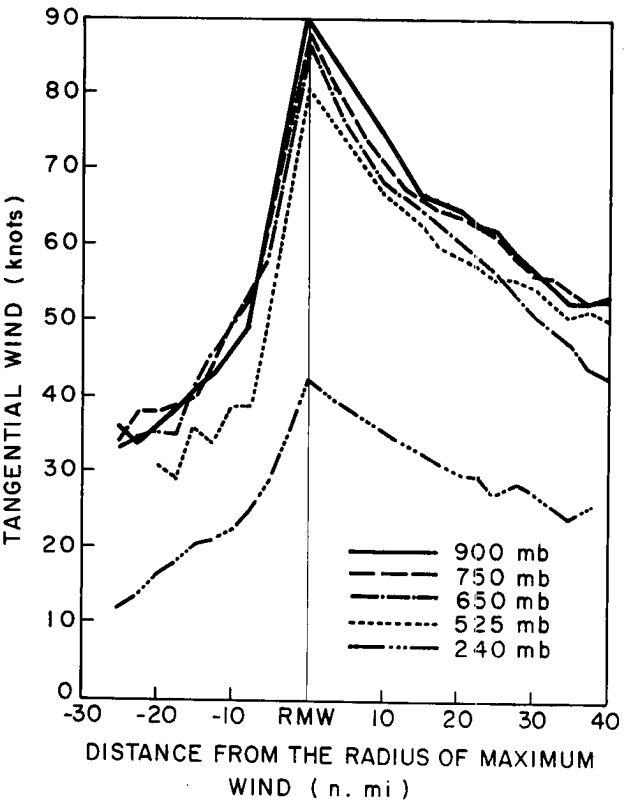

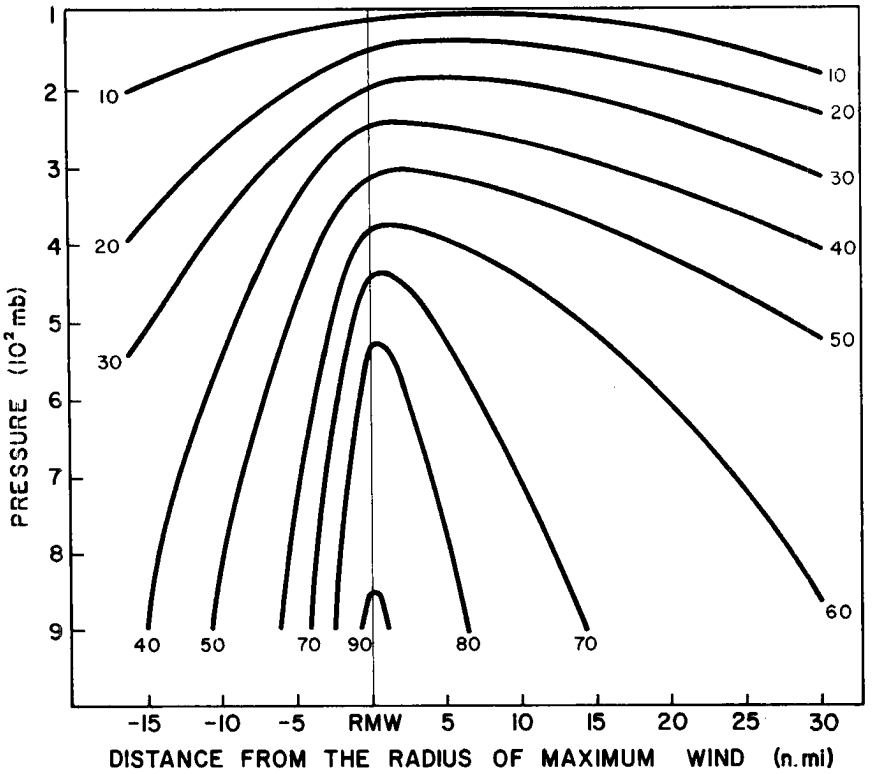

Fig. 15. Vertical cross section of tangential wind for the mean symmetric storm (method I).

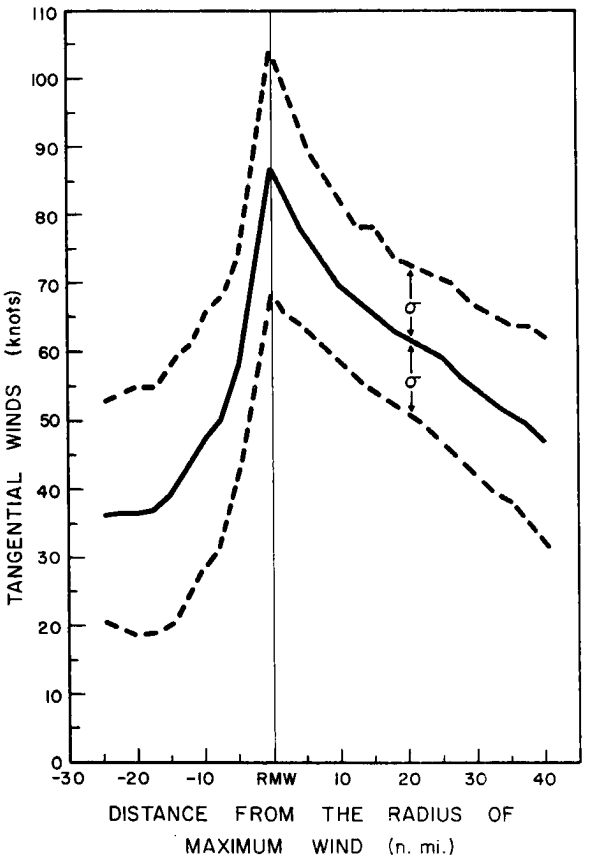

Fig. 16. Mean tangential wind profile and standard deviation (σ) for the 900-500 mb layer in the mean symmetric storm (method I).

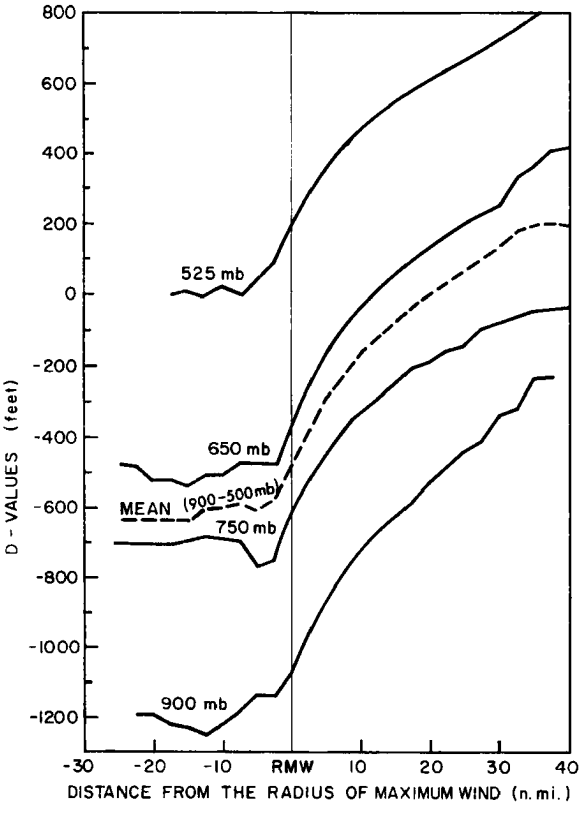

Fig. 17. D-values for lower four levels of the mean symmetric storm. The mean D-value profile for the 900-500 mb layer is shown by the dashed line (method I).

outside the radius of maximum winds we have the strong convergence one might expect in a layer near the top (~ 900 mb) but apparently just within the surface frictional boundary layer. The three middle levels (750, 650 and 525 mb) show very little overall inflow or outflow but convergence is present at and just outside the RMW. No radial winds are presented for the 240 mb level due to small amount of radial wind data available at this level.

D-Values. D-values for the four lowest layers of the mean symmetric storm are presented in Fig. 17. D-value data was not available in sufficient quantity at the upper tropospheric level to give a reliable profile. The largest D-value gradients are found at and just

outside the radius of maximum wind. At radii inside the RMW the gradients are much less.

Adjusted Temperature. Fig. 18 shows the profiles of the adjusted temperatures for all five levels. Note that the warmest temperatures occur well inside the RMW, whereas, the largest temperature gradients occur at the radius of maximum wind. For the three middle layers these temperature gradients around the RMW average approximately one and a half to two degrees per 5 n. mi.

The departure of individual mean temperatures from the mean temperature at the RMW for each of the four lower levels is shown in Fig. 19. The largest temperature deviations inside the RMW occur at 525 mb. The deviations become smaller with decreasing elevation.

Fig. 20 shows a cross section of the temperature anomalies for the lower half of the troposphere. These increase rather markedly with elevation being between 7 and 8°C at 525 mb. This graph shows, quite well, the warm core nature of the hurricane and the concentration of the warming in the inner core area.

Frequency plots portraying temperature differences between temperatures five n. mi. on either side of the RMW (i.e., $T_{\text{RMW-5 n. mi.}} - T_{\text{RMW+5 n. mi.}}$) for the 950-700 mb and 700-500 mb layers are presented in Figs. 21 and 22[9]. The mean maximum wind for each

[9]When the RMW was less than ten n. mi., the gradients could not be measured. Section V of this report will show that the highest winds occur at these radii. Thus, Figs. 19 and 20 are somewhat biased toward weaker storms.

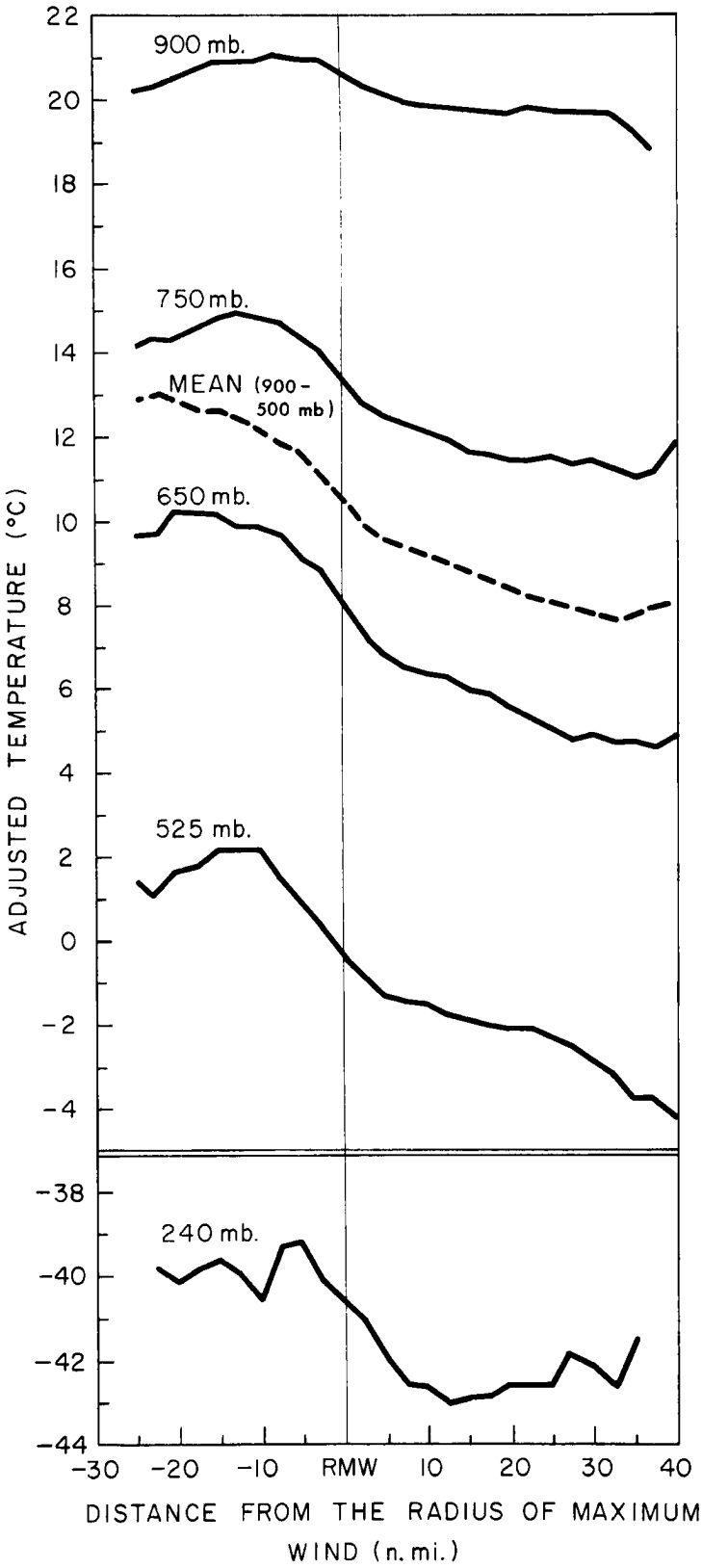

Fig. 18. Adjusted temperature profiles for the five levels of the mean symmetric storm. The mean adjusted temperature profile for the 900-500 mb layer is shown by the dashed line (method I).

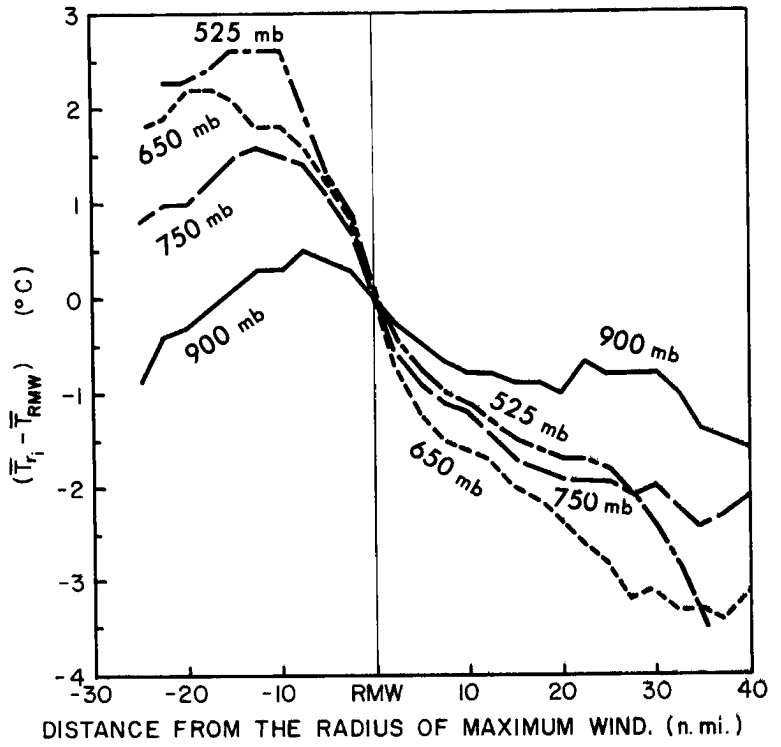

Fig. 19. Deviations of the individual mean adjusted temperatures (T_{ri}) from the mean adjusted temperature at the RMW ($\overline{T}_{RMW}$) for each of the four lower levels.

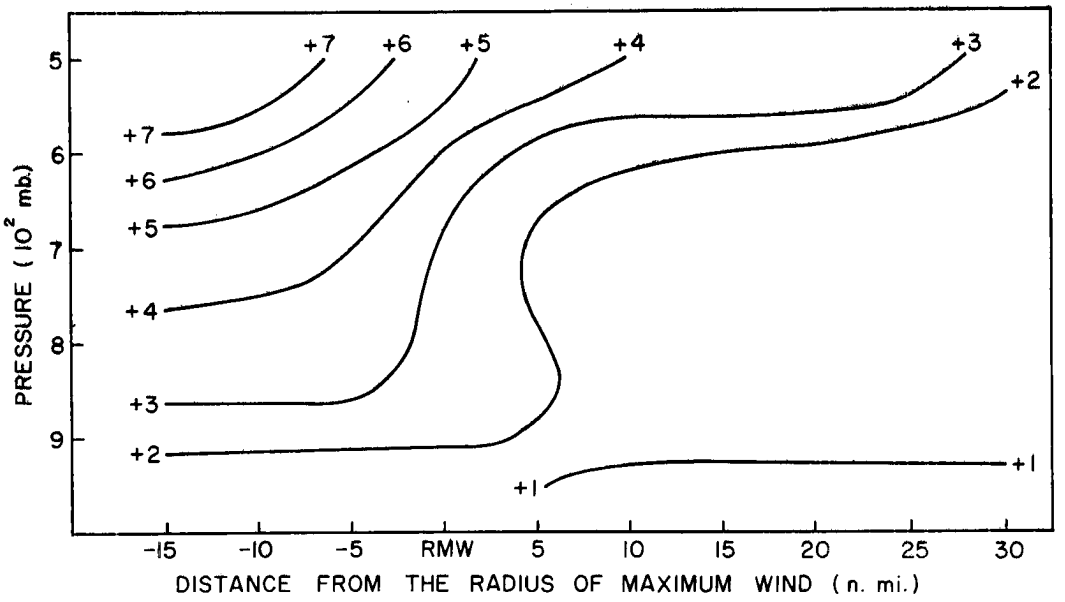

Fig. 20. Adjusted temperature anomaly pattern for the mean symmetric storm.

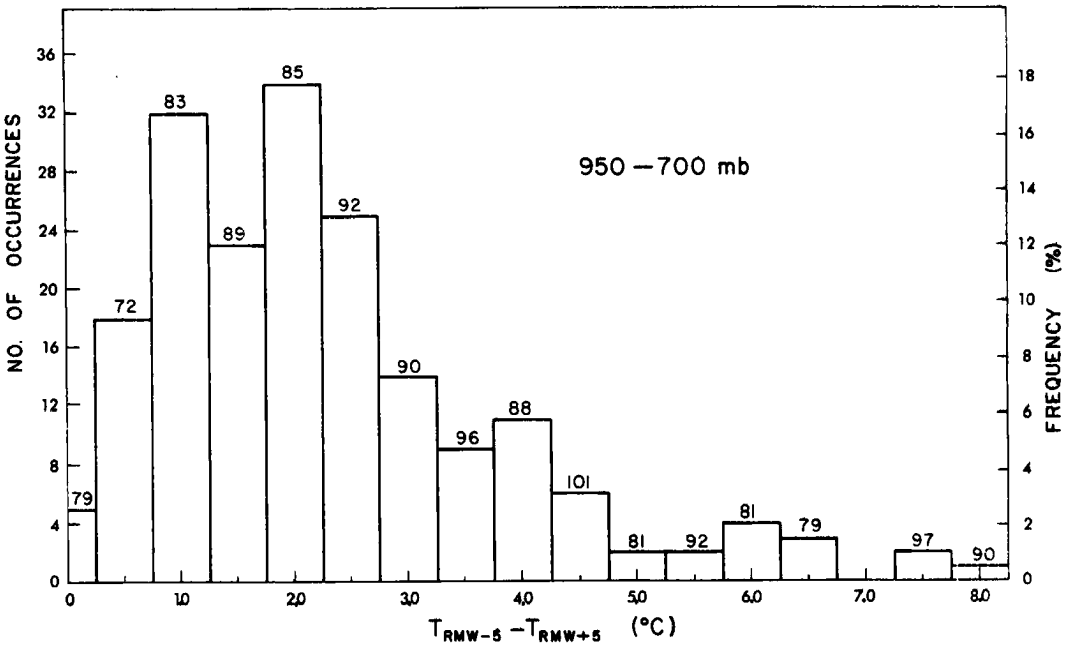

Fig. 21. Frequency diagram portraying individual ten nautical mile radial leg temperature differences which straddle the RMW for the 950-700 mb layer. The mean maximum wind (in knots) is indicated at the top of each block.

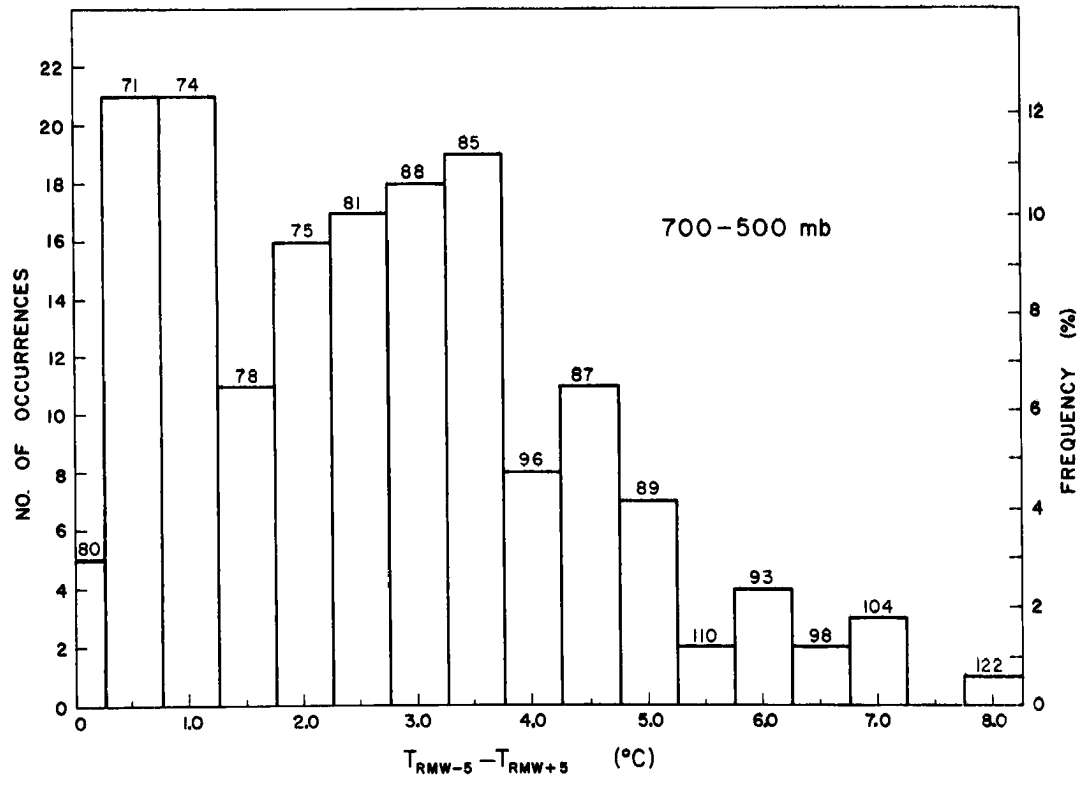

Fig. 22. Frequency diagram portraying individual ten nautical mile radial leg temperature differences which straddle the RMW for the 700-500 mb layer. The mean maximum wind (in knots) is indicated at the top of each block.

temperature difference is also shown. The large variability in wind speed and temperature difference values shows that only in the statistical average are these parameters correlated.

Virtual Temperature Correction. Because of some uncertainties in the humidity measurements this parameter was not treated. No virtual temperature corrections have been made to the raw temperature data used in this study. All temperature measurements were assumed to have been taken in an atmosphere with a constant relative humidity. At radii well inside and outside the RMW this is probably not valid because relative humidities are less than at the RMW. Estimates of the effect of a virtual temperature correction on the measured temperatures have been made. Table 3 lists the virtual temperature corrections for relative humidities of 25 and 50 percent less than at the RMW. Fig. 23 visually portrays the effect a virtual temperature correction would have in the lower half of the troposphere. It is greatest at the lower levels.

The effect that the virtual temperature correction would have on the observed temperature gradients (i.e., baroclinicity) is shown in Table 4. This table presents observed radial temperature gradients and the changes in the radial temperature gradients due to various assumed relative humidity reductions. The ± 5 n. mi and ± 10 n. mi. radial gradients are centered about the RMW.

Several case studies [e.g., Colon and Staff (1961) and La Seur and Hawkins (1963)] indicate that relative humidities in the inner fifty

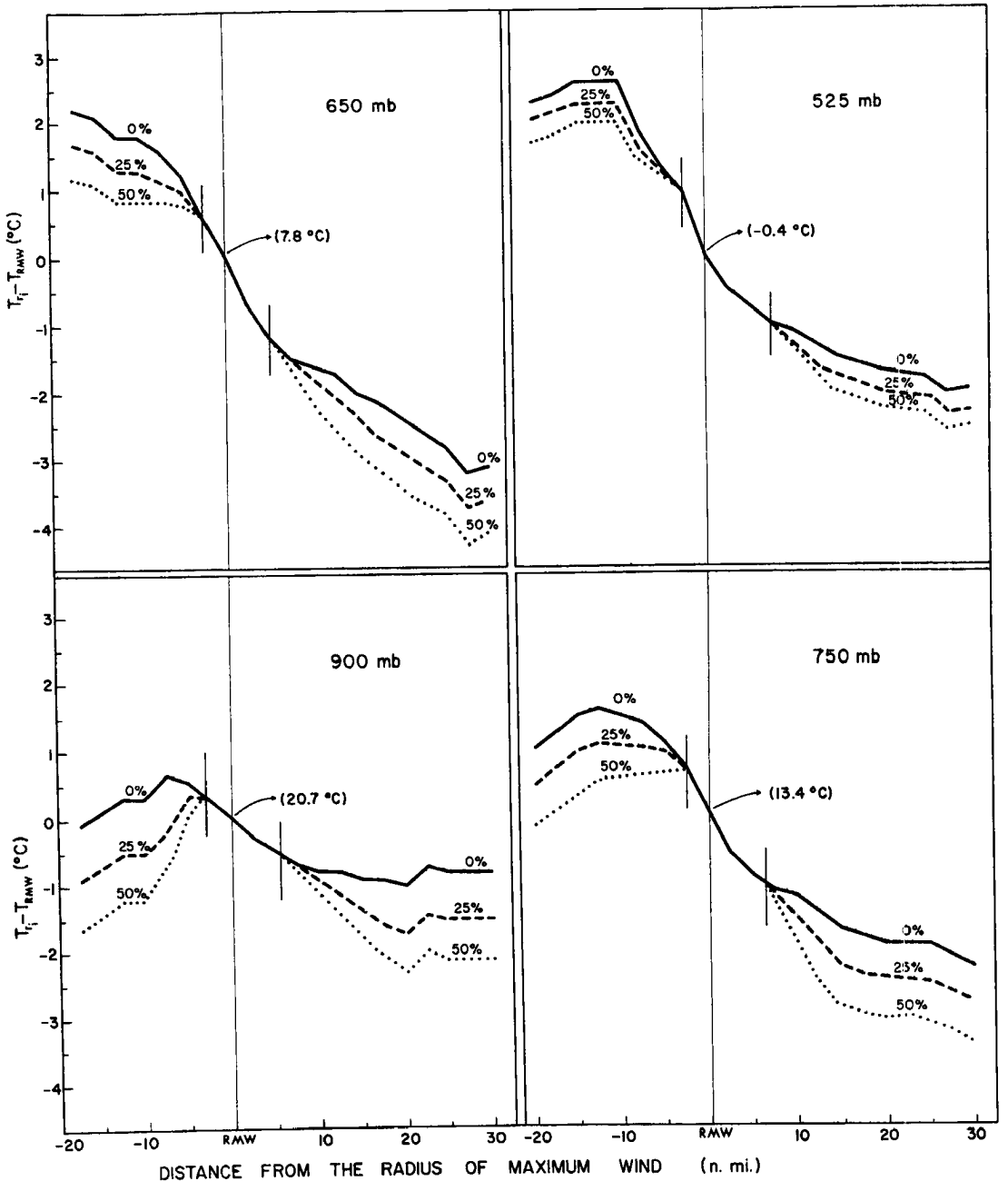

Fig. 23. Virtual temperature reduction due to various lower relative humidities inside and outside the eye wall cloud region. The vertical lines define the cloud eye wall region. The temperatures in parenthesis are the observed temperatures at the RMW.

TABLE 3

Virtual Temperature Reduction in ^{o}C for Relative Humidity Reduction of 25 and 50 Percent

Pressure (mb)	T(^{o}C)	25%	50%
900	21	0.8	1.5
	20	0.7	1.4
	19	0.7	1.3
750	15	0.6	1.2
	14	0.6	1.2
	13	0.5	1.1
	12	0.5	1.0
	11	0.5	1.0
650	10	0.5	1.0
	9	0.5	0.9
	8	0.4	0.9
	7	0.4	0.8
	6	0.4	0.8
	5	0.4	0.7
525	2	0.3	0.6
	1	0.3	0.6
	0	0.3	0.5
	-1	0.3	0.5
	-2	0.2	0.4
	-3	0.2	0.4
240	(-37) - (-43)	0.0	0.0

TABLE 4

Changes in Observed 10 and 20 n. mi. Radial Temperature Gradients (Centered at the RMW) Due to Virtual Temperature Corrections for Various Relative Humidity Reductions

Pressure (mb)	Observed Adjusted Temp. Gradient straddling RMW by ± 5 and ± 10 n. mi. (±5/±10)	Change in observed temp. gradients due to including virtual temp. correction for various relative humidity reductions from the RMW values		
		25% less inside eye 0% outside eye	50% less inside eye 0% outside eye	50% less inside eye 25% less outside eye
900	1.0/1.2°C	0.2/1.0	0.7/1.5	0.7/1.2
750	1.9/2.8°C	0.1/0.6	0.4/1.2	0.4/0.7
650	2.4/3.4°C	0.2/0.5	0.5/1.0	0.5/0.5
525	2.2/3.6°C	0.0/0.2	0.1/0.6	0.1/0.4

nautical miles outside the RMW are between 85 and 100 percent. Inside the eye the relative humidities at low levels are quite high (80 to 95%) but decrease with elevation. Relative humidity may be as low as 40 to 60% in the subsidence part of the eye at middle levels (Jordan, 1957). Simpson (1952) and Jordan (1961) have shown that in typhoons these may even be lower.

In summary, Table 4 shows that the virtual temperature correction would have only a small effect on the temperature gradients for realistic humidity variations. In Fig. 23 note that in the region outside the RMW a humidity decrease would act to increase the radial temperature gradient.

Slope of the Radius of Maximum Wind with Elevation. The left portion of Fig. 24 shows the slope of the RMW with elevation for storms with simultaneous lower and upper tropospheric data. The right side of this figure shows the slope of the RMW with elevation for those storms which have two or more lower tropospheric levels. Only the weaker storms exhibit a tendency for a slope of the RMW with height; more intense storms do not. The vertical slope of the RMW is probably related to the intensity of cumulus convection. The more active eye wall convection in intense storms is more effective in transporting horizontal momentum to upper levels. This causes the cumuli to stand straighter and the maximum winds at upper levels to occur more directly above those at lower levels.

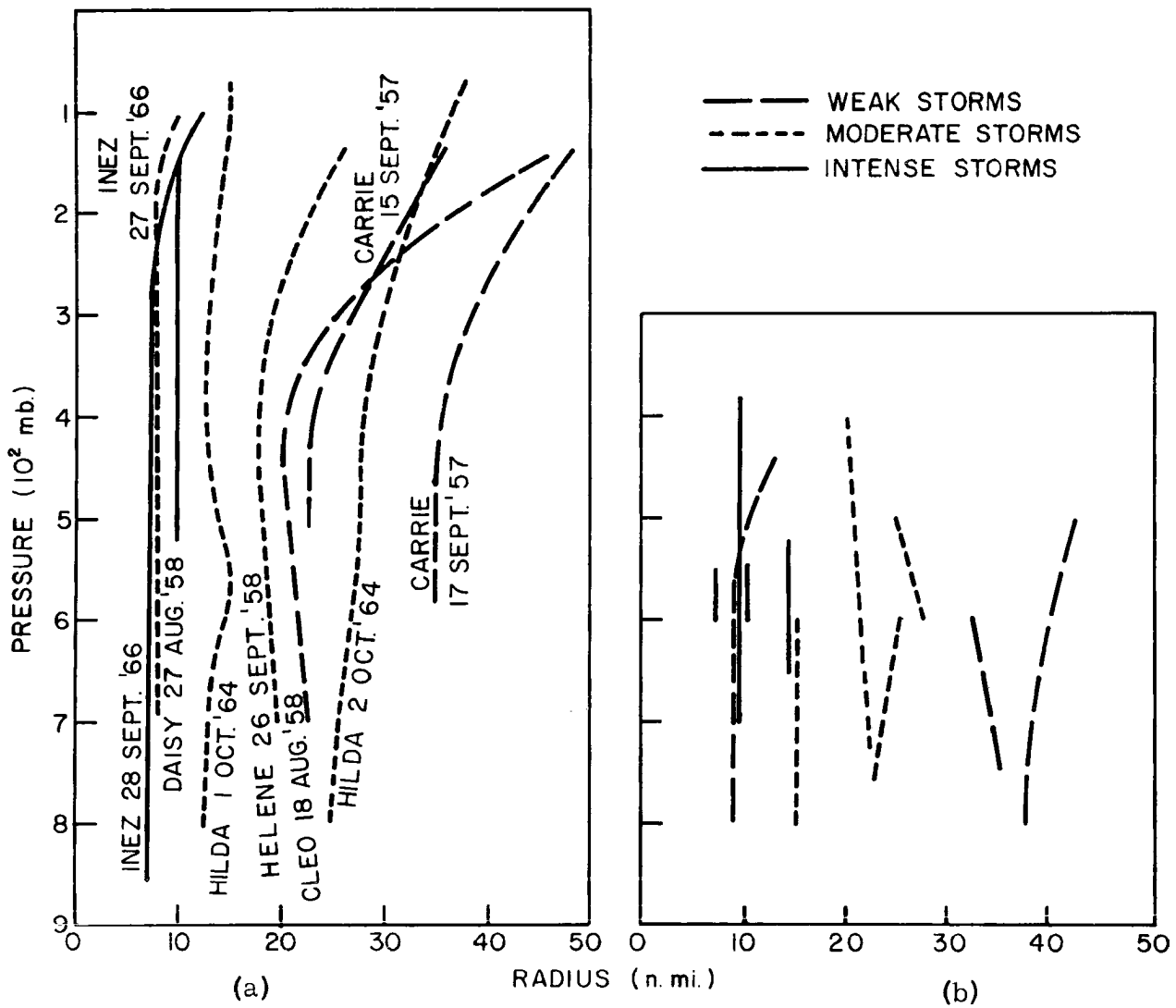

Fig. 24. Variation of the RMW with elevation for (a) storms with simultaneous lower and upper tropospheric data and (b) storms with two or more simultaneous flights in lower troposphere only.

The fact that the slope of the RMW with height is small and apparently a function of intensity does not support the hypothesis by Palmén (1956). He felt that if a cylindrical thermal wind balance exists, then the eye should slope outward with height. Except in very weak storms (where cumulus convection is less intense) the RMW slope is rather small.

Position of the Inner Radar Eye Radius (IRR) Relative to the Radius of Maximum Wind. Fig. 25 shows the position of the RMW relative to the inner radar eye radius (assumed synonomous with the inner cloud wall). Obviously, in the overwhelming majority of cases, the RMW occurs within the cloud area. In the mean the RMW occurs at radii five to six n. mi. outside the IRR.

Positioning errors could account for some of the difference but it seems likely that these errors would be random in such a large data sample. The larger discrepancies seen in Fig. 25 occurred in storms where the maximum wind was up to 35 n. mi. away from the region of largest horizontal wind shear.

Fig. 26 shows the difference between the RMW and the IRR versus the maximum velocity for individual radial legs. Positive values along the ordinate indicate that the maximum wind is within the cloud wall. Note that the more intense the wind the better is the agreement between the RMW and the IRR. Presumably, this is a result of the stronger subsidence in the more intense storms. This strong subsidence would tend to evaporate the inner portion of the eye wall cloud.

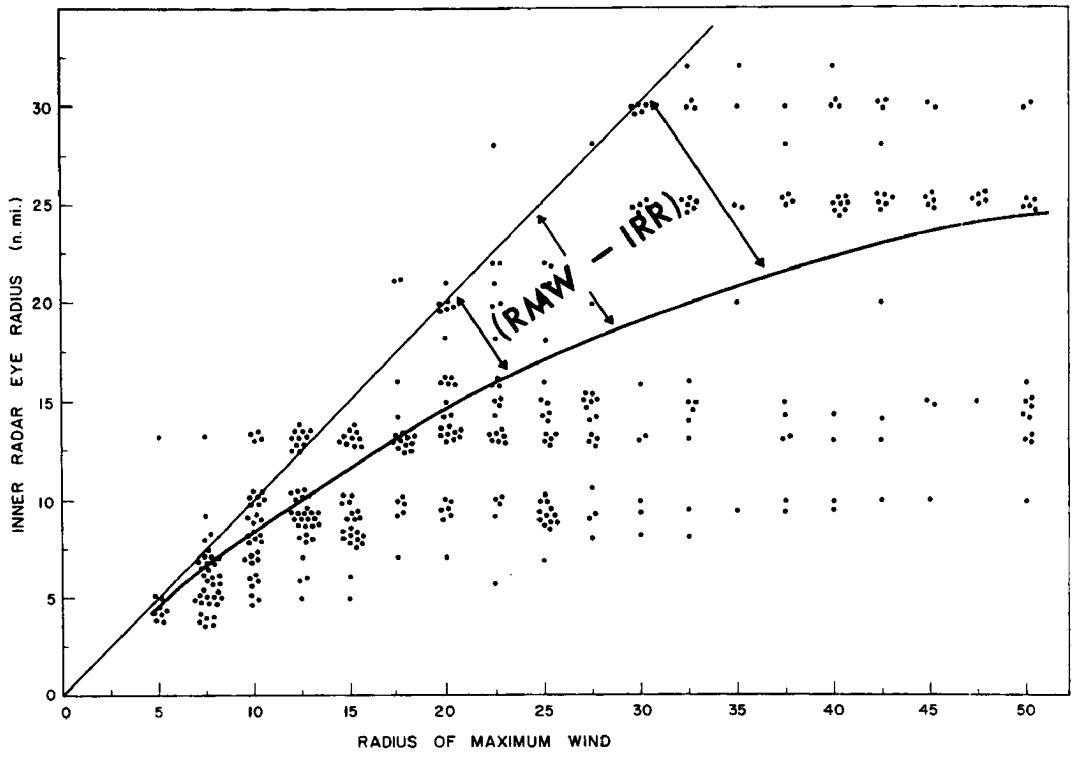

Fig. 25. Radius of maximum wind (RMW) versus inner radar eye radius (IRR). Points falling on the forty-five degree line are those where the RMW and IRR coincide. The heavy line indicates the best fit curve.

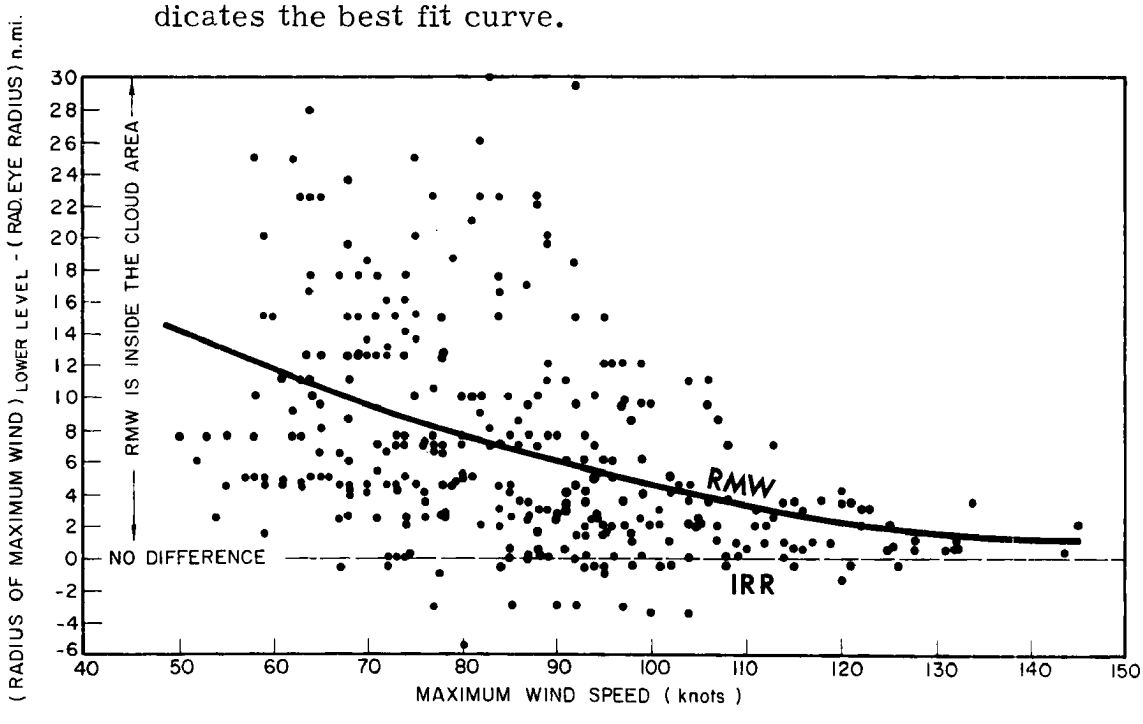

Fig. 26. Difference between the RMW and the inner radar eye radius versus maximum wind speed. The best fit curve is indicated by the heavy line.

Structure With Respect to the Absolute Radius

The structure of the mean storm when the data was composited w.r.t. absolute radius (method II) will now be briefly discussed.

Tangential Winds. Radial profiles of the tangential wind are shown in Figs. 27-31. At no radius does the wind exceed 70 knots. In general the profiles at all levels are quite flat except at the innermost radii (5-10 n. mi.). In this region the winds increase with increasing radii. Fig. 32 shows the tangential wind profiles for all the levels. As was the case in Fig. 14, the wind profiles are very similar in the lower half of the troposphere.

Radial Winds. Radial wind profiles are also shown in Figs. 27-30. The 900 mb layer shows inflow at all radii greater than ten nautical miles. The magnitude of the inflow is largest at the outermost radii and decreases as the center is approached. Inside ten n. mi. outflow is present. The middle levels (750, 650 and 525 mb) display a varying pattern.

D-Values. D-values for the four lowest layers are shown in Fig. 33. A systematic decrease in the D-values is evident when approaching the center. The D-gradients are quite uniform from fifteen to fifty n. mi. This is consistent with the tangential wind profiles which show rather uniform wind speeds at radii greater than fifteen nautical miles. The D-gradient is largest at ten to fifteen nautical miles. Inside this the D-gradient decreases only slightly.

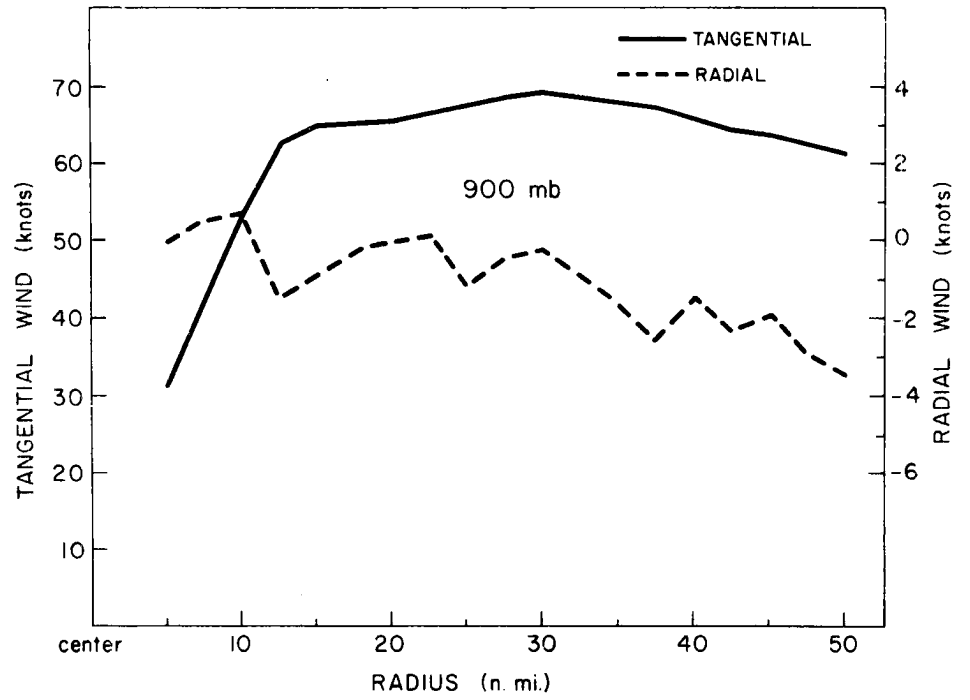

Fig. 27. Tangential and radial wind profiles for the 900 mb level where all the data has been averaged with respect to absolute radius (method II). Positive radial winds indicate outflow.

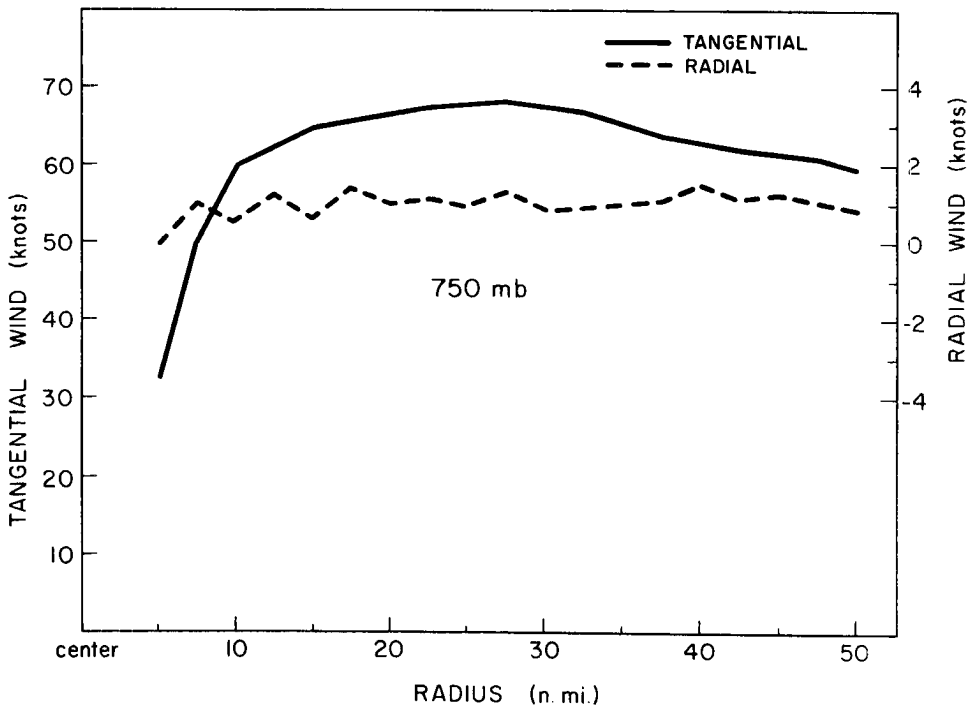

Fig. 28. Same as Fig. 27 except at 750 mb.

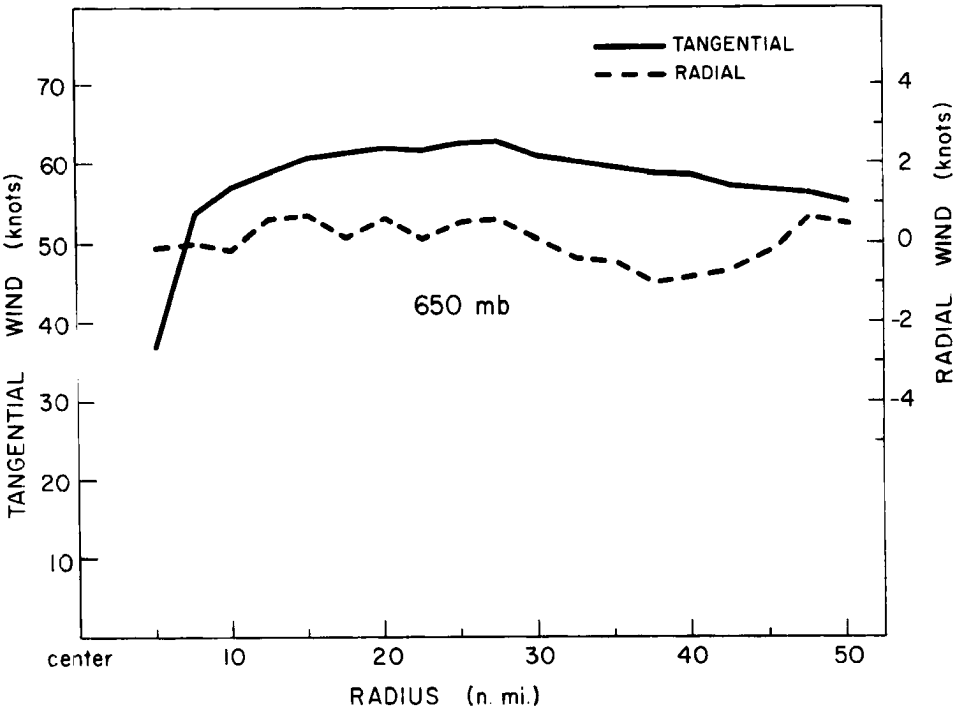

Fig. 29. Same as Fig. 27 except at 650 mb.

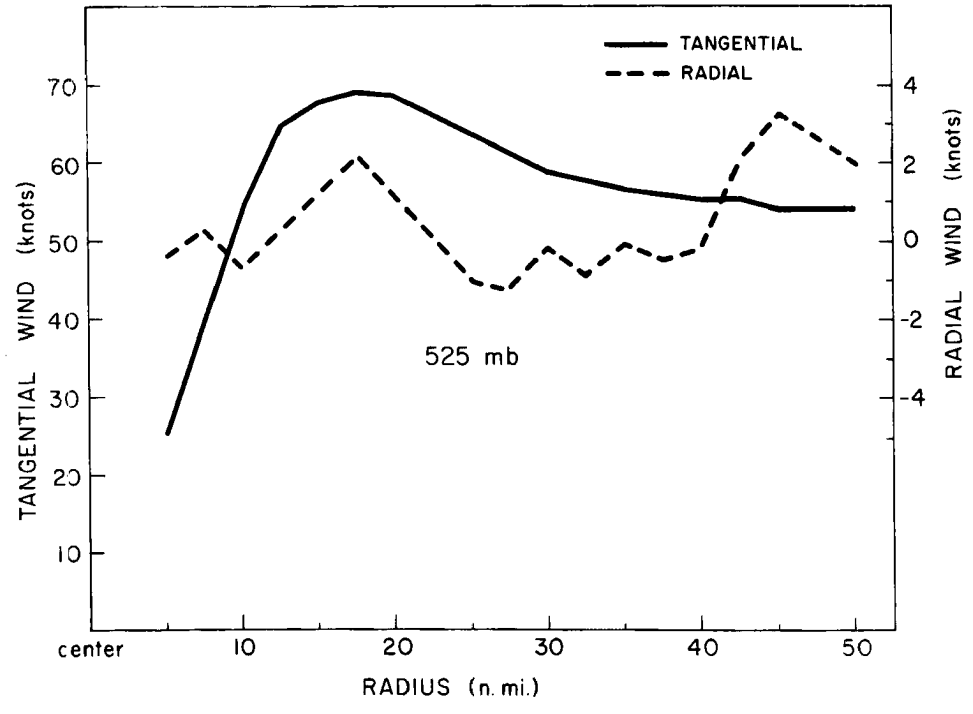

Fig. 30. Same as Fig. 27 except at 525 mb.

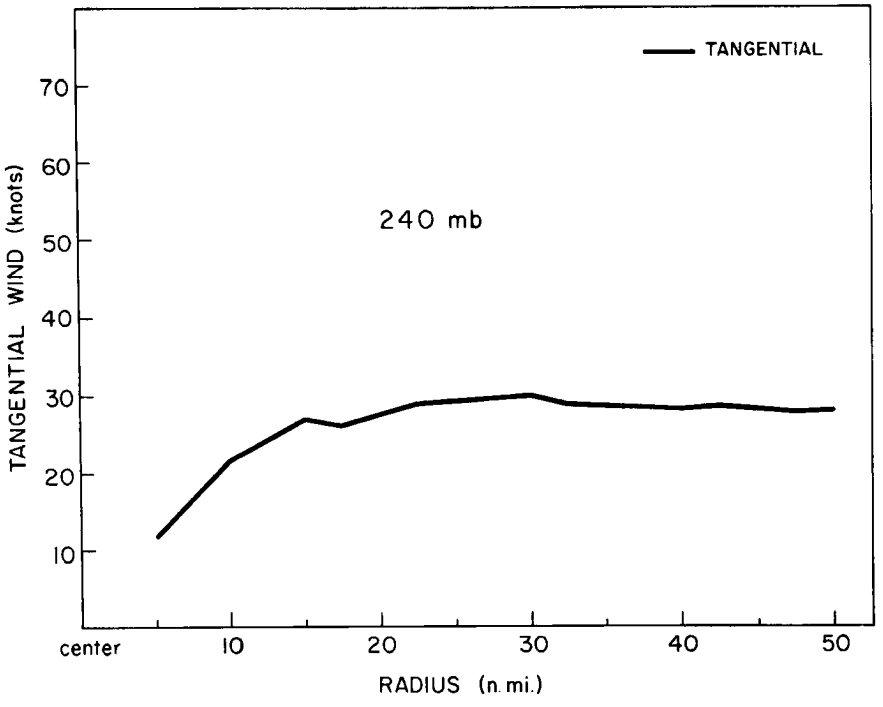

Fig. 31. Same as Fig. 27 except at 240 mb.

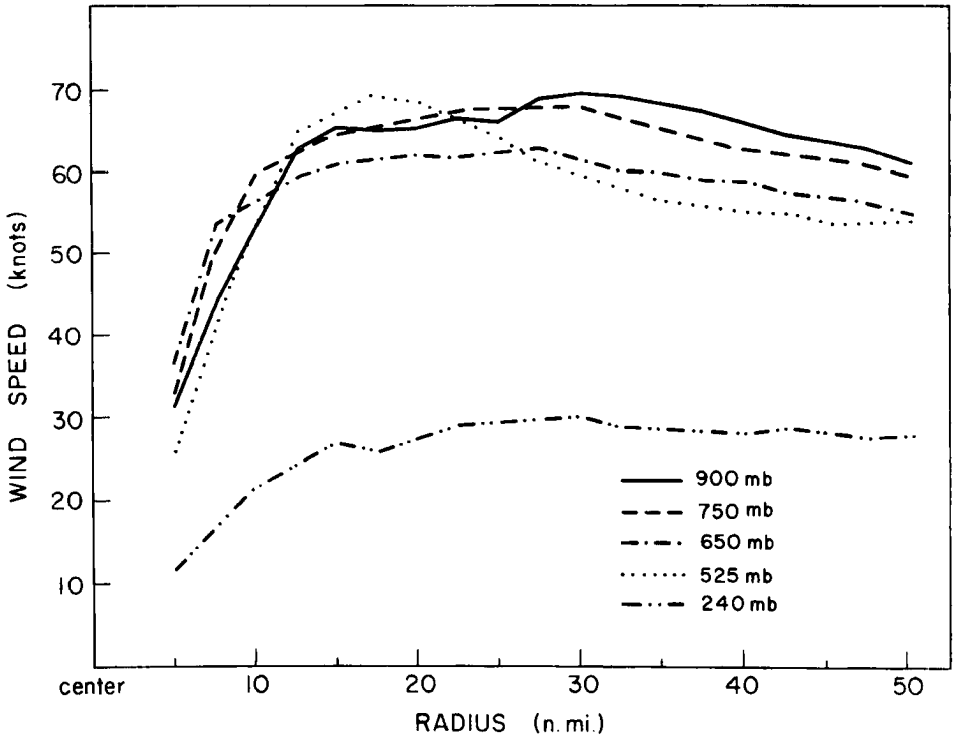

Fig. 32. Tangential wind profiles where data has been averaged with respect to absolute radius (method II).

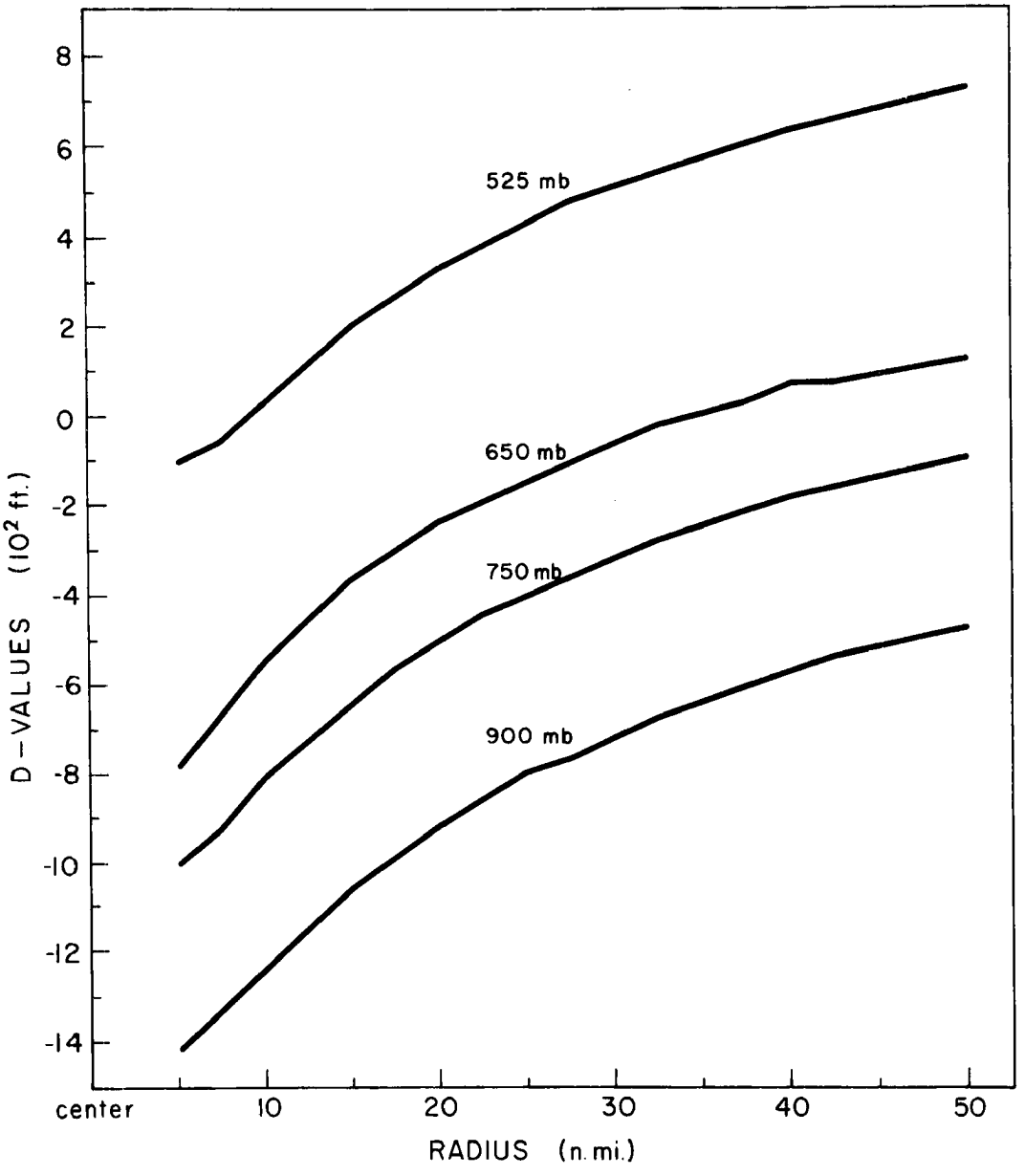

Fig. 33. D-value profiles where data has been averaged with respect to absolute radius (method II).

Adjusted Temperature. Fig. 34 presents temperature profiles for the five levels. The highest temperatures at each level are at the innermost radii. These decrease with increasing distance from the center. In general, the largest temperature gradients ($1^{o}C$ per 5 n. mi.) occur in the middle levels. The exception to this is the 240 mb level where inside ten n. mi. there is a large warming.

Comparing the mean storm structures determined by use of methods I and II, we can clearly see the superiority of method I. Use of method II results in the data being smoothed out - obscuring the essential features of the circulation in the inner core area. For this reason, no dynamic computations were performed using this method.

Dynamics

Dynamic computations were performed for each individual radial leg using absolute radius and then composited with respect to the radius of maximum wind (method I). The computations to be discussed include: (1) pressure gradient-wind balance; (2) cylindrical thermal wind balance; (3) absolute angular momentum; (4) relative vorticity; (5) kinetic energy; (6) divergence; (7) vertical motions; (8) mean vs. eddy transport; (9) slope of tangential wind profiles and (10) storm wind asymmetry. For computational simplicity a steady state, symmetric storm will be assumed.

Pressure Gradient-Wind Balance. The vortex averaged frictionless, cylindrical gradient wind equation is

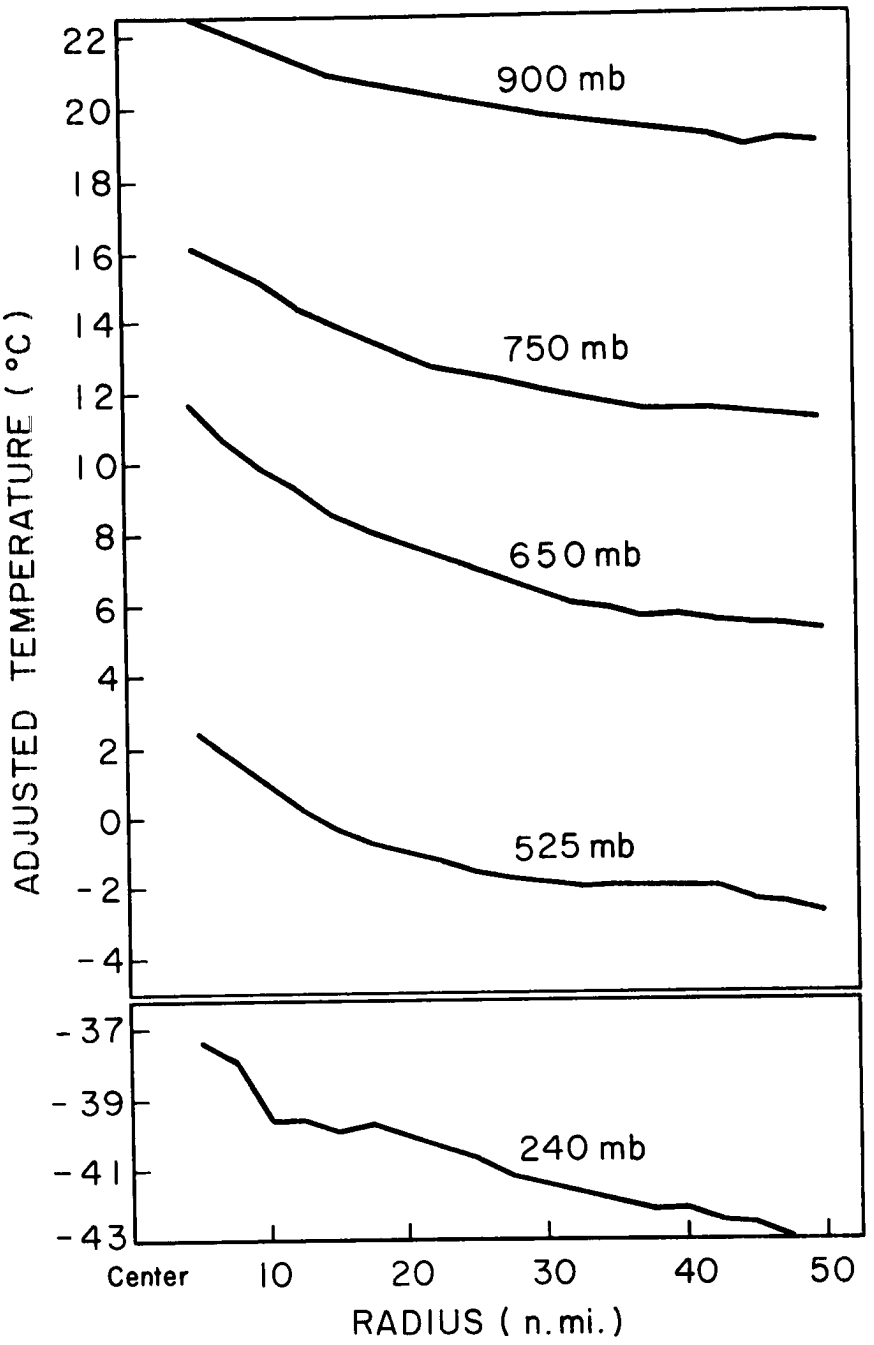

Fig. 34. Adjusted temperature profiles averaged with respect to absolute radius (method II).

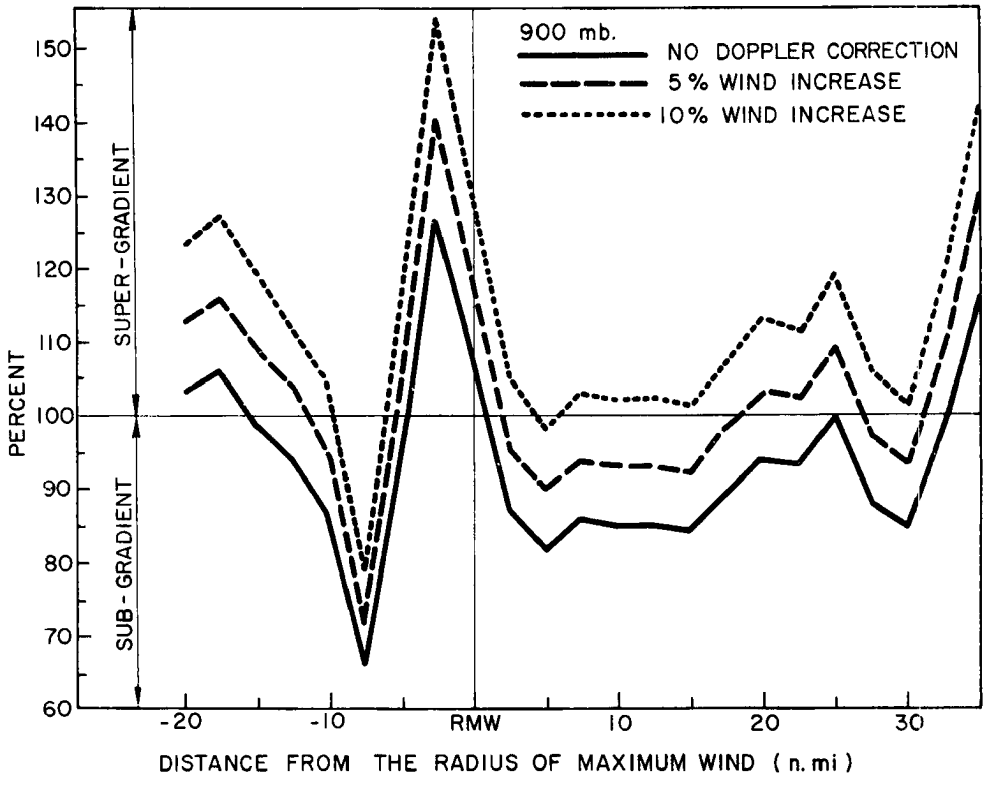

Fig. 35. Ratio (in percent) of the wind acceleration to the pressure acceleration at 900 mb (method I).

$$\frac{1}{2\pi r}\int_0^{2\pi}\left(fV_\theta + \frac{V_\theta^2}{r}\right) r\,\delta\theta = \frac{1}{2\pi r}\int_0^{2\pi} g\,\frac{\partial D}{\partial r}\, r\,\delta\theta \qquad (1)$$

where V_θ is the tangential wind

f is the coriolis parameter

g is the acceleration of gravity

D is the D-value

r is the radius

Using equation (1) balance computations were performed along each radial leg. The radial legs were then azimuthly averaged using the procedure outlined by Riehl (1963) in order to ascertain the degree of

gradient wind balance[10]. Figs. 35-39 show the ratio of the left hand side of equation (1) to the right hand side in percent for the four lower levels and for the lower half of the troposphere. Note that almost everywhere outside the RMW the wind accelerations are less than the pressure accelerations. At the radius of maximum winds distinct super-gradient winds are observed. Inside the RMW the wind-pressure ratio is, in general, less than 100%. It will be shown, however, that when the Doppler wind correction is added slightly super-gradient winds are present in this area. Malkus (1958) has hypothesized that these super-gradient winds in the eye are the result of an inward turbulent transfer of angular momentum from the higher wind region outside the eye. This is consistent with the observed divergent area just inside the eye wall which results from the required outward acceleration of the super-gradient winds.

Wind Correction Due to Water Motion. Attempts have been made to determine the effect that water motion has on the Doppler measured winds. It was felt that a Doppler wind correction might best be obtained from the imbalance in equation (1). To accomplish this, the winds along each individual radial leg were arbitrarily increased five and ten percent. The computations were again performed and composited. Figs. 35-39 show that wind increases of but five and ten percent will allow for gradient wind balance at radii outside the RMW.

---

[10]The V_θ^2/r term is felt to be only slightly underestimated using this procedure.

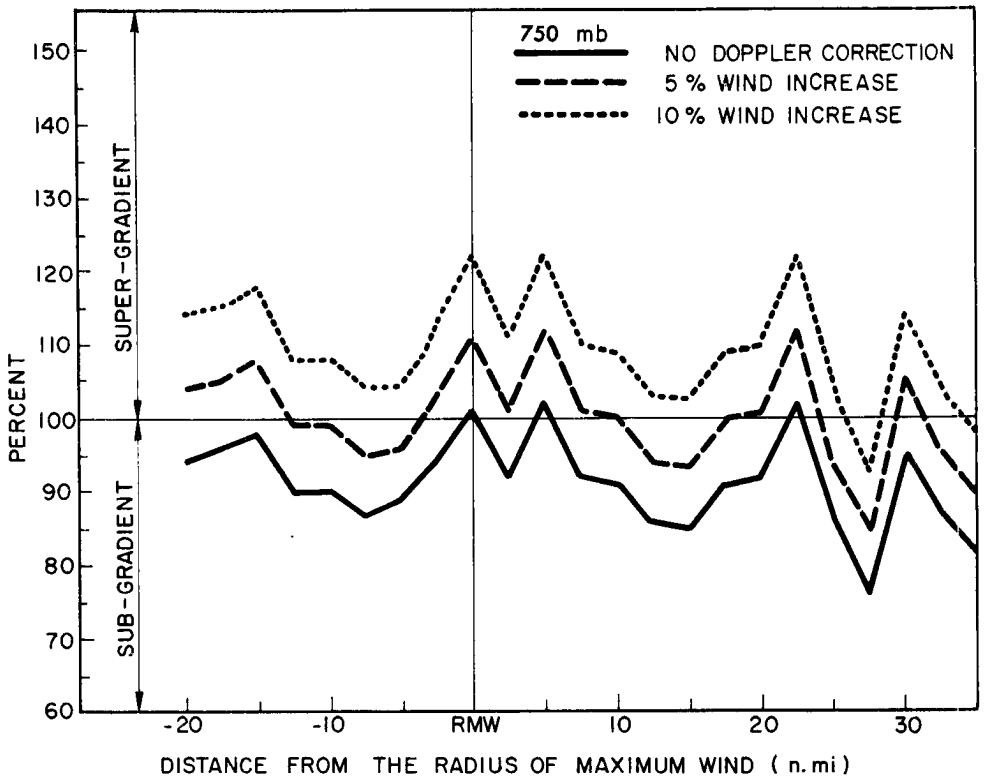

Fig. 36. Same as Fig. 35 except at 750 mb.

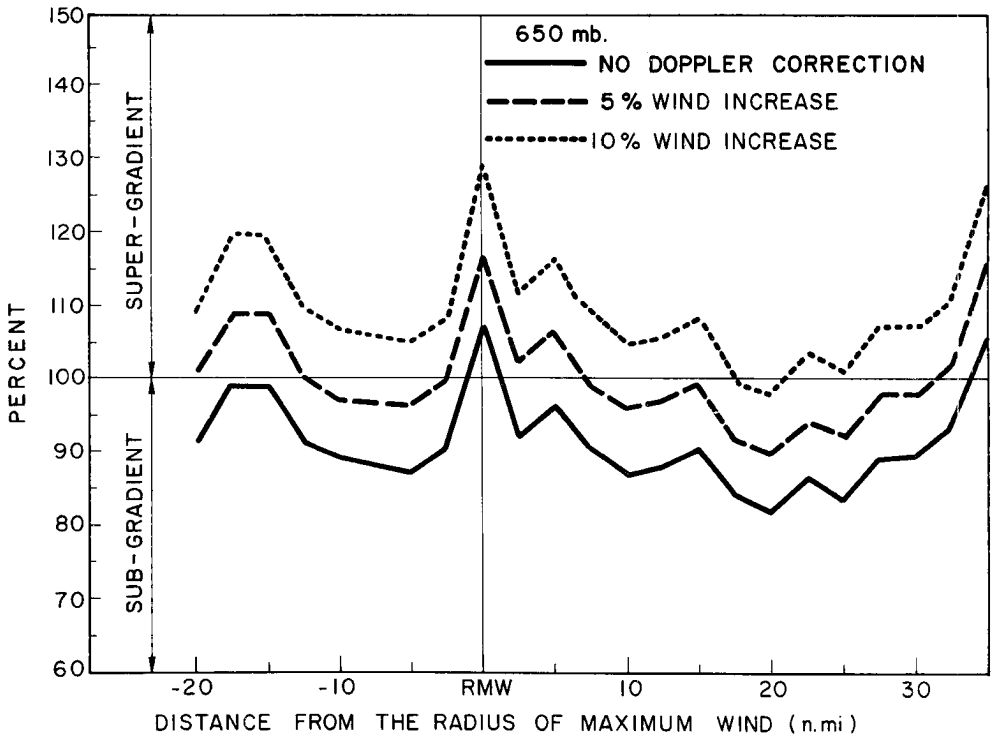

Fig. 37. Same as Fig. 35 except at 650 mb.

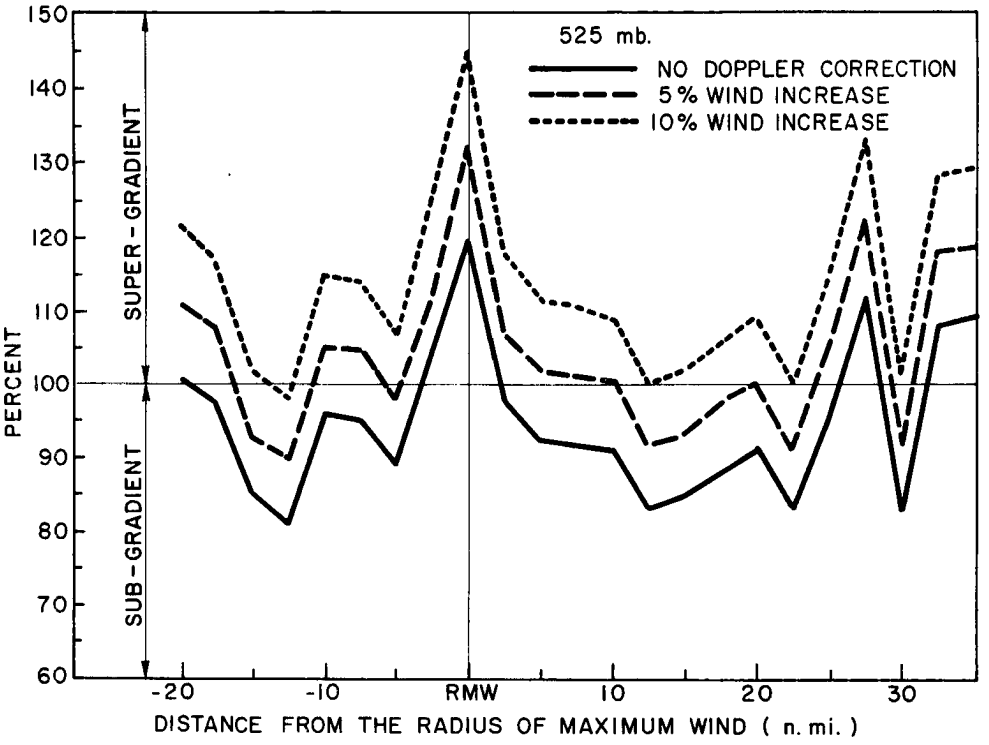

Fig. 38. Same as Fig. 35 except at 525 mb.

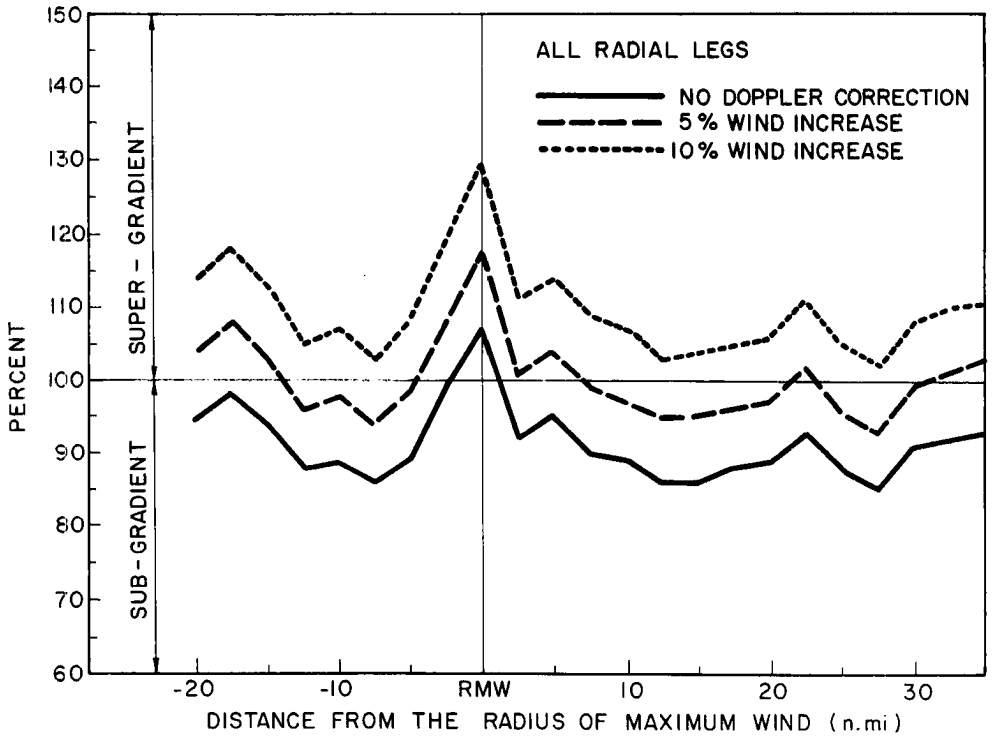

Fig. 39. Same as Fig. 35 except for all radial legs in the lower half of the troposphere.

Inside the RMW, especially in the lowest layer, the winds are super-gradient, supporting Malkus' (1958) hypothesis. At the radius of maximum wind significant super-gradient flow is observed with or without any correction. At 900 mb it is necessary to interpret these super-gradient winds as being 'overshot' (i.e., accelerated by the pressure gradient beyond the point of pressure gradient-wind equilibrium). The super-gradient winds at middle levels may be attributed to the vertical transport by the cumuli of higher momentum from lower levels.

Thermal Wind. The steady, symmetric, frictionless, cylindrical thermal wind equation with the origin at the center of a vortex may be written as

$$\left(f + \frac{2V_\theta}{r} \right) \frac{\partial V_\theta}{\partial p} = - \frac{R}{p} \left(\frac{\partial T}{\partial r} \right)_p \qquad (2)$$

where R is the gas constant

$)_p$ denotes differentiation along a constant pressure surface and the other symbols as previously defined

Using the notation of Gray (1967), equation (2) can be abbreviated as

$$W_r S = B \qquad (3)$$

where $W_r = \left(f + \frac{2V_\theta}{r}\right)$ = inertial parameter

$S = \partial V_\theta / \partial p$ = vertical wind shear parameter

$B = - \frac{R}{p} \left(\partial T / \partial r \right)_p$ = baroclinicity

A complete evaluation of equation (3) could be accomplished for the double level flights listed in Table 2. To be considered the flights at each level were required to have at least four approximately equally spaced radial legs and the flights must have occurred within a reasonable time interval of each other (5-6 hours). These requirements greatly reduced the number of eligible flights. Eligible double level flights were weighted by pressure intervals -- those over larger pressure intervals counted more.

Fig. 40 portrays the weighted composited values of $W_r S$ and B for the double level flights which occurred exclusively in the lower half of the troposphere. Fig. 41 presents the same values for those double level flights in which one level was below 500 mb and other between 200-260 mb. Also shown in each figure is the baroclinicity excess (B_{ex}) defined as

$$B_{ex} = B - W_r S \tag{4}$$

In the lower half of the troposphere it is evident that from the RMW outward to the RMW + 15 n. mi. the baroclinicity is 40 to 60% larger than the inertial - vertical wind shear term. (With the virtual temperature correction this imbalance could even be larger at radii outside the RMW). This imbalance is believed to be due to the cumulus convection which acts to distribute the horizontal momentum more uniformly throughout the vertical with up and down motions as

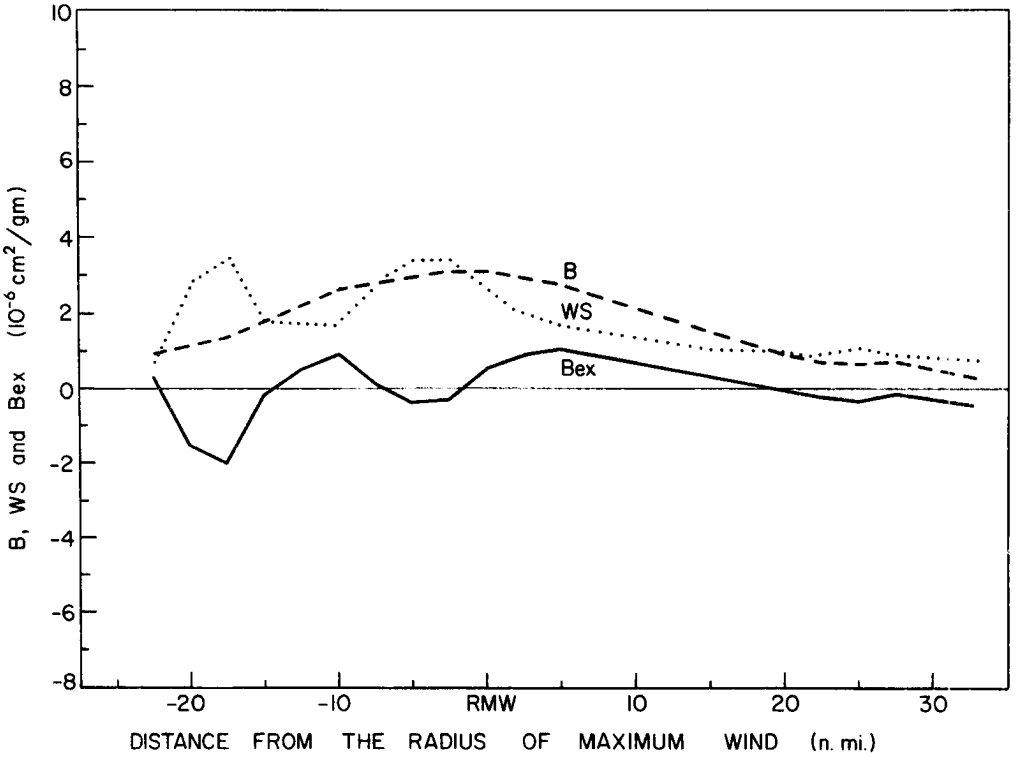

Fig. 40. Profiles of B, W_rS and B_{ex} for double level flights which were conducted exclusively in the lower troposphere (10^{-6} cm^2/gm; method I).

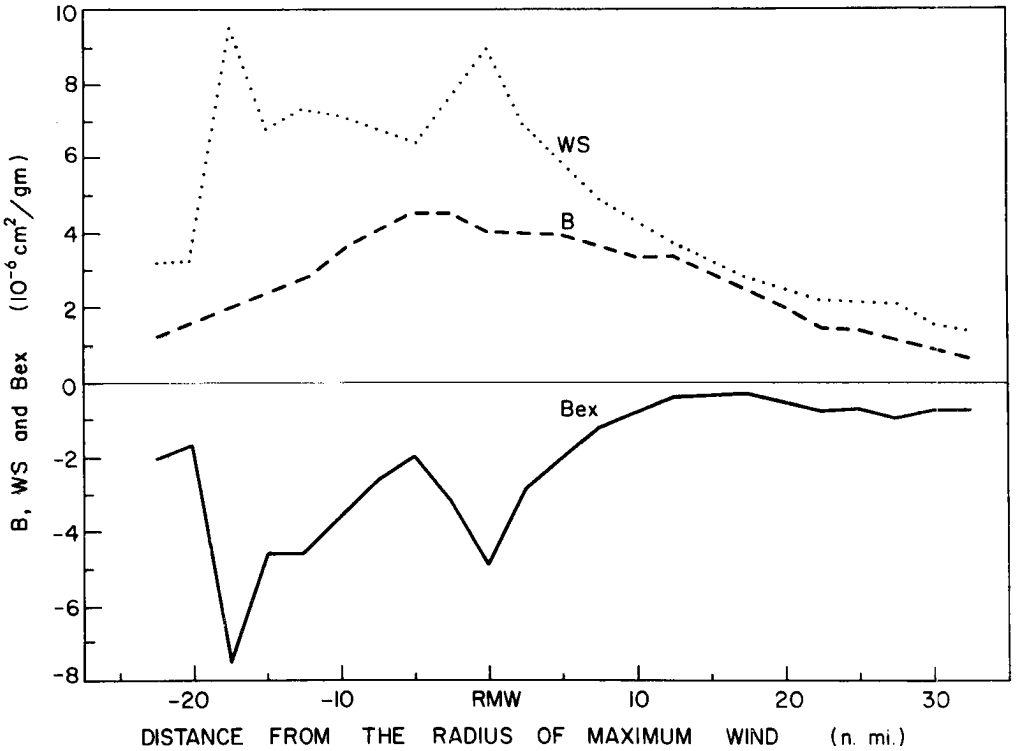

Fig. 41. Profiles of B, W_rS and B_{ex} for double level flights which have lower and upper tropospheric data (10^{-6} cm^2/gm; method I).

hypothesized by Gray (1967). Between the lower and the upper half of the troposphere the $W_r S$ term is 10 to 50% larger than the baroclinicity. The cumulus momentum transfer mechanism is less effective in the upper troposphere.

Individual storms showed wide fluctuations from this pattern. About half the storms show a very pronounced thermal wind imbalance with baroclinicity 2 to 5 times larger than vertical shears would prescribe at and just beyond the RMW. Other storms showed a deficit of baroclinicity.

The imbalance of the cylindrical thermal wind equation in the lower troposphere can also be investigated from a composite of all the flight data in vertical cross-section form as portrayed in Fig. 15. Table 5 shows the ratio of calculated vertical wind shear assuming cylindrical thermal wind balance to the vertical wind shear observed in the mean storm. It should be noted that the observed vertical wind shears at the RMW are only 60-70% of the values prescribed by cylindrical thermal wind balance. In other words calculated shears are larger than observed shears. This is believed to be due to the vertical transfer of momentum by the cumuli at the RMW.

TABLE 5

Ratio of Calculated to Observed Vertical Wind Shear
From Composite of All Flight Data

Pressure (mb)	n. mi. from RMW -10	-5	RMW	+5	+10	+15	+20
525	1.2	.9	1.5	.8	.7	.9	.6
650	1.5	1.9	1.5	.9	.9	1.0	1.3
750	1.3	1.8	1.3	1.0	1.0	1.1	1.2

Absolute Angular Momentum. The absolute angular momentum (M) of a parcel when expressed in a cylindrical coordinate system with the origin at the hurricane center is given by,

$$M = V_\theta r + \frac{fr^2}{2} \qquad (5)$$

with symbols as before.

Using equation (5) a mean cross section of absolute angular momentum was constructed (Fig. 42). Obviously, the absolute angular momentum of the air in the lower levels is decreasing as the center is approached. This decrease is due to the friction between the air and the sea surface. It shows that a hurricane represents a sink region of angular momentum. At the upper outflow levels the lines of constant angular momentum become more nearly horizontal. This is

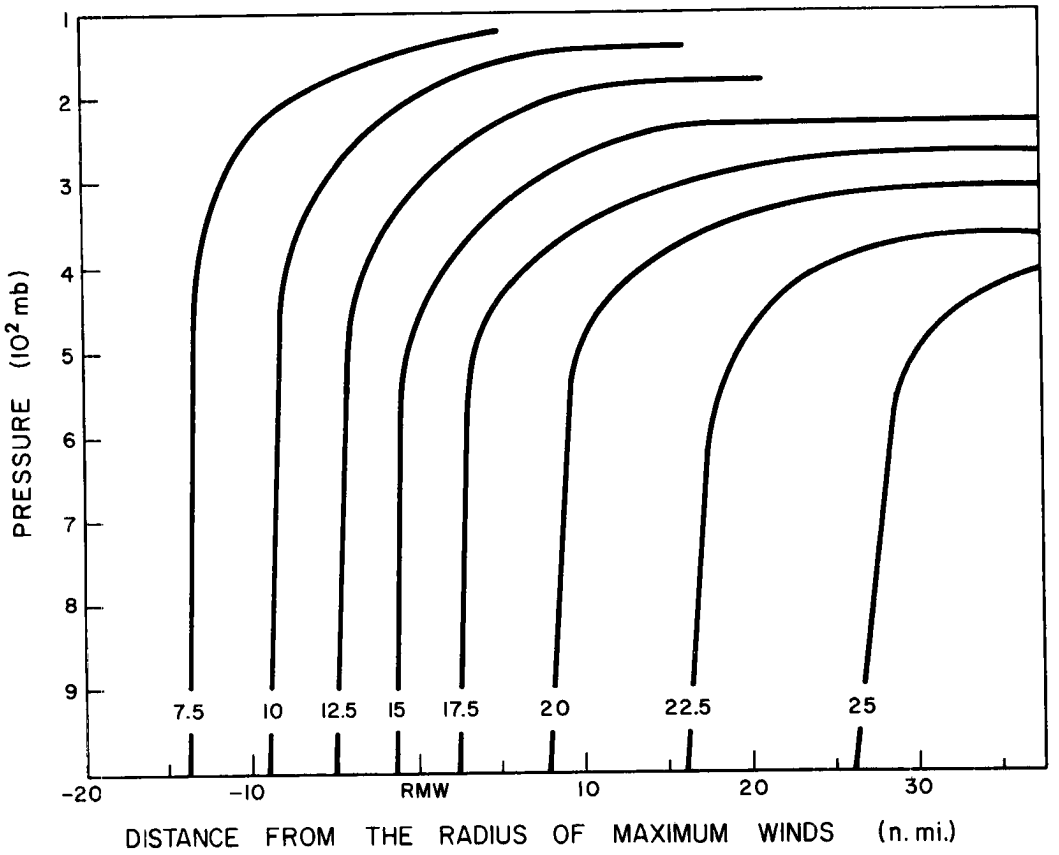

Fig. 42. Cross section of absolute angular momentum (10^9 cm^2/sec; method I).

required if the outflowing air between 175 and 250 mb is to conserve its momentum.

Relative Vorticity. The relative vorticity (ζ_r) of a parcel is given by,

$$\zeta_r = \frac{\partial V_\theta}{\partial r} + \frac{V_\theta}{r} \qquad (6)$$

The mean cross section of relative vorticity is shown in Fig. 43. The concentration of vorticity just inside of the RMW, due to the large horizontal shears, is readily seen.

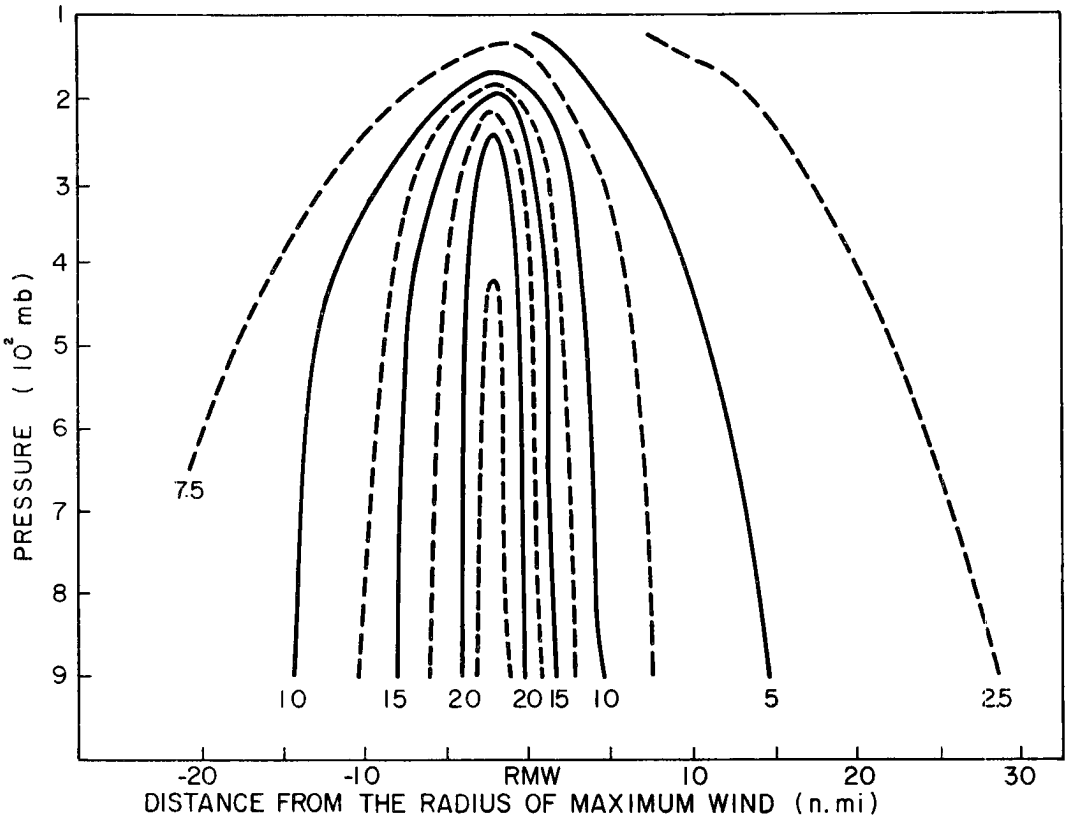

Fig. 43. Cross section of relative vorticity (10^{-5} sec^{-1}; method I).

Kinetic Energy. Fig. 44 presents a vertical cross section of kinetic energy [11] (KE) per unit mass,

$$KE = \frac{1}{2\pi r} \int_0^{2\pi} \frac{V_\theta^2}{2} r\delta\theta \qquad (7)$$

As expected the largest KE is at the RMW and there is only a small decrease of KE with height in the lower half of the troposphere. The KE drops off rapidly inside the RMW.

---

[11] The kinetic energy is felt to be only slightly underestimated by virtue of the impossibility of accounting for all storm asymmetry from only 4-6 radial leg measurements.

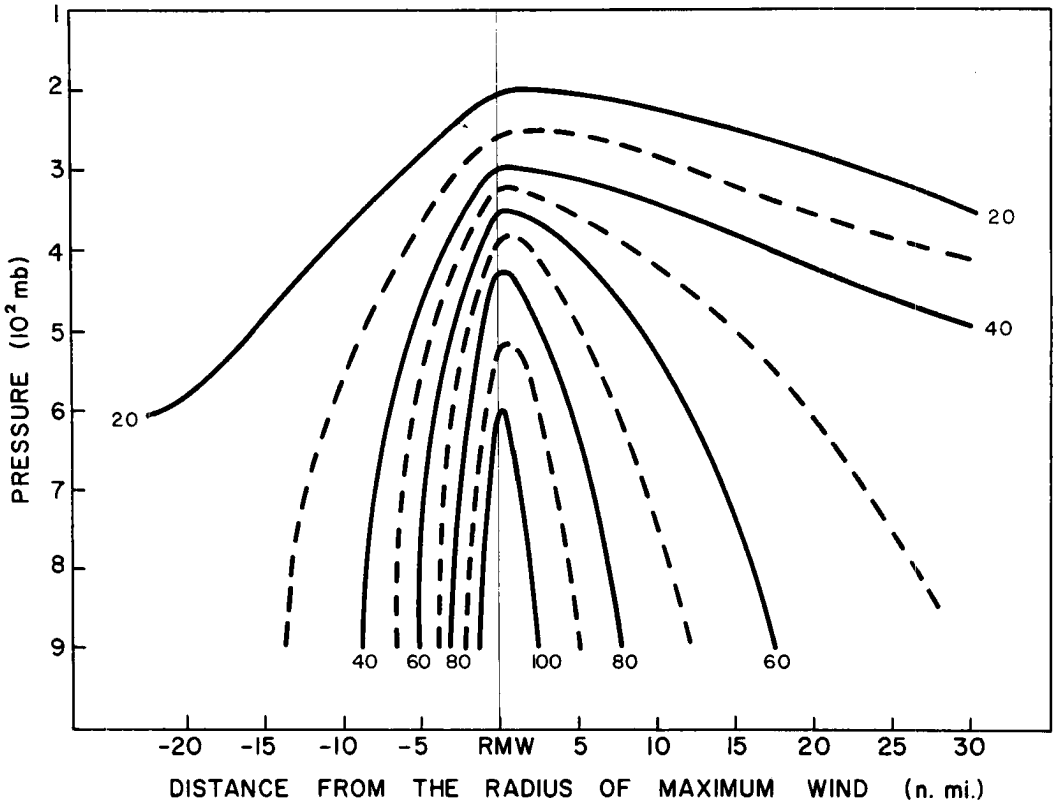

Fig. 44. Cross section of kinetic energy (10^5 cm^2/sec^2; method I).

Divergence. Fig. 45 presents a vertical cross section of divergence (DIV) in units of 10^{-5} sec^{-1} where,

$$DIV = \frac{\partial V_r}{\partial r} + \frac{V_r}{r} \tag{8}$$

Note the intense convergence (~23 x 10^{-5} sec^{-1}) at and just outside the RMW at 900 mb (approximately the top of the boundary layer). It is here that the eye wall air starts its ascent. Large convergence is also present just inside the RMW. This rapidly gives way at higher levels and small radii to large divergence. At 5-7 n. mi. inside the

RMW divergence of approximately 20 x 10^{-5} sec^{-1} is observed in the lowest layers.

Vertical Motions. The vertical motion pattern was kinematically determined utilizing the divergence values just described. The results are shown in Fig. 46 in units of 100 mb/day. The largest ascending vertical motions (~-50 x 10^2 mb/day) are concentrated in a narrow area at the RMW. At radii outside the RMW weak and variable vertical motions are noted. This pattern supports the often held viewpoint, first mentioned by Wexler (1945) and later emphasized by Robert and Joanne Simpson (at many AMS meetings), that most of the "ascending motion occurs through a relatively narrow ring near the storm's center". A narrow region of strong subsidence (~40-50 x 10^2 mb/day) is present approximately 5-7 n. mi. inside the RMW. It is interesting to note that this is approximately the mean position of the inner radar eye radius. Well inside the RMW weaker subsidence is present.

Although ascending vertical motions of approximately 50 x 10^2 mb/day (~0. 8 m/sec) appear to be low for a hurricane, case studies [e.g., Riehl and Malkus (1961)] indicate that the hurricane does not have a uniform vertical motion pattern. Rather only a small portion of the hurricane is covered by strong updrafts. Assuming that 10 percent of the eye wall region is covered by intense convection a mean ascending vertical motion of about 8 m/sec would be present in these

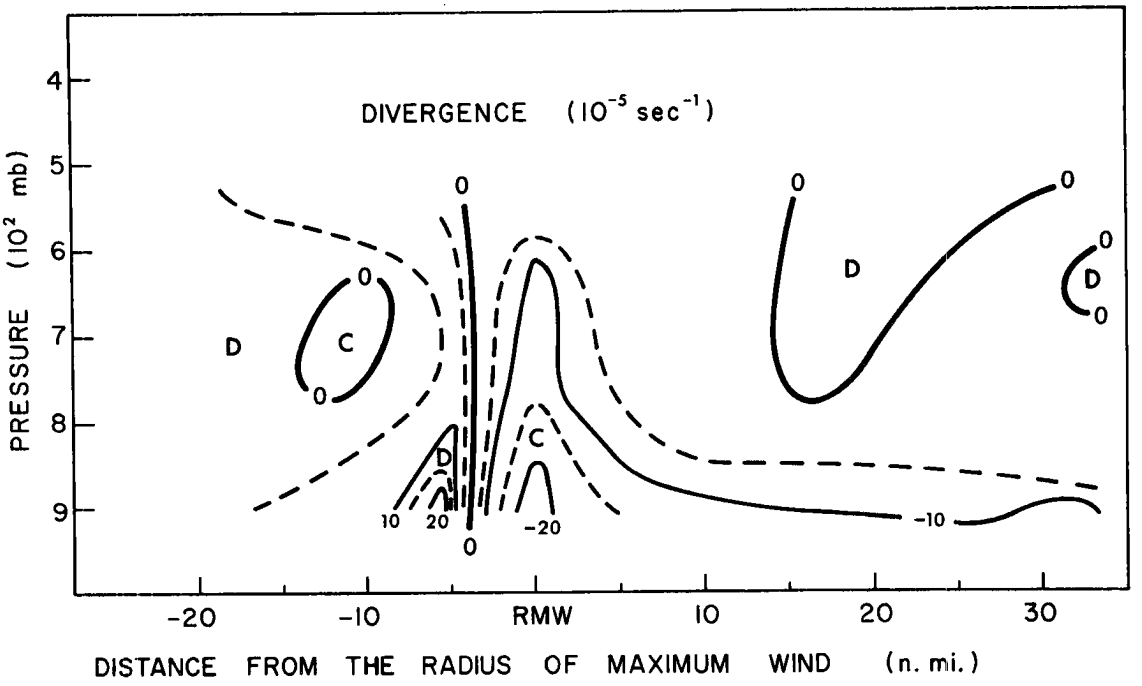

Fig. 45. Cross section of divergence (10^{-5} sec^{-1}; method I).

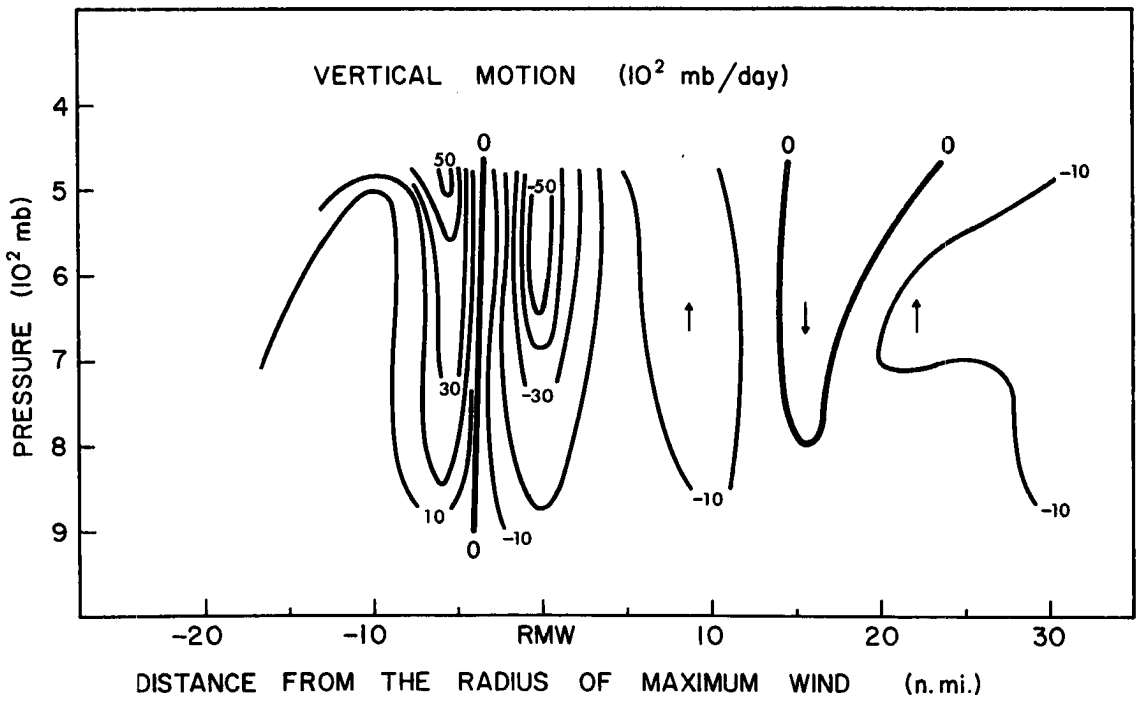

Fig. 46. Cross section of kinematically computed vertical motion (10^2 mb/day).

regions. This agrees with Gray's (1965) calculated vertical motions in cumulus at the RMW.

Mean vs. Eddy Transports. The importance of the eddy quantity $\overline{V'_{\theta r} V'_{rr}}$ which appears in the radial momentum equation compared to the mean flow $\overline{V_{\theta r}}\,\overline{V_{rr}}$ was determined. It was found that the mean flow term is much larger (often by one or two orders of magnitude) than the eddy term. Thus, in the inner core region of the hurricane the eddy or perturbation radial transports of momentum are much smaller than the mean transports. This is a further verification of the findings by Riehl (1961) who stated that inside 600 km the transport of momentum by eddies is quite small compared to the mean flow.

Slope of Tangential Wind Profiles. Riehl (1954, 1963) and Hughes (1952) have noted that hurricane winds can be approximated by an equation of the form,

$$V_\theta r^x = \text{constant} \tag{9}$$

where V_θ is the tangential wind
r is the absolute radius
x is the exponent

Inside the RMW, $x = -1$ (solid rotation) is often assumed and outside the RMW $x = 0.5$ is often considered to give a good fit. Obviously, glancing at Fig. 4 it can be seen that the above exponents can hardly be expected to describe all profiles. However, in order to assess

mean values of x for inside and outside of the RMW, best fit exponents were determined for all 533 radial legs. The resultant means and standard deviations for the lower (900-500 mb) and upper (~240 mb) level data are shown in Table 6.

TABLE 6

Level (mb)	Mean Exponent Inside RMW and Standard Deviation	Mean Exponent Outside RMW and Standard Deviation
240	-1.48 (±0.8)	0.73 (±0.6)
900-500	-1.05 (±0.6)	0.47 (±0.3)

In the lower levels x inside = -1 and x outside = 0.5 are indeed good approximations. Riehl (1963) assumed a constant surface drag coefficient and he determined a value of x outside the RMW of 0.5. At the upper level it is apparent that the lower 0.5 exponents are not valid. The magnitudes for the inside and outside exponents at this level are larger by approximately 50 percent. Again, it should be remembered that we are discussing mean exponents. Along an individual radial leg these exponents can be quite different.

Storm Wind Asymmetry. In Section IV it will be shown that there is a large degree of asymmetry in both the actual tangential and relative tangential winds. Quantitative estimates of the asymmetries in these winds were determined for selected flight missions that had at

least four approximately equally spaced radial legs. The equation used was,

$$\text{asymmetry} = \frac{(V_{max})_r - (V_{min})_r}{(\overline{V})_r} \tag{10}$$

where $(V_{max})_r$ is the maximum wind at any radius r

$(V_{min})_r$ is the minimum wind at any radius r

$(\overline{V})_r$ is the mean wind at the radius

Equation (10) will yield asymmetries which are somewhat smaller than actually occurring because it is unlikely that the aircraft will measure the absolute maximum and absolute minimum winds at a particular radius. The resulting composited asymmetries are shown in Fig. 47. The largest asymmetries for both wind types are inside the RMW. This is probably due to the higher degree of wind variability inside the RMW and to center positioning errors. Outside the RMW the asymmetries are less. The asymmetry exhibited by the relative winds verifies that there is a natural asymmetry in hurricanes beyond that induced by storm motion as discussed by Sherman (1956).

Thermodynamics

Stability. Profiles of equivalent potential temperature (θ_e) at several radii for the mean symmetric storm are presented in Fig. 48. The assumptions made in drawing this figure are: (a) in cloudy areas (i.e., at the RMW and at the RMW + 20 n. mi.) there is a linear de-

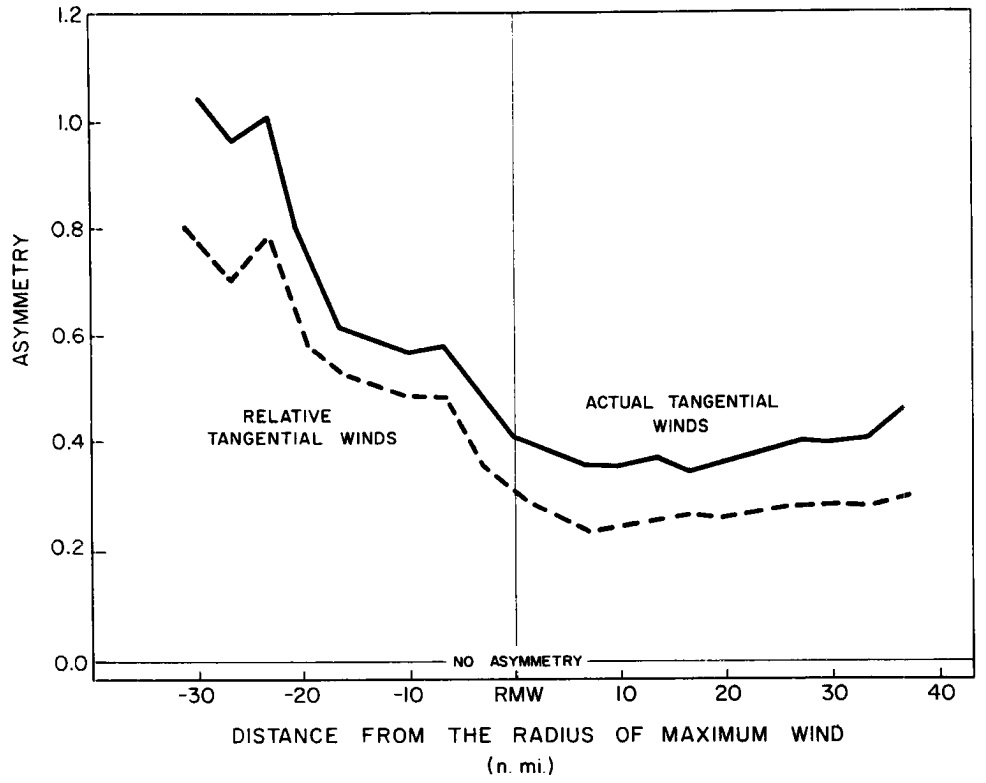

Fig. 47. Asymmetry in the actual and relative tangential winds (method I).

crease in relative humidity from 90 percent at 900 mb to 70 percent at 500 mb; (b) well inside the RMW where subsidence is present (i.e., at the RMW - 7 n.mi. and at the RMW - 20 n.mi.) there is a linear decrease in relative humidity from 90 percent at 900 mb to 50 percent at 500 mb, based on Jordan's (1957) data; and (c) a uniform surface temperature of 25.5°C at 90 percent relative humidity is present. The cloudy areas exhibit large moist instability ($\partial\theta_e/\partial z < 0$) up to approximately 700 mb. Above this a marked increase in moist stability ($\partial\theta_e/\partial z > 0$) is noted. Clearly, the instability decreases as the RMW is approached, i.e.,

$$\frac{\partial \theta_e (\text{RMW} + 20)}{\partial z} < \frac{\partial \theta_e (\text{RMW})}{\partial z} < 0$$

As noted by Sheets (1969) this is probably due to the stronger cumulus activity near the RMW which acts to decrease the convective instability. Even if a relative humidity of 100 percent is assumed at all levels at the RMW the shape of the θ_e profile is not significantly altered between 900 and 500 mb (See Fig. 48). Individual storm profiles determined at the RMW also exhibit these features (Fig. 49). These figures clearly show that the air in cloudy regions does not have a constant equivalent potential temperature with elevation as would be the case if the hurricane had a moist-adiabatic lapse rate everywhere.

Well inside the RMW where subsidence is present only a slight decrease of θ_e with elevation is noted in the 850 to 500 mb layer. Below 850 mb more pronounced instability exists. Equivalent potential temperature profiles drawn using Jordan's (1961) typhoon eye data (Fig. 50) show similar features up to 500 mb. Both Figs. 48 and 50 may be used to explain the low level cumulus cloudiness which is often observed in the hurricane eye. Deeper convection in the eye is inhibited by subsidence which produces middle level dryness. This causes rapid erosion of any cumulus towers. At times some middle level 'forced' layered clouds are found. These are believed to be due to anomalous inflow from the eye wall cloud.

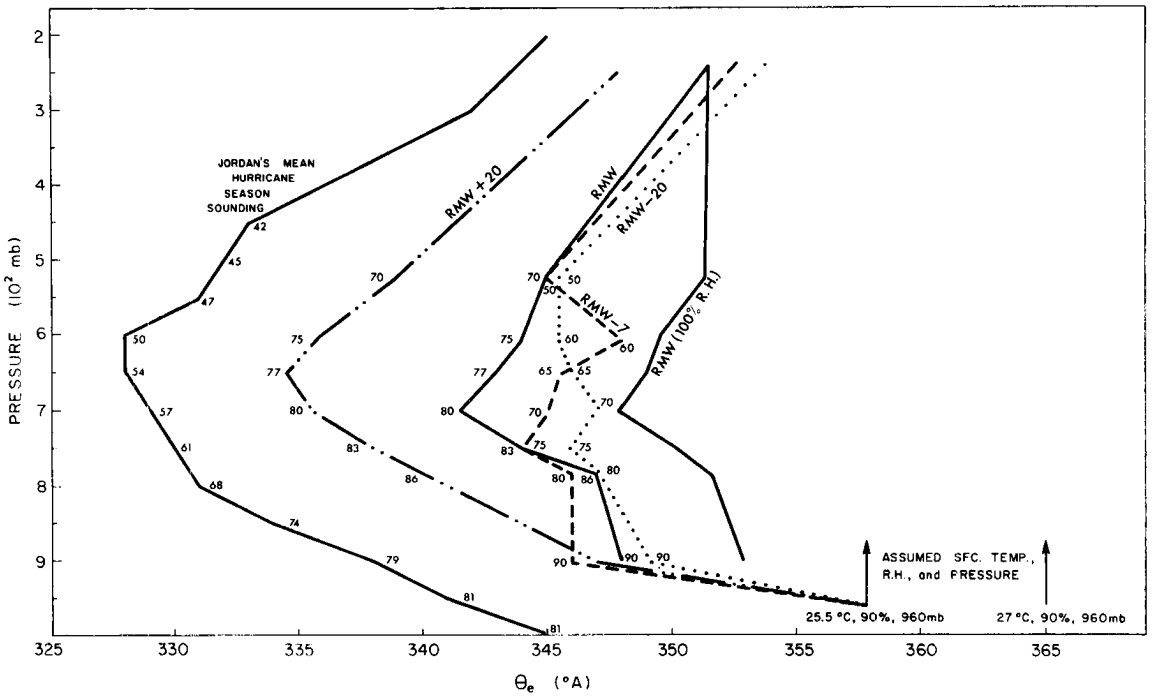

Fig. 48. Equivalent potential temperature (θ_e) profiles at several radii in the mean symmetric storm. Jordan's (1958a) mean hurricane season sounding is provided as a reference. The assumed relative humidities are indicated.

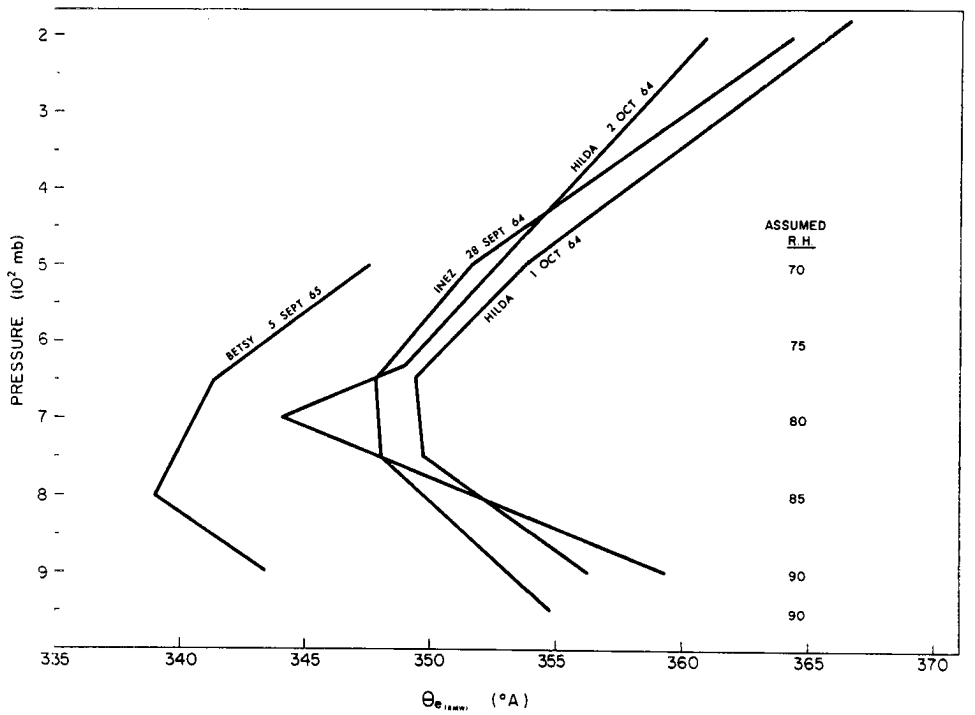

Fig. 49. Equivalent potential temperature (θ_e) profiles at the RMW for several individual storms. The assumed relative humidities are shown.

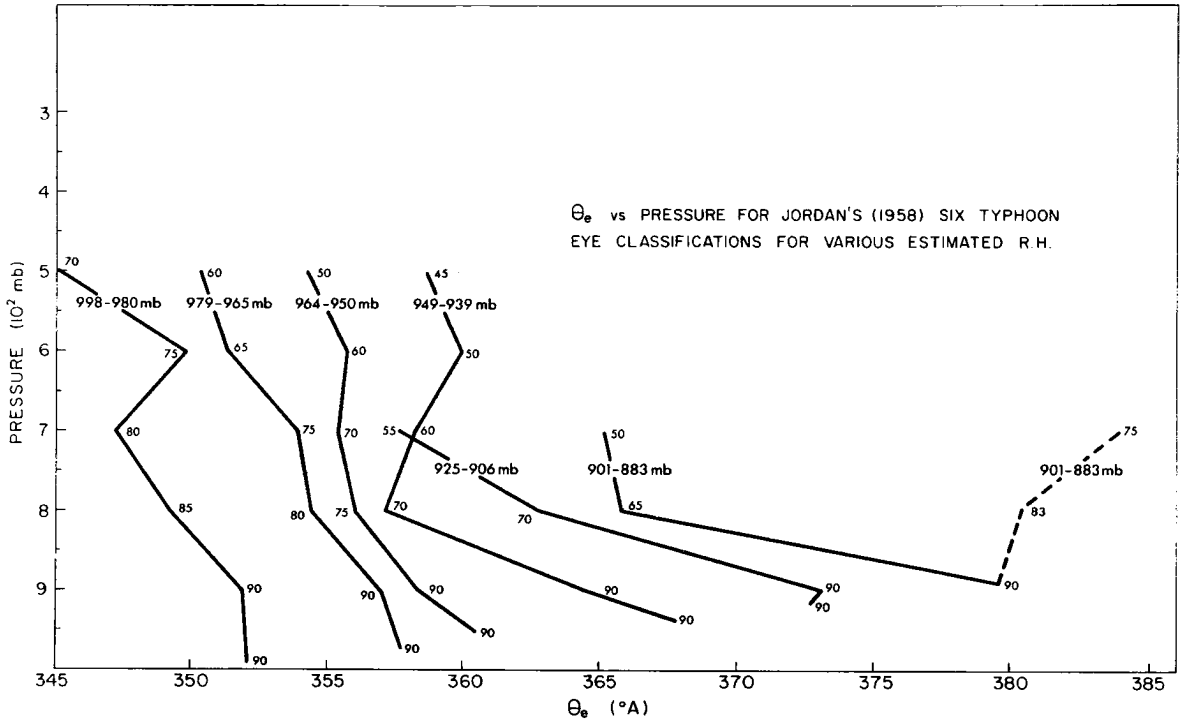

Fig. 50. Equivalent potential temperature (θ_e) profiles for Jordan's (1958b) six typhoon classifications. The dashed line shows the sensitivity of the lapse rate to different relative humidities. (The surface temperature for the 964-950 mb storm has been arbitrarily increased). The numbers shown give the relative humidities.

Schematic

Having discussed the variation of the RMW with elevation, the discrepancy between the inner radar eye radius and the radius of maximum wind, the mean profiles of tangential and radial winds, the D-values, the temperatures and the dynamic computations, we are now in a position to portray a symmetric vortex flow pattern of the hurricane's inner core region. Fig. 51 shows an idealized vertical cross section of this area. The dashed lines portray the mean D-value pattern for the lower half of the troposphere (900-500 mb). The dotted lines portray the mean temperature profile for the upper (240 mb) and lower levels (900-500 mb). Finally, the horizontal and vertical arrows portray the radial and vertical wind velocities. Although no radial winds have been presented for the 240 mb level, Simpson and Starrett (1955) have inferred the existence of a cyclonic indraft at very high levels over the eye.

Fig. 52 presents an idealized view of the lower half of the troposphere. Note that (1) the largest ascending vertical motions occur at the RMW and (2) the 'hump' in temperature inside the inner cloud wall corresponds to subsidence warming.

As previously mentioned the radial winds in the lowest level (900 mb) are directed outwards everywhere inside the RMW and inwards outside this radius. The result of these motions is the very large convergence and vertical velocities at and just outside the RMW as

shown in Figs. 45 and 46. The outward directed radial winds inside the eye are necessary to assure mass balance.

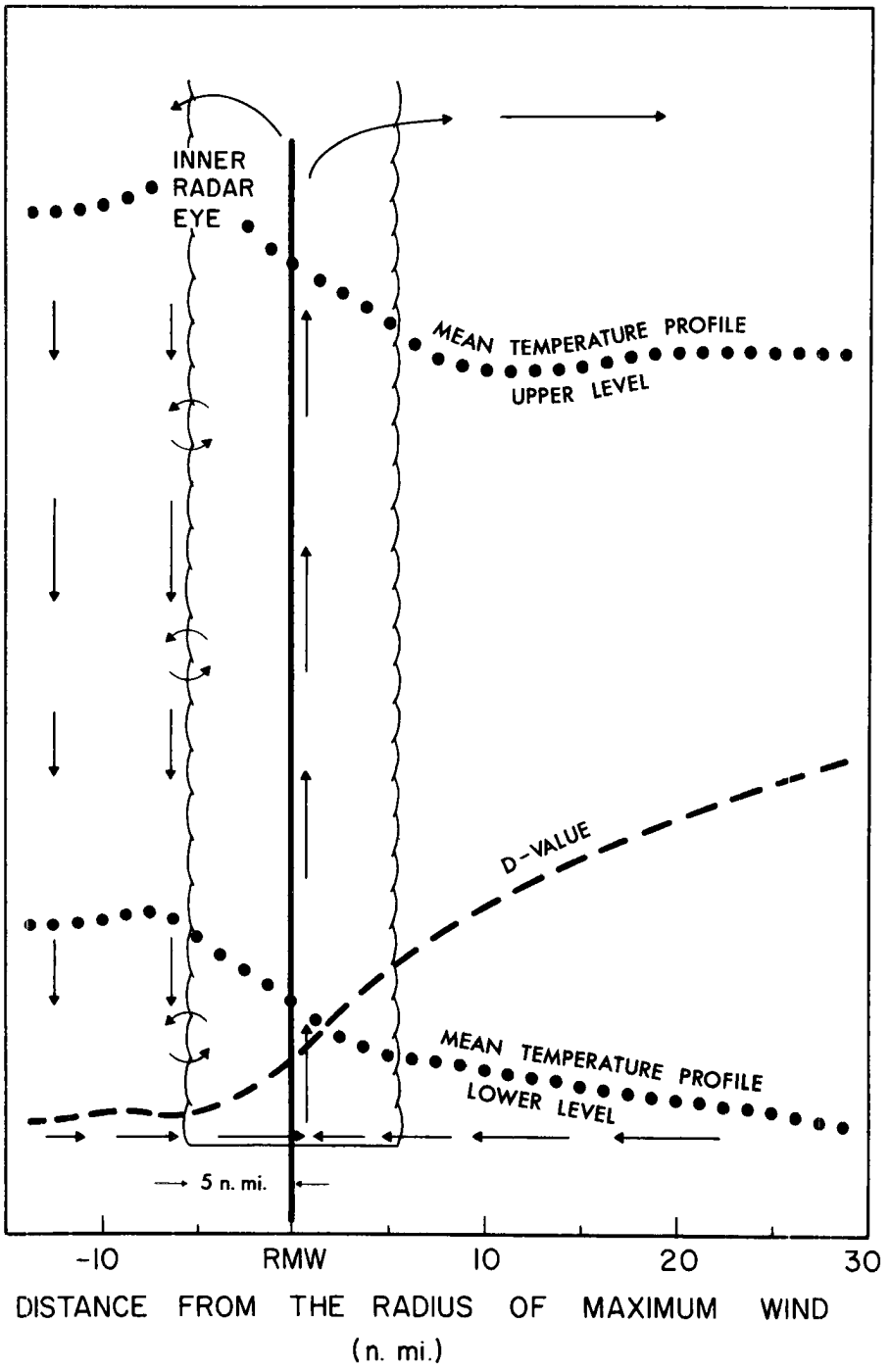

Fig. 51. Portrayal of the mean flow conditions in the hurricane's inner core region. The horizontal and vertical arrows represent the radial and vertical velocities, respectively. Mean D-value and temperature profiles are as indicated.

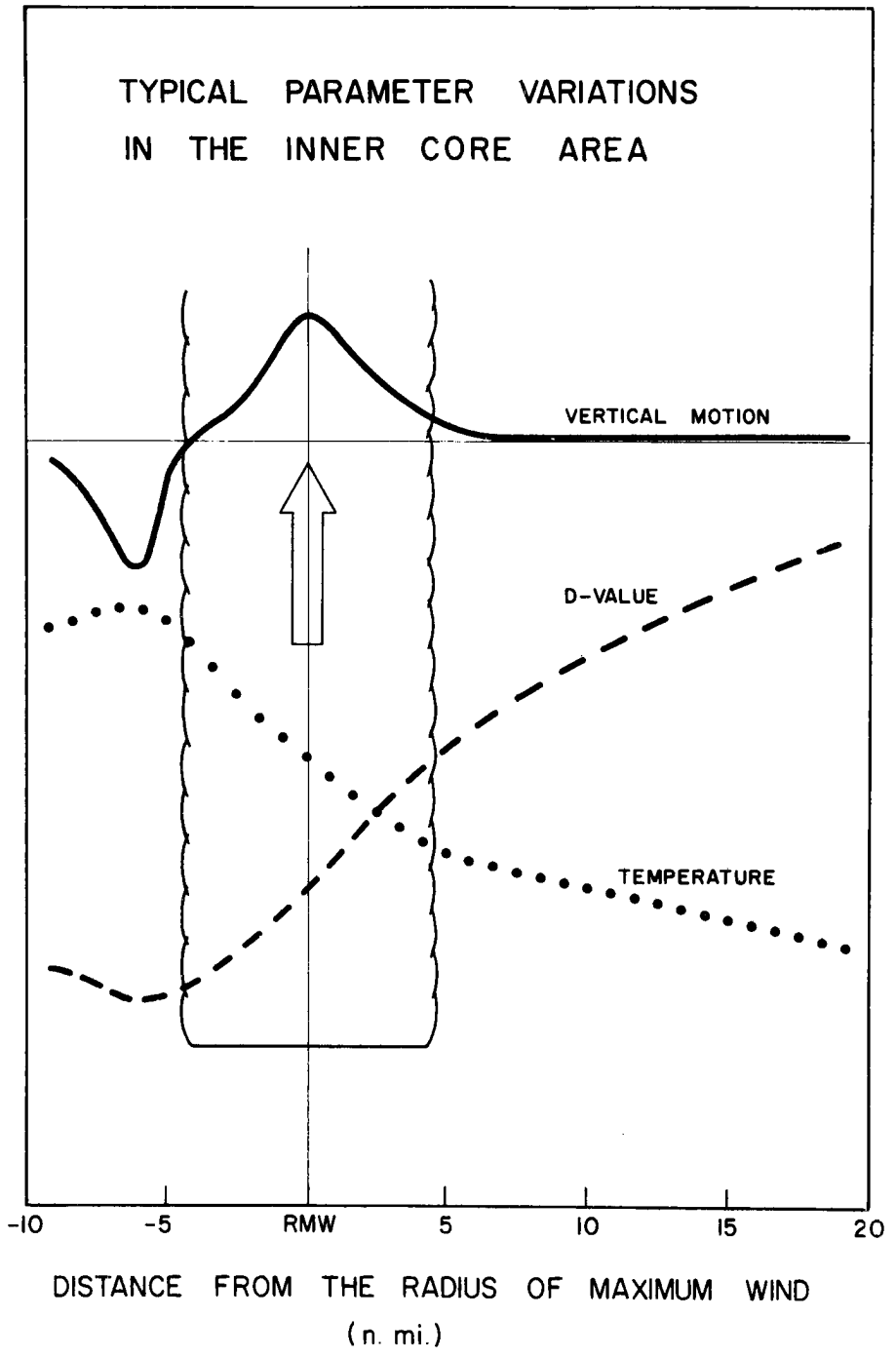

Fig. 52. Idealized portrayal of the mean flow conditions in the lower half of the troposphere.

IV. STRUCTURE OF THE MEAN ASYMMETRIC STORM

The structure of the mean asymmetric storm is exhibited in a series of plan views. These plan views present the mean data with respect to the Radius of Maximum Wind (RMW) for distances from 20 n. mi. inside the RMW to 30 n. mi. outside the RMW[12].

Actual Tangential Winds. The actual radial winds are shown in Figs. 53a-e. Note the large degree of asymmetry. At all levels the strongest wind speeds are to the right of the storm motion and the weakest speeds to the left. This is, of course, partly due to the super position of the storm speed upon the wind field. At larger radii, Hughes (1952), Miller (1958), Izawa (1964) and Black and Anthes (1971) also show large asymmetries in the winds.

Actual Radial Winds. The actual radial winds are shown in Figs. 54a-d. The 900 mb level shows the largest inflow both in area and in magnitude. Most of the inward motion takes place in the south and east quadrants. The higher three levels show approximately equal areas of inflow to the south and outflow to the north of the storm motion. Most of the inflow and outflow cancels when the storm motion is subtracted from the data.

Relative Tangential Winds. The relative tangential winds are shown in Figs. 55a-e. As might have been expected the relative tangential winds are more symmetric than the actual tangential winds. There still

---

[12] Due to averaging these plan views lack the striations so often observed in individual storms.

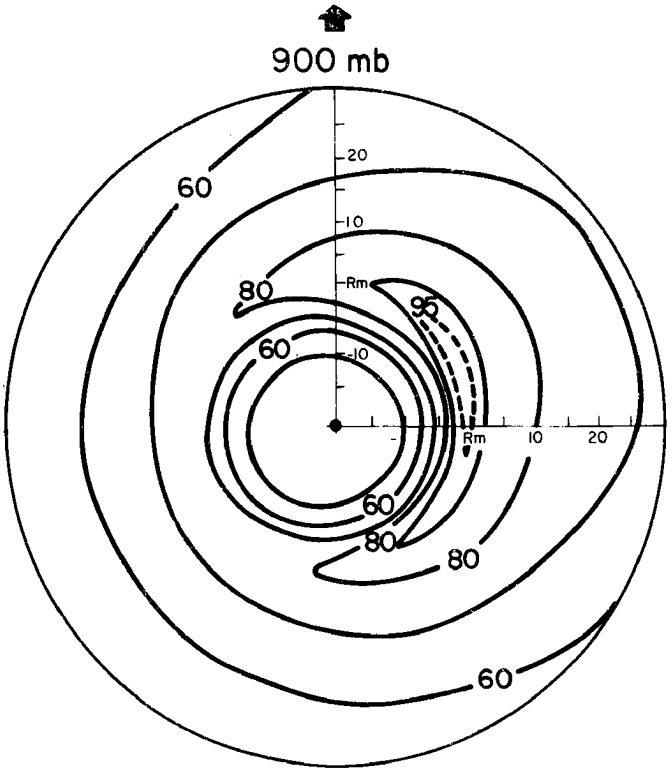

Fig. 53a.

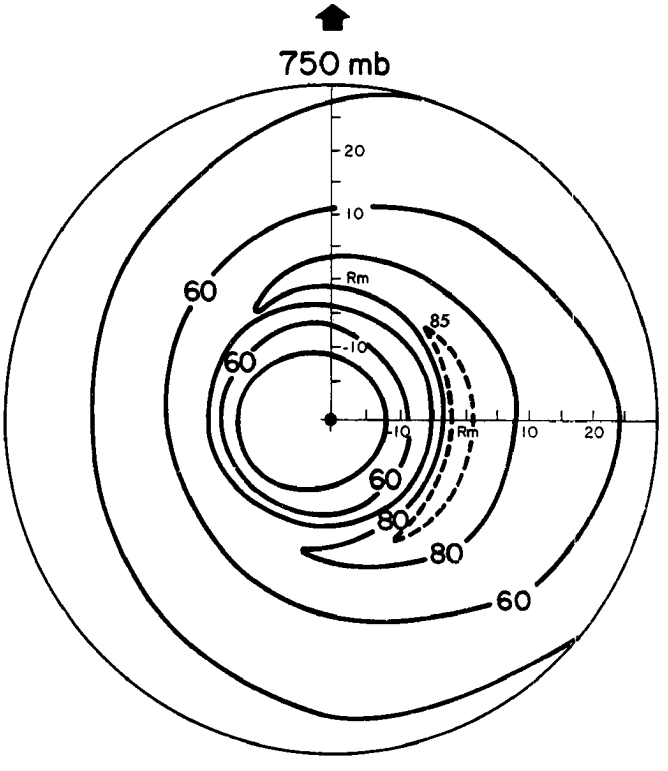

Fig. 53b.

Figs. 53a-e. Plan view of actual tangential winds with respect to RMW (kts; method I). The arrow indicates the direction of storm movement. Distance from the RMW is indicated in n. mi.

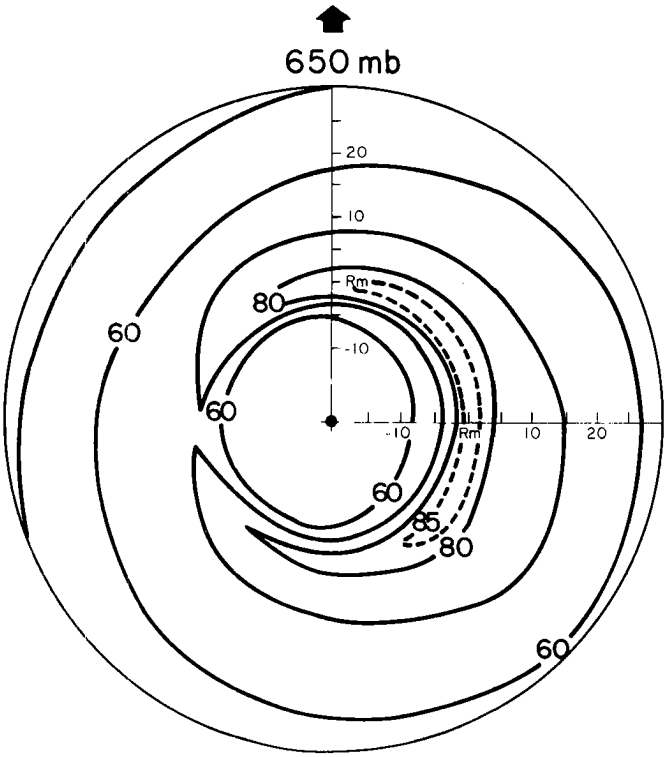

Fig. 53c.

Fig. 53d.

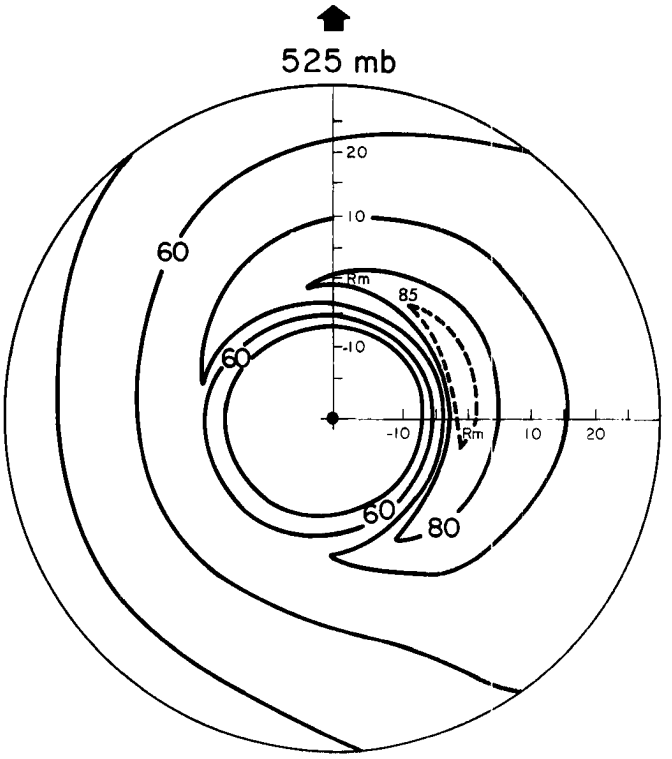

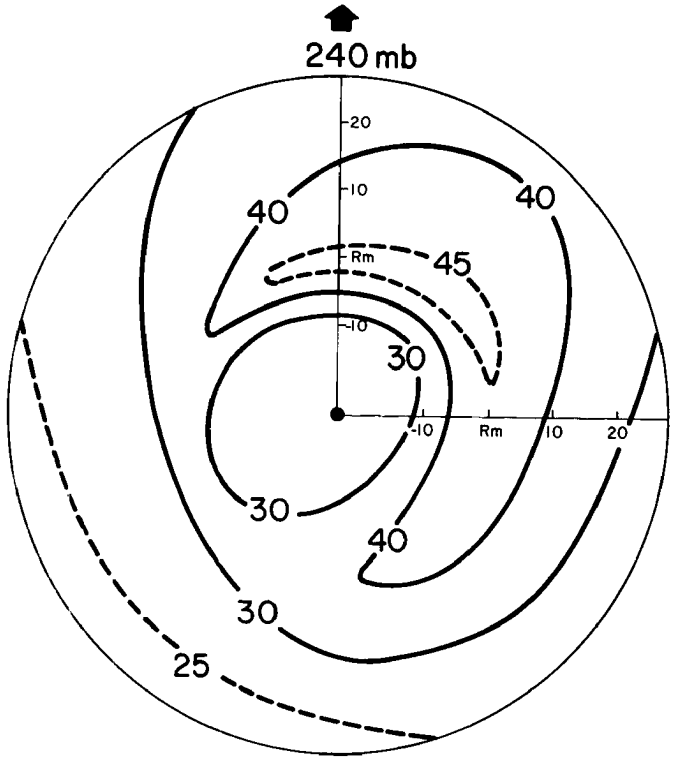

Fig. 53e.

is, however, a maximum to the right of the storm motion. Individual case studies also show this [e.g., Jordan, et al. (1960)].

This asymmetry in hurricane tangential wind (even after the storm motion has been subtracted out) has been discussed by Sherman (1956). He noted that the difference in wind speed between winds to the right of the storm and those to the left is sometimes two or three times the storm velocity.

Relative Radial Winds. The relative radial winds are shown in Figs. 56a-d. At 900 mb inflow is present beyond the RMW especially to the right of the storm's motion and outflow is present inside the eye. A weak mixed pattern exists at the middle three levels.

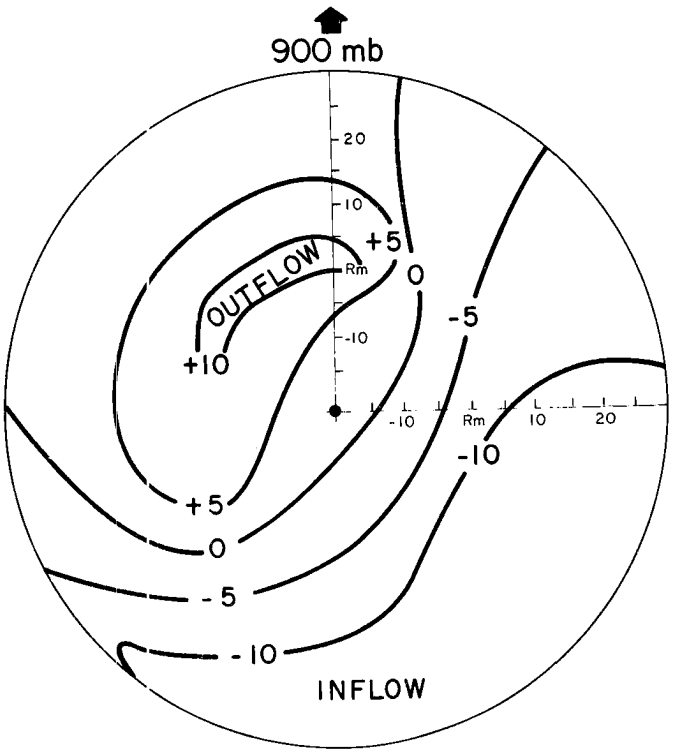

Fig. 54a.

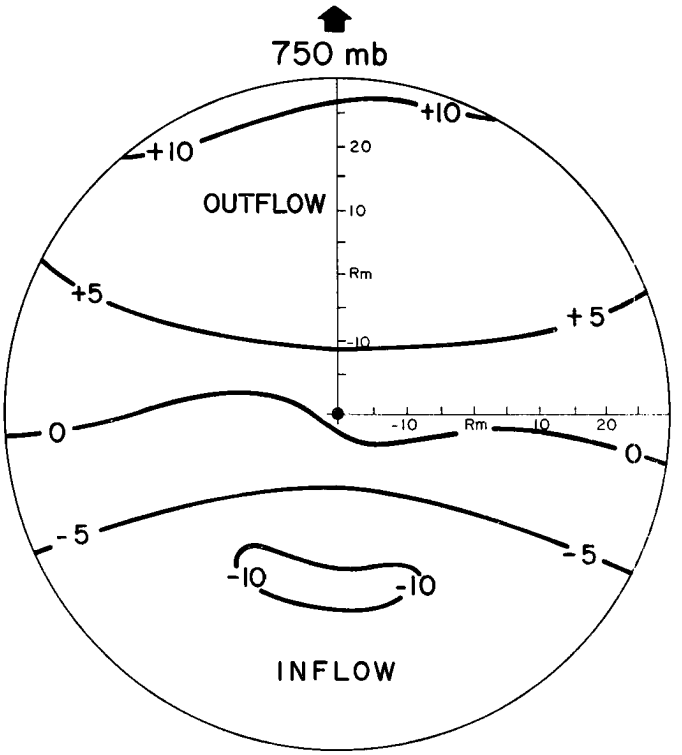

Fig. 54b.

Figs. 54a-d. Plan views of actual radial winds (kts; method I). The arrow indicates the direction of storm movement. Distance from the RMW is indicated in n. mi.

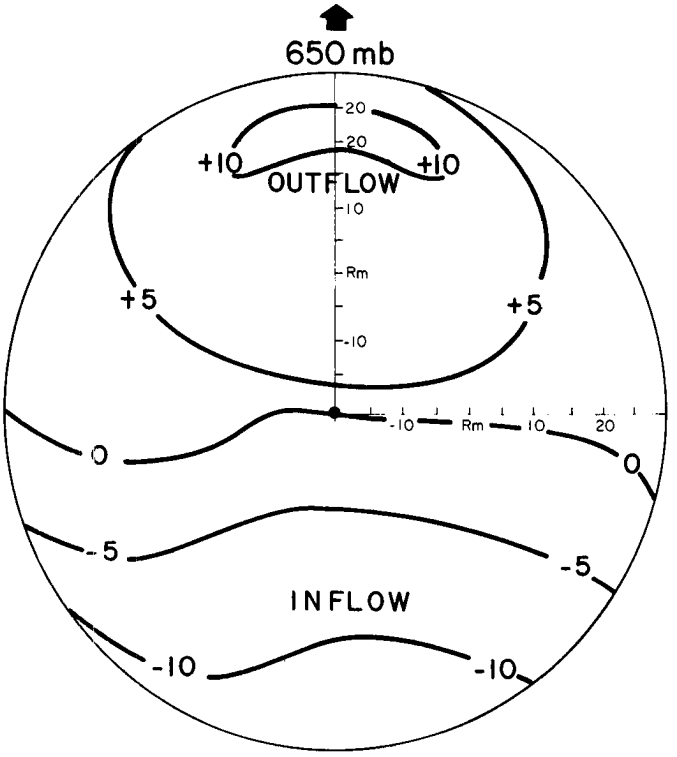

Fig. 54c.

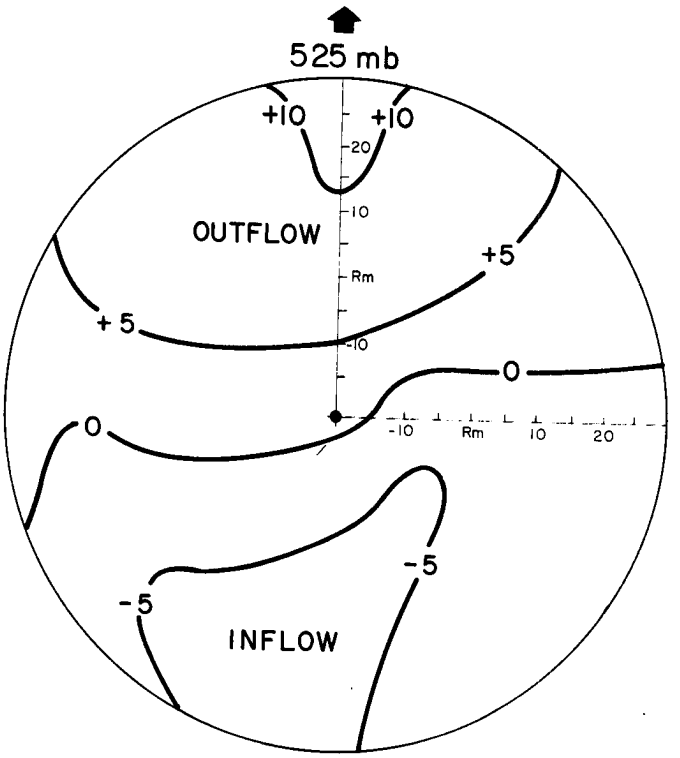

Fig. 54d.

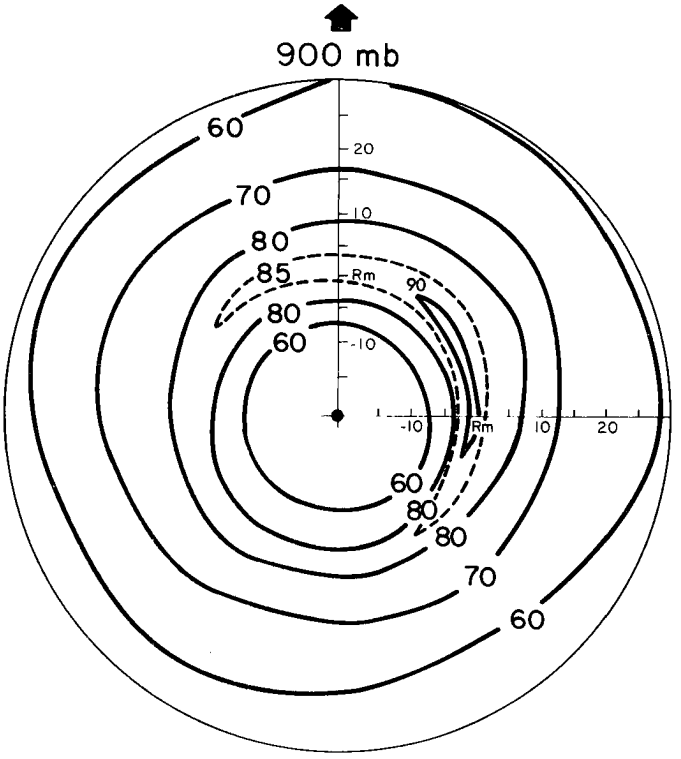

Fig. 55a.

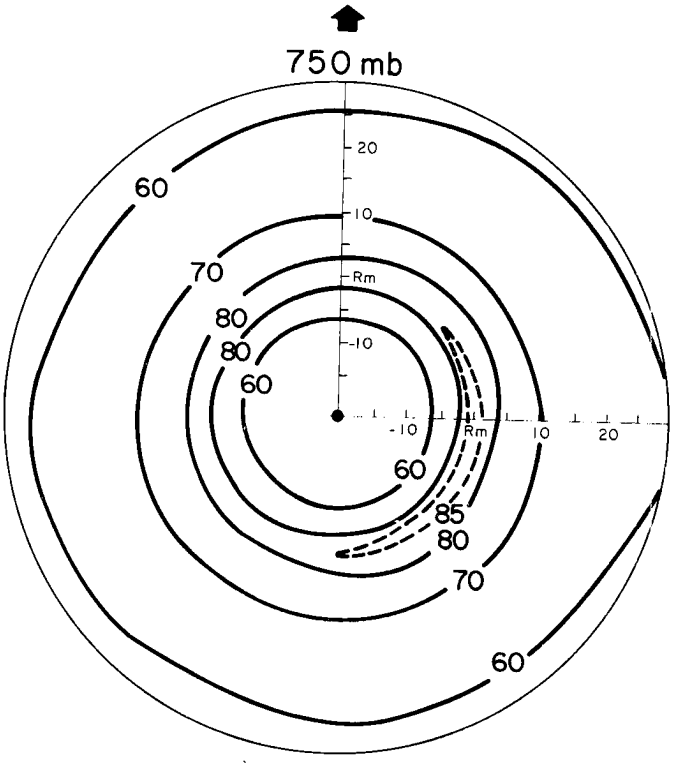

Fig. 55b.

Figs. 55a-e. Plan views of relative tangential winds (kts; method I). The arrow indicates the direction of storm movement. Distance from the RMW is indicated in n. mi.

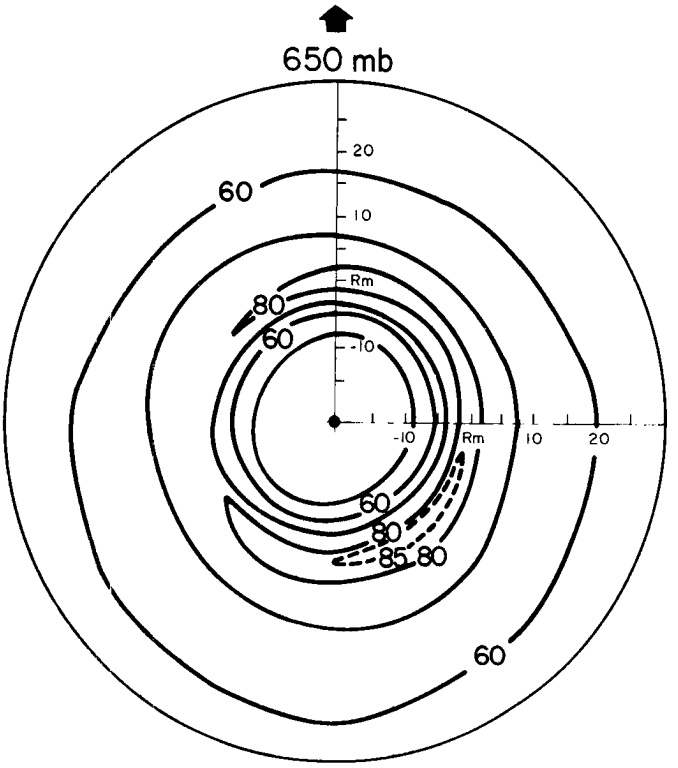

Fig. 55c.

Fig. 55d.

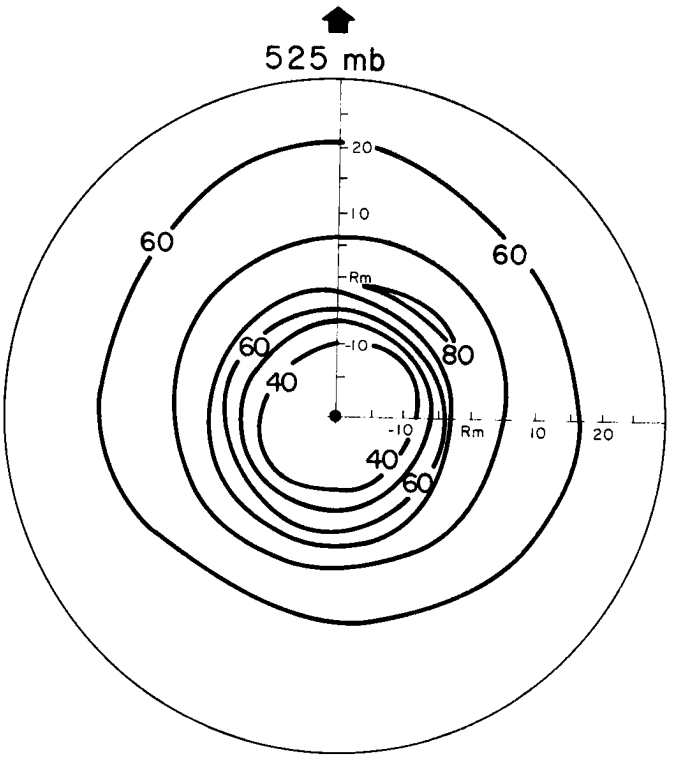

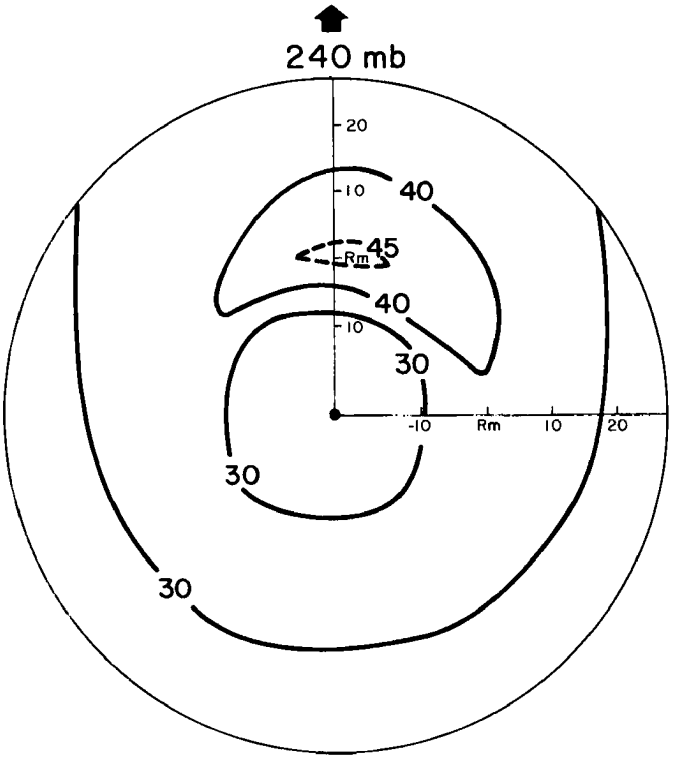

Fig. 55e.

D-Value Profile. D-value patterns are shown in Figs. 57a-d. Because of missing information no D-values are shown at the 240 mb level. By and large the patterns are quite symmetric with the largest gradients concentrated at the RMW.

The much larger asymmetry of the wind field (both V_θ and $V_{\theta r}$) compared to the very symmetric D-value pattern has been noted before in the literature by Gray (1962) and LaSeur and Hawkins (op. cit.). Their studies reported sub-gradient winds to the left and super-gradient winds to the right of the storm motion. Analysis of the present data shows the same results.

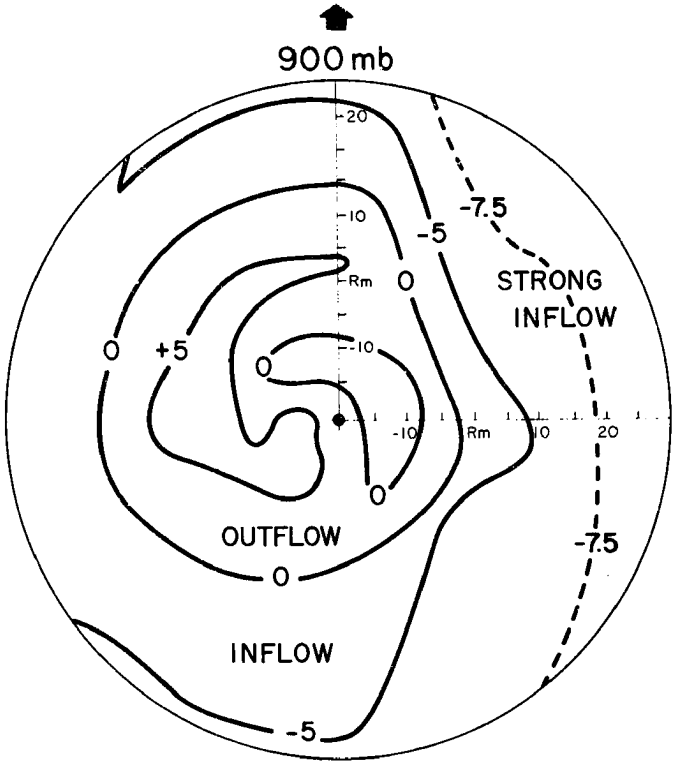

Fig. 56a.

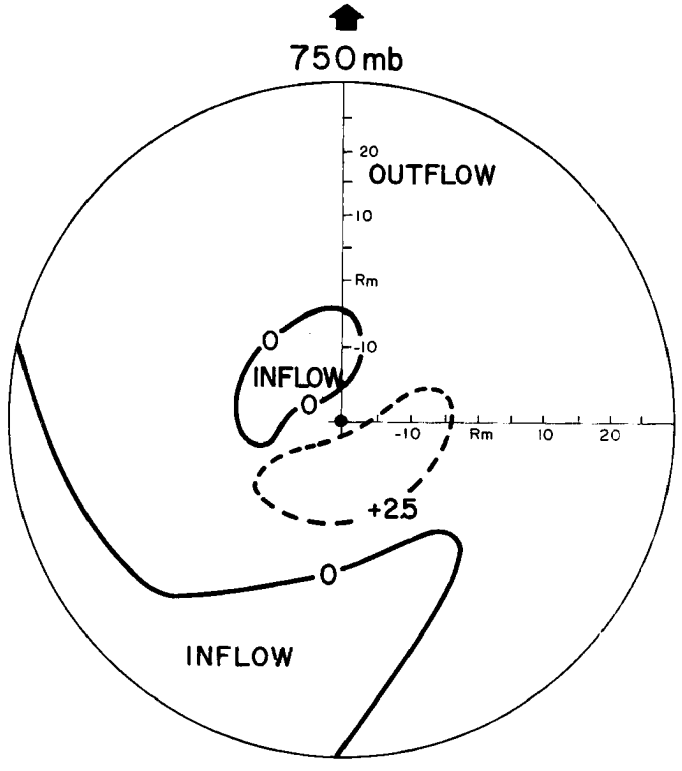

Fig. 56b.

Figs. 56a-d. Plan views of relative radial winds (kts; method I). The arrow indicates the direction of storm movement. Distance from the RMW is in n. mi.

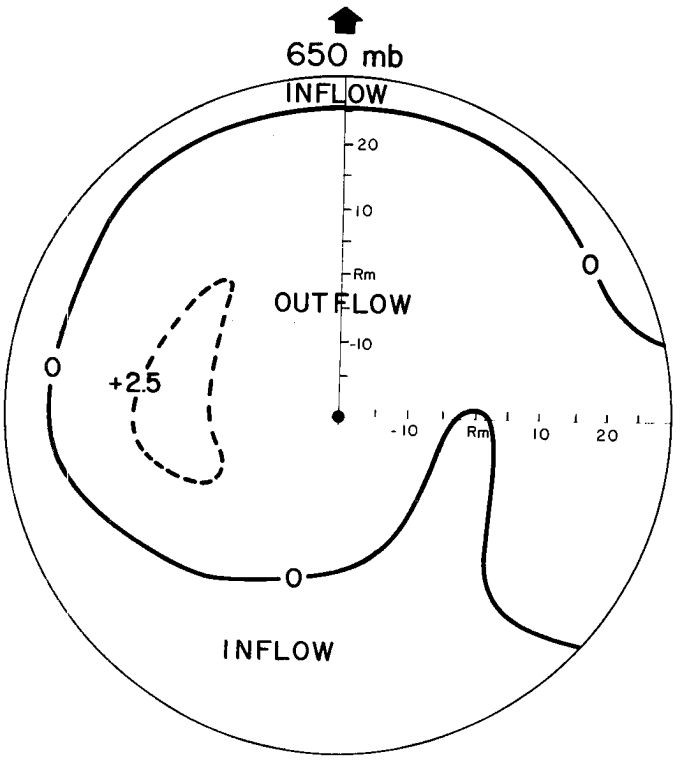

Fig. 56c.

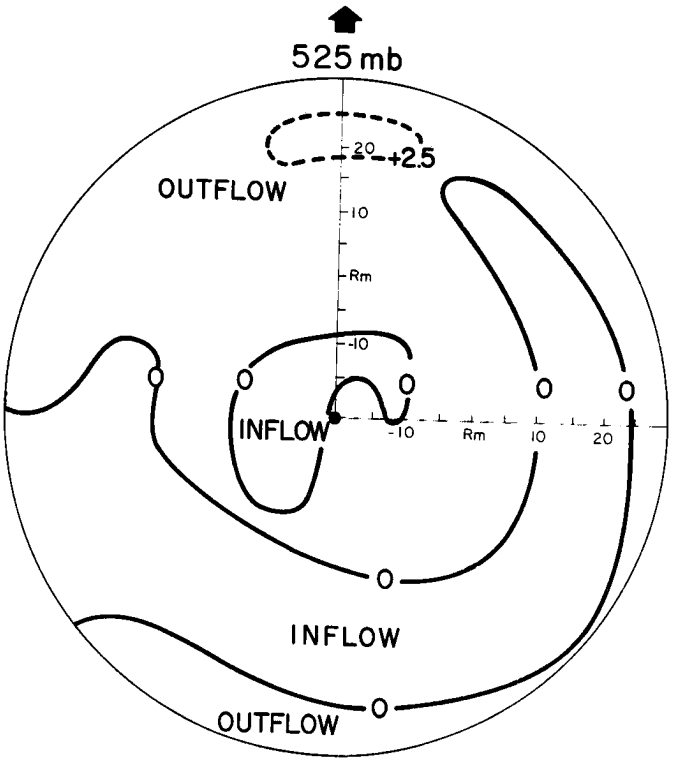

Fig. 56d.

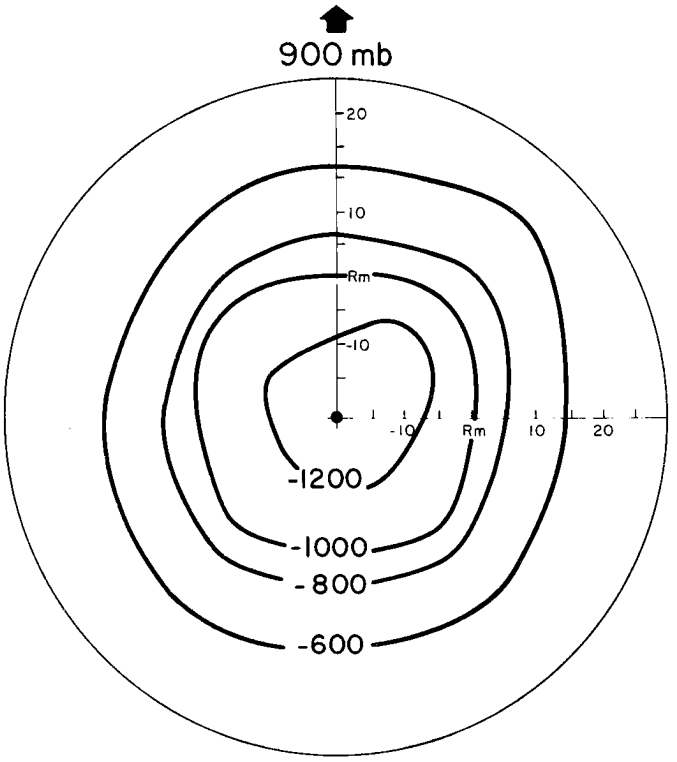

Fig. 57a.

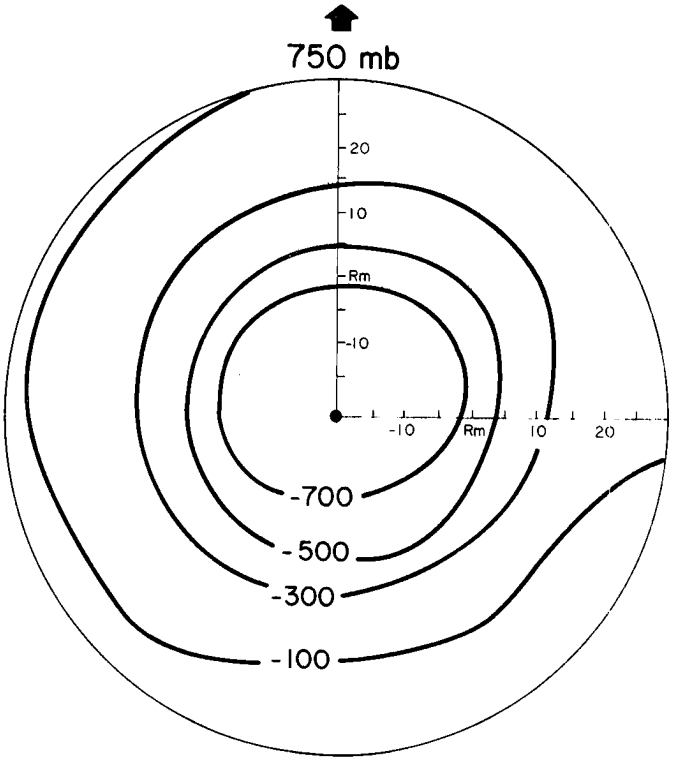

Fig. 57b.

Figs. 57a-d. Plan views of D-value (feet; method I). The arrow indicates the direction of the storm movement. Distance from the RMW is in n. mi.

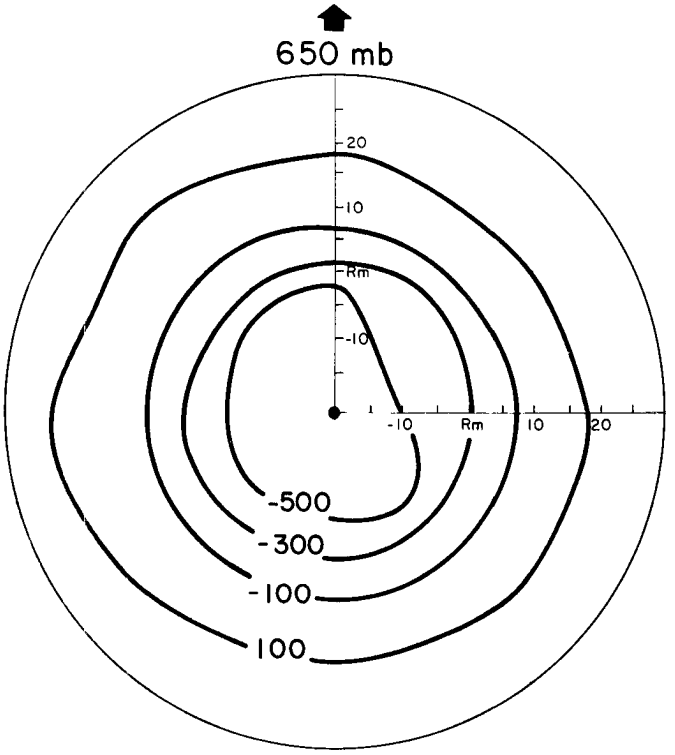

Fig. 57c.

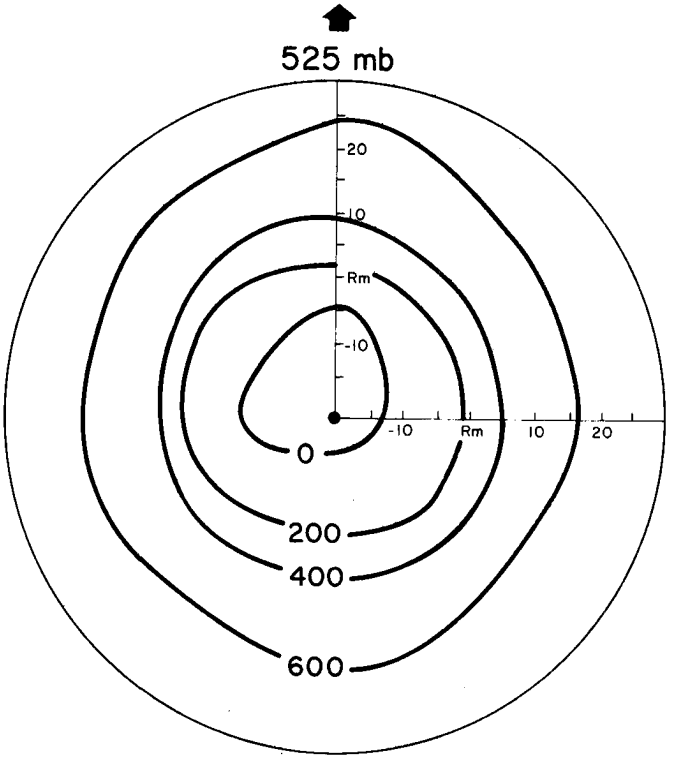

Fig. 57d.

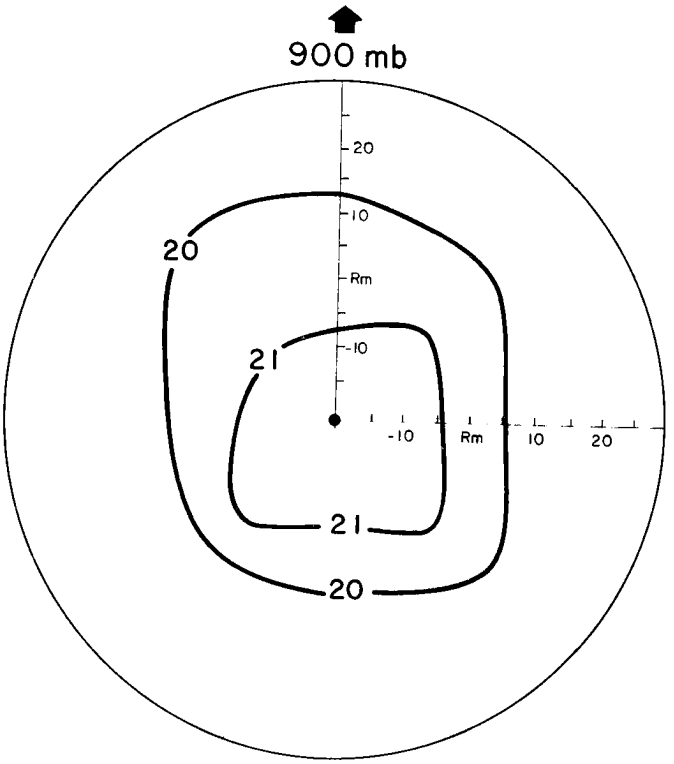

Fig. 58a.

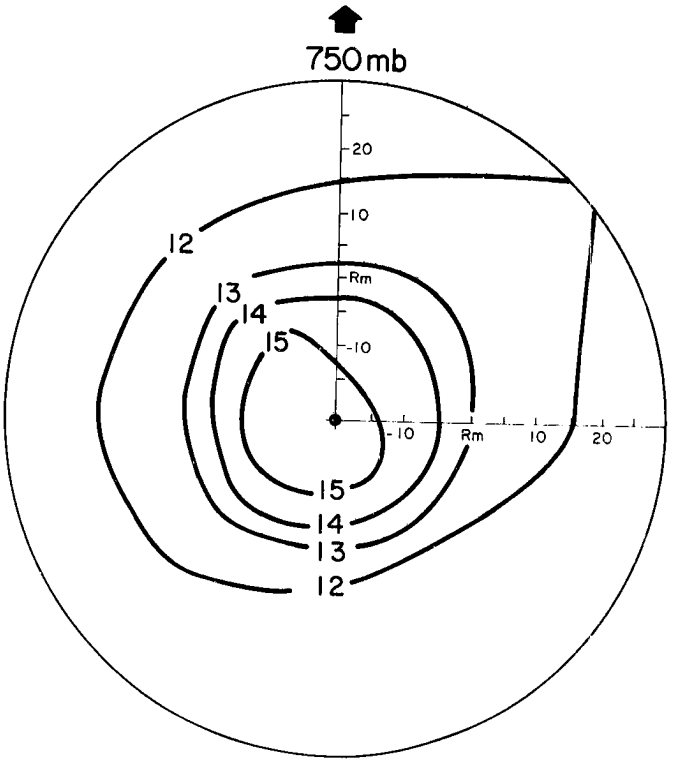

Fig. 58b.

Figs. 58a-e. Plan views of temperature (^{o}C; method I). The arrow indicates the direction of storm movement. Distance from the RMW is in n. mi.

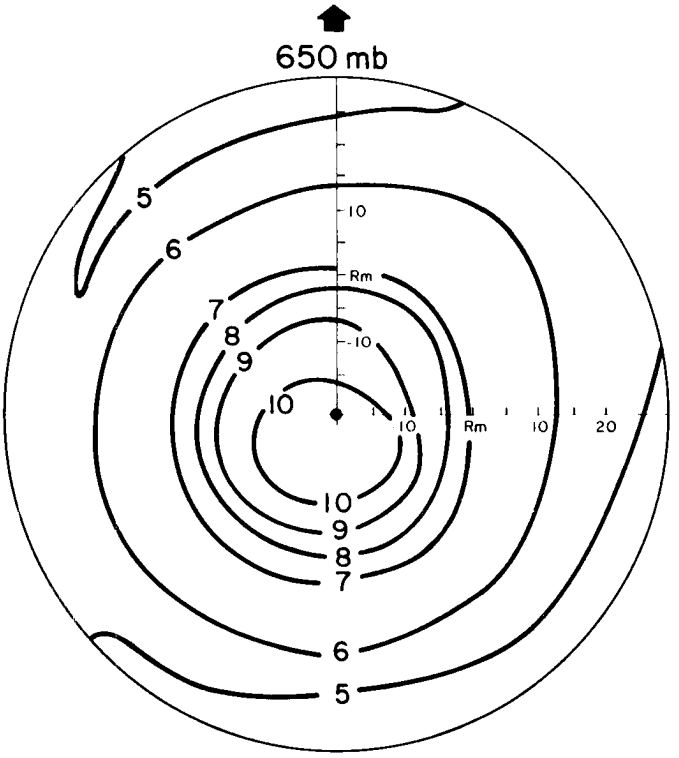

Fig. 58c.

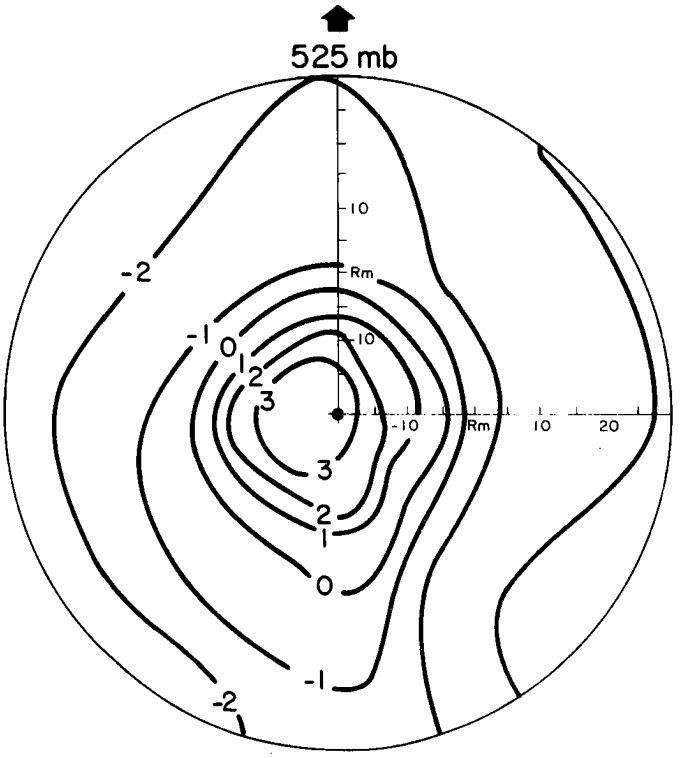

Fig. 58d.

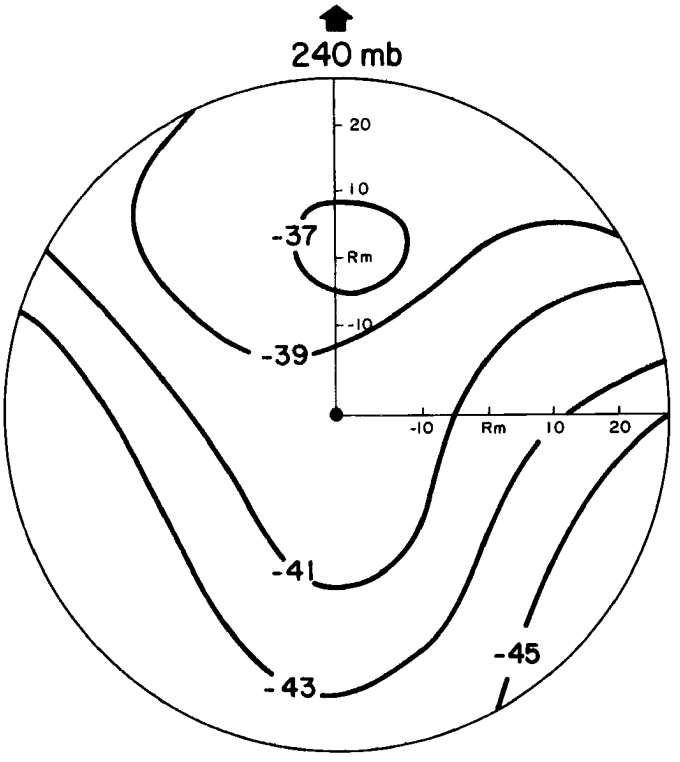

Fig. 58e.

Adjusted Temperature. The adjusted temperatures are shown in Figs. 58a-e. The inward temperature gradients increase with height in the lower half of the troposphere. At 525 mb the average radial temperature gradient is 5°C to 6°C per 45 n. mi. At 250 mb the radial temperature gradients are on the order of 3°C/45 n. mi. The upper warm area at 240 mb in the direction of storm motion is probably due to subsidence and may be initiating the forward warming and pressure falls required in the storm's motion.

V. STORM STRATIFICATIONS

The highly variable character of the hurricane's inner core area has been noted. In order to further investigate this variability, storms have been stratified by their latitude, direction, speed, intensity and growing and filling tendency. Correlations between (1) latitude and maximum winds; (2) latitude and the Radius of Maximum Winds (RMW); (3) maximum winds and the RMW and (4) maximum winds and central pressure have been made.

The structural characteristics of the storms relative to these stratifications is made with the three level storm model only (i.e., 900-700 mb, 700-500 mb and 260-180 mb) because 1) the lower layers exhibit very similar profiles and not much would be gained by presenting a five level storm, and 2) after stratification, the data samples are significantly reduced.

Deepening and Filling Storms. Table 1 shows which storms were listed as deepening or filling. This classification was quite subjective and due to the many short period tendency changes some inaccuracies may be present. Storms were classified as deepening or filling depending on whether their central pressure showed a marked pressure change ($\geq$ 15 mb) from one day to the next. In some cases the storms did not quite satisfy this criteria at the time of observation but they showed a definite tendency towards deepening or filling over a longer period. Steady state storms were not treated since it was felt that the resulting averages would resemble those of the mean storm.

A definite latitude bias is exhibited in this stratification. Most of the deepening storms occurred at low and middle latitudes, whereas the majority of filling storms occurred at high latitudes. The filling at higher latitudes is largely due to the colder waters and reduced cumulus activity. There were too few filling storms at low latitudes to give a meaningful data sample. The deepening storms were slightly more intense than the filling storms.

With these criticisms in mind, wind profiles for the lower two layers in the deepening and filling storms are presented in Figs. 59 and 60. Note the difference in vertical shears. Deepening storms have almost identical lower and middle profiles. In contrast, the filling storms, although they exhibit similar profiles, have much larger vertical shears. This is probably due to a lessening of cumulus convection in these storms. The higher momentum from low levels is not being distributed in the vertical. (It might be possible to make operational predictive use of this observation). Profiles for the upper level ($\sim$ 240 mb) are not presented due to the small data sample.

Adjusted temperature profiles are presented in Fig. 61. Little difference can be seen between the deepening and filling storms. If, however, we take the deviation of each temperature from the mean temperature at the RMW (See Figs. 62 and 63) we see that the temperature deviations in the middle level for the deepening storms are exceptionally large compared to the filling storms. Obviously the thermal wind will not be in balance.

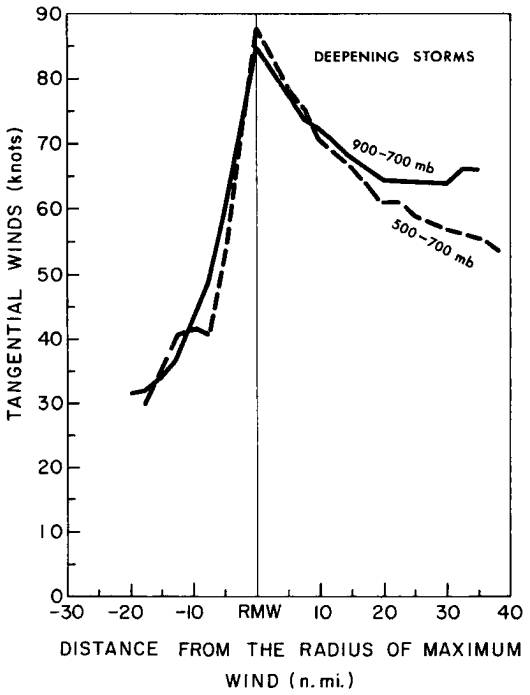

Fig. 59. Tangential wind profiles for deepening storms (method I).

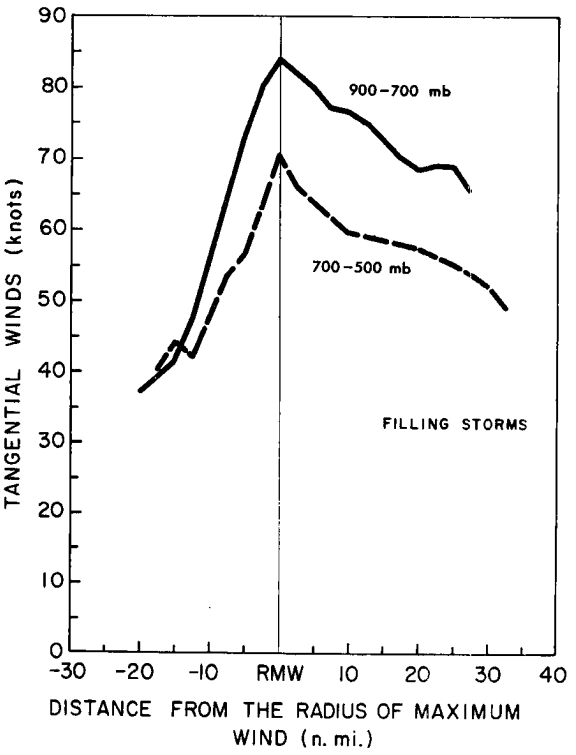

Fig. 60. Tangential wind profiles for filling storms (method I).

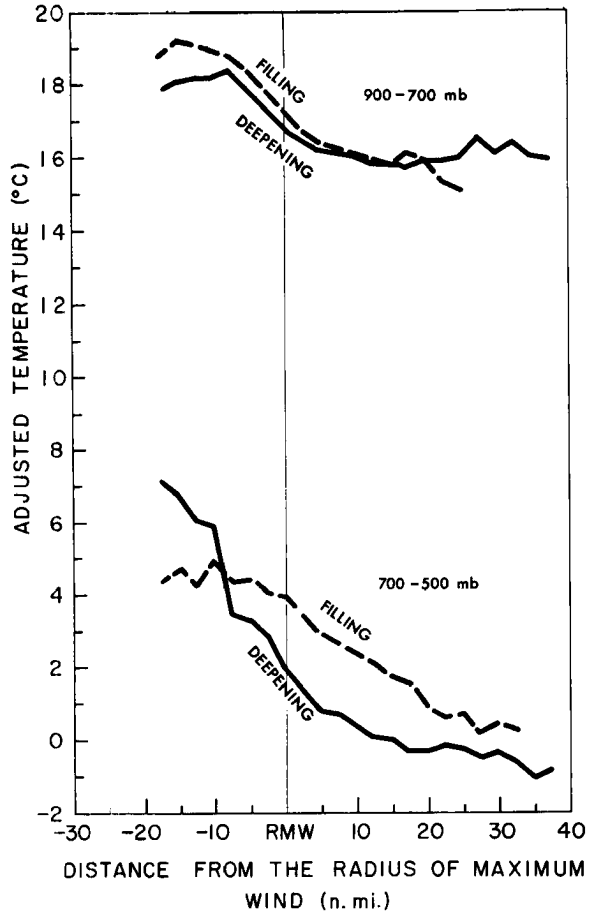

Fig. 61. Adjusted radial temperature profiles for deepening and filling storms (method I).

Equivalent potential temperature (θ_e) profiles at the radius of maximum winds for each storm classification are shown in Fig. 64. The filling storms are convectively unstable only in a shallow layer up to 800 mb. Above this level there is a marked increase in stability. Deepening storms exhibit a deep convectively unstable layer up to 625 mb. Stable conditions exist above this level. It is obvious that the deepening storms possess the potential to have more convection than either the filling storms or the mean storm (See Fig. 48.).

Stratification of Storms by Latitude. Storms were next stratified by latitude. Comparison was made of storms at latitudes less than

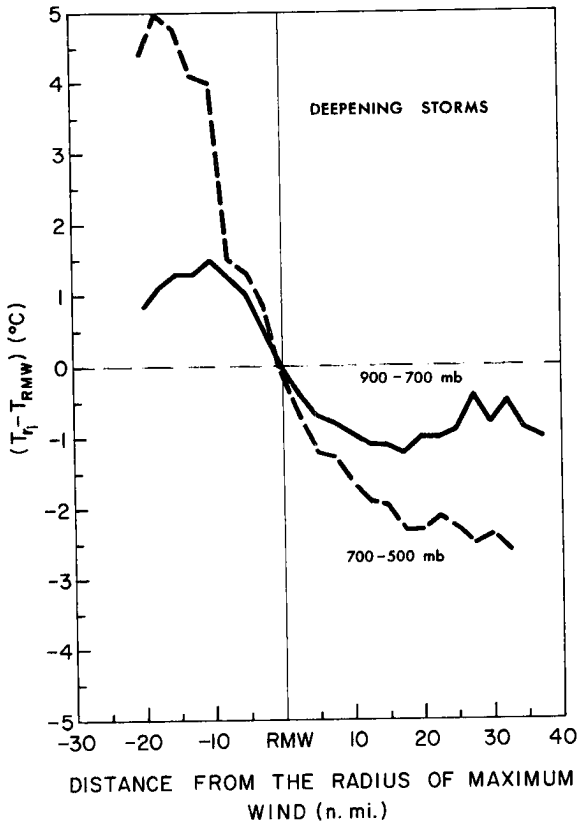

Fig. 62. Deviations of individual mean adjusted temperatures (T_{r_i}) from the mean adjusted temperature at the RMW for the deepening storms.

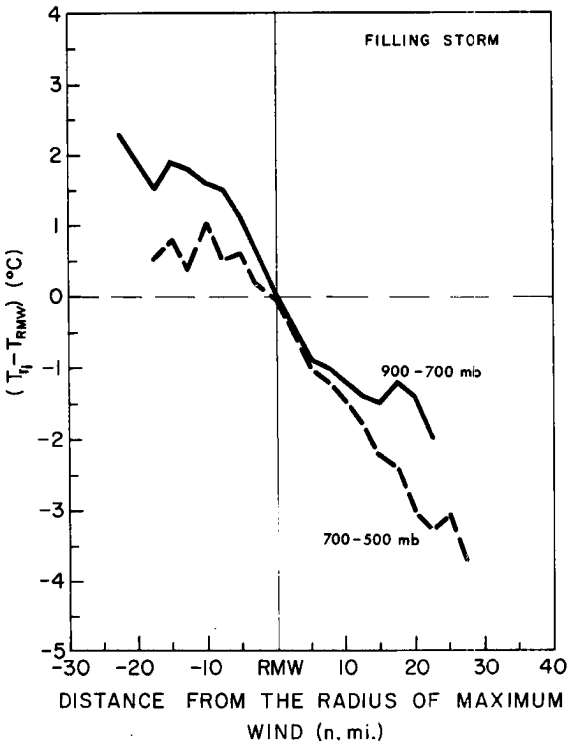

Fig. 63. Deviations of individual mean adjusted temperatures (T_{r_i}) from the mean adjusted temperature at the RMW for the filling storms.

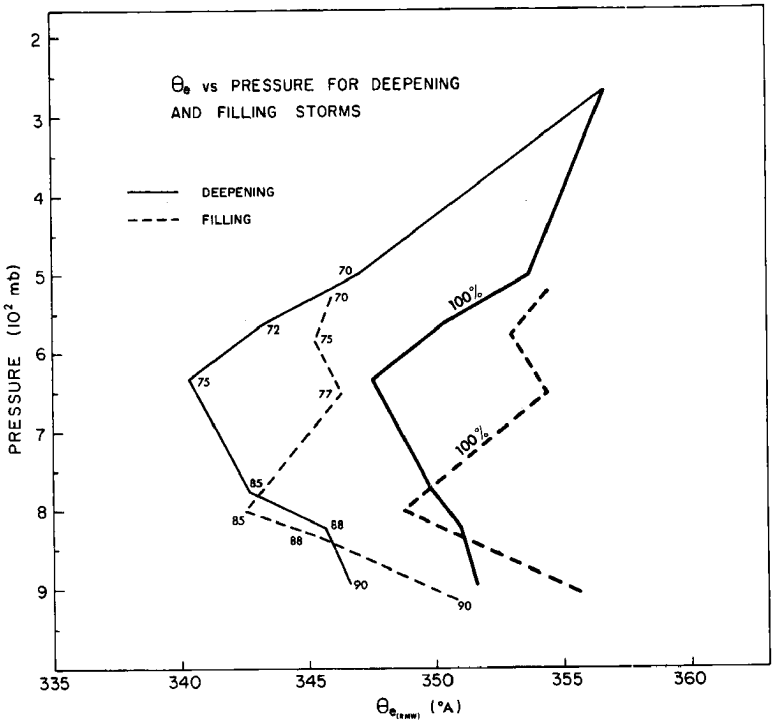

Fig. 64. Equivalent potential temperature (θ_e) profiles at the RMW for deepening and filling storms. The numbers indicate the assumed relative humidities at each level.

22^{o} with those at latitudes greater than 30^{o} (a third of the data fit into each of these categories).

The wind profiles for the lower and middle levels for each storm category are shown in Figs. 65 and 66. Two important features are noted. First, the wind profiles for the lower latitude mean storm are much sharper and the winds are more intense than the corresponding profiles for the higher latitude storms. Second, the vertical wind shears for the higher latitude storms are larger. Again, the greater eye wall convection of the lower latitude storms is more effective in reducing the vertical wind shears.

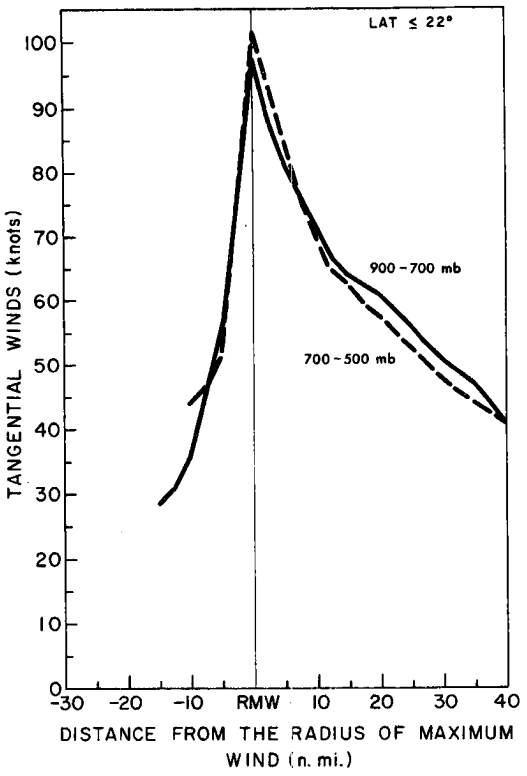

Fig. 65. Tangential wind profiles for lower latitude storms (method I).

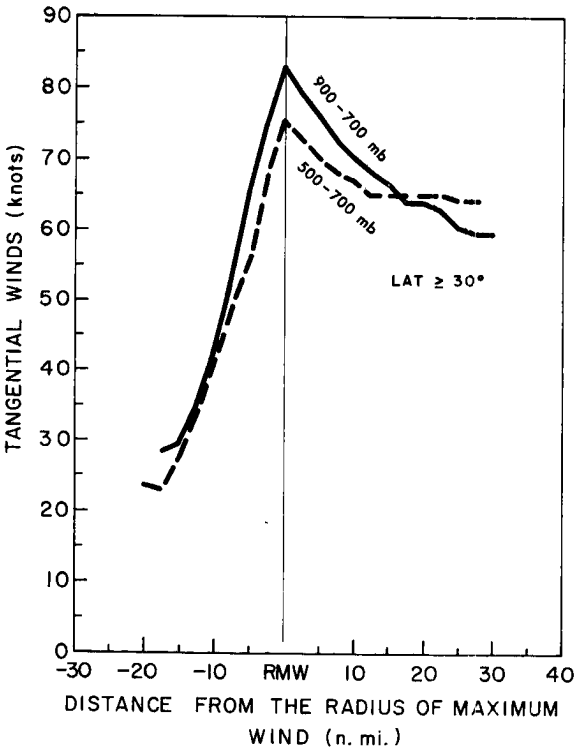

Fig. 66. Tangential wind profiles for higher latitude storms (method I).

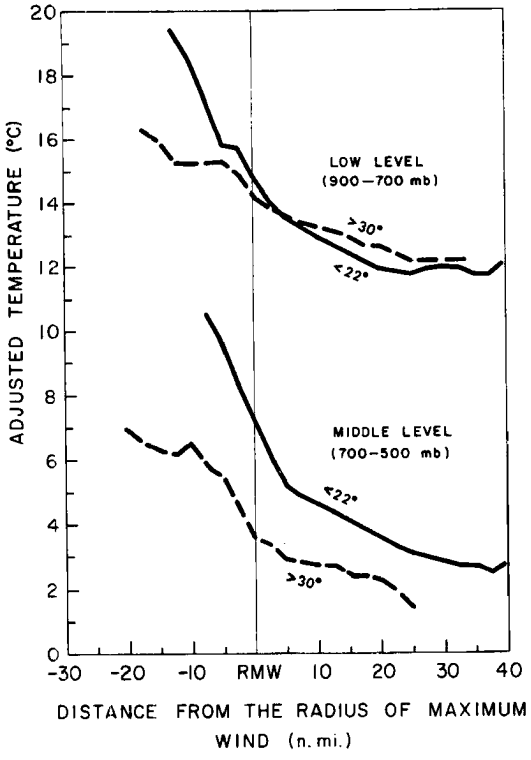

Fig. 67. Adjusted radial temperature profiles for lower and higher latitude storms (method I).

Temperature profiles are shown in Fig. 67. The temperature increase of the lower latitude storms is larger than the increase at higher latitudes. This is due to air rising with warmer equivalent potential temperature at lower latitudes.

Intense, Moderate and Weak Storms. Using central pressures, storms were classified as to whether they were weak (central pressures $\geq$ 965 mb), moderate (945 mb $\leq$ central pressure $\geq$ 965 mb) or intense (central pressure $\geq$ 945 mb). The results show what might be expected. The winds, temperature gradients and D-value gradients were larger in storms with lower central pressures.

Figs. 68-70 show the wind profiles for weak, moderate and intense storms, respectively. Note the very pronounced peaks on the wind

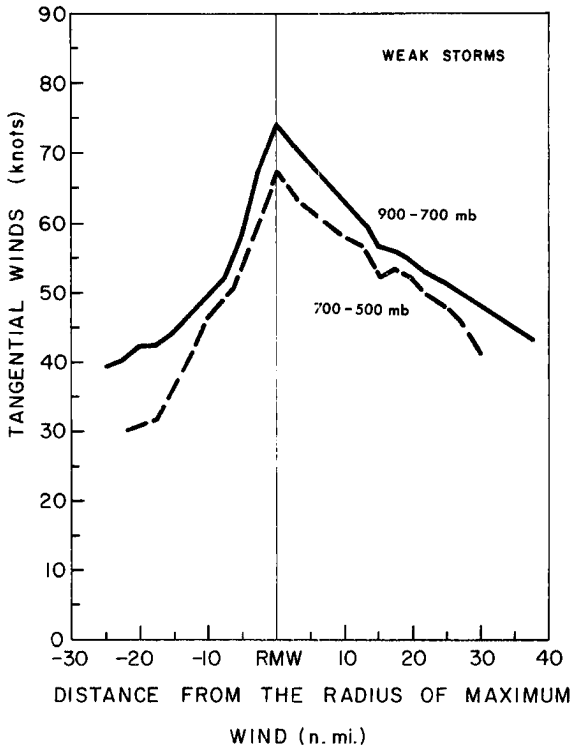

Fig. 68. Tangential wind profiles for weak storms (method I).

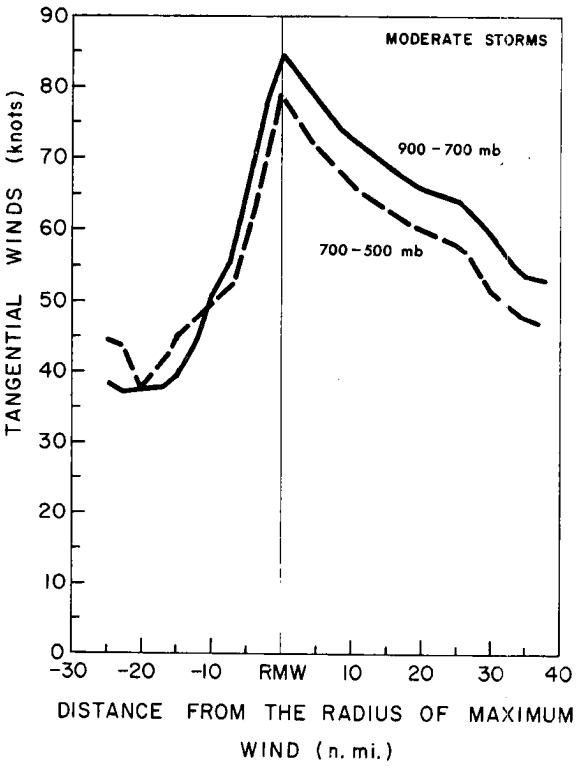

Fig. 69. Tangential wind profiles for moderate storms (method I).

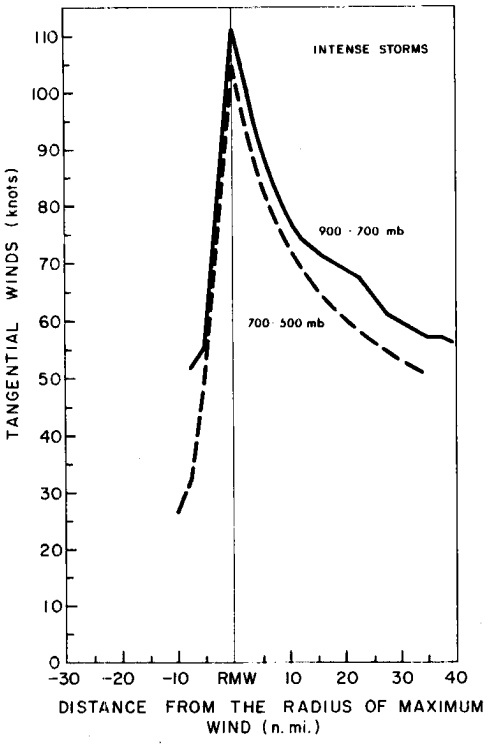

Fig. 70. Tangential wind profiles for intense storms (method I).

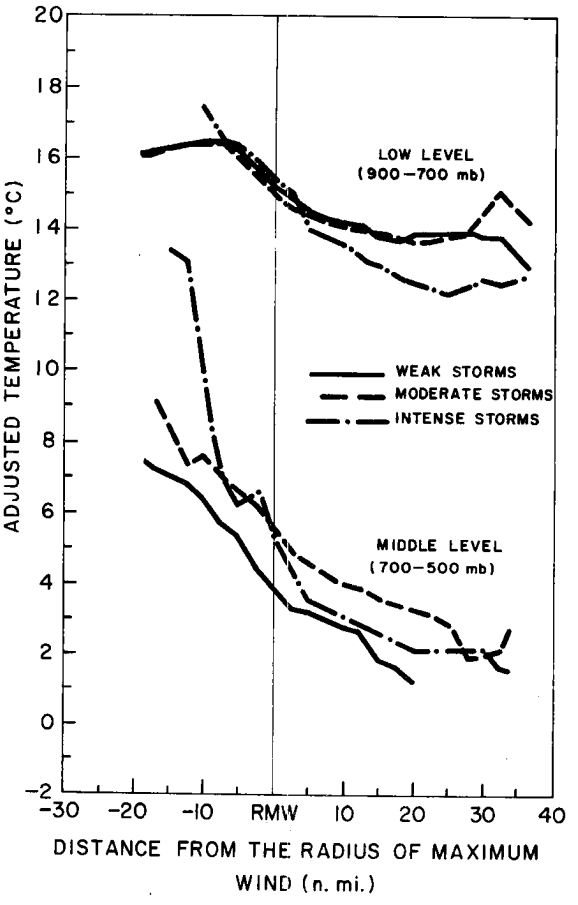

Fig. 71. Temperature profiles for weak, moderate and intense storms (method I).

profiles for the intense storms compared to the profiles for moderate and weak storms.

Temperature profiles for each storm classification are shown in Fig. 71. At lower levels the weak and moderate storms have similar temperature gradients. Intense storms appear to be cooler outside of the RMW and slightly warmer inside. At middle levels, a distinct difference between the three storm types is noted. The more intense the storm the higher are its temperatures and the larger are its temperature gradients.

Fig. 72 and 73 portray deviations of individual temperatures from the mean temperature at the RMW for the lower and middle levels. At the lower level, little temperature differences are noted inside the RMW. Outside the RMW the intense storms exhibited the largest deviations. At the middle level the deviations for the intense storms are significantly larger than for moderate and weak storms only at radii well inside the RMW. This is felt to be directly related to the strong inner eye wall subsidence associated with the more intense storms.

Storm Direction. In stratifying by direction, storms were classified as westerly moving (storm direction $\leq$ 315 degrees), northwesterly moving (315 $\leq$ storm direction $\leq$ 345 degrees) and north to northeasterly moving (storm direction $\leq$ 345 degrees). A cursory glance at Table 1 shows that this classification scheme has a definite

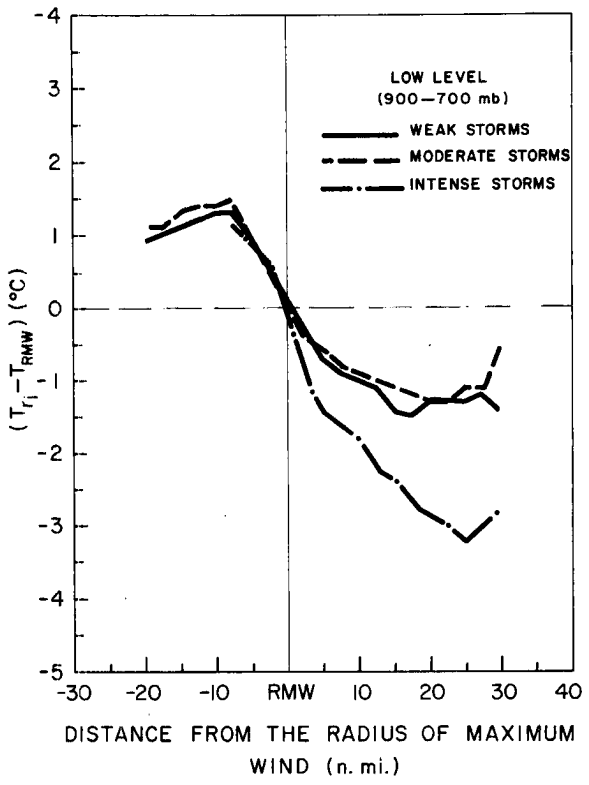

Fig. 72. Deviations of individual mean temperatures (T_{r_i}) from the mean temperature at the RMW in lower level (900-700 mb) for weak, moderate and intense storms.

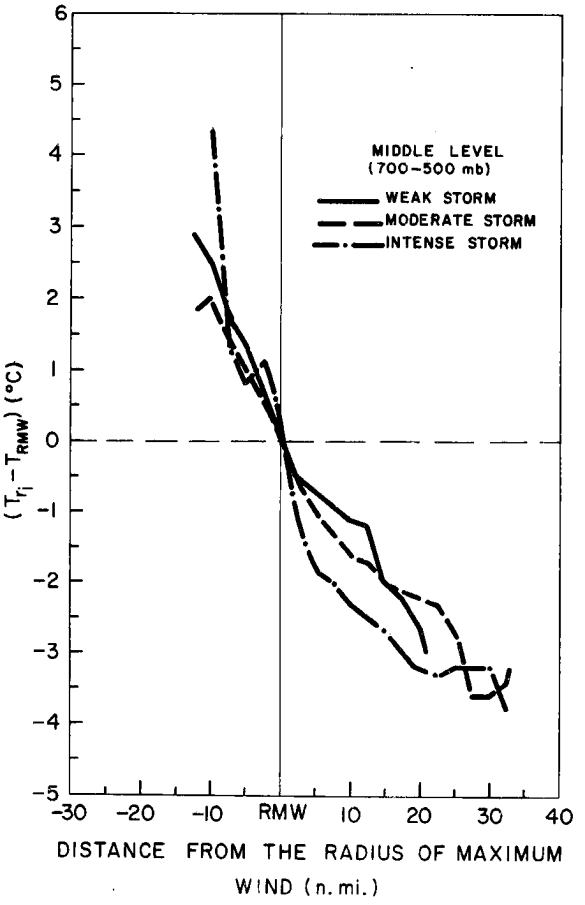

Fig. 73. Deviations of individual mean temperatures (T_{r_i}) from the mean temperature at the RMW in the middle level (700-500 mb) for weak, moderate and intense storms.

latitude bias. In general, westerly moving storms are at low latitudes, northwesterly are at middle latitudes, and north to northeasterly moving storms are at high latitudes. Thus, the results closely resemble those presented in a previous section on latitude stratification and will not be discussed here.

Storm Speed. Storms moving at different speeds were also examined. Fast moving storms were defined as those moving at speeds greater than 12 knots, slow storms were those moving less than 9 knots. Only the wind profiles are presented. These are shown in Figs. 74 and 75. Note that the faster moving storms exhibit stronger winds, smaller vertical shears and a slightly sharper maximum wind peak than do the slower moving storms.

Fig. 76 presents the variation of the RMW with latitude for lower tropospheric data. Although there is large variability at individual latitudes, there is a pronounced shift in tendency toward larger RMW's at high latitudes. Colón (1963) has noted that weakening storms are "invariably" accompanied by a widening of the eye. The present data agrees well with this conclusion.

In order to determine if a correlation exists between the RMW and the maximum winds, Figs. 77 and 78 were prepared. Again at both levels we note large variability. Nonetheless, a definite pattern exists with higher wind speeds occurring at radii closer to the storm center. In intense storms the low level inflow penetrates closer to the center. Angular momentum considerations would require higher wind speeds.

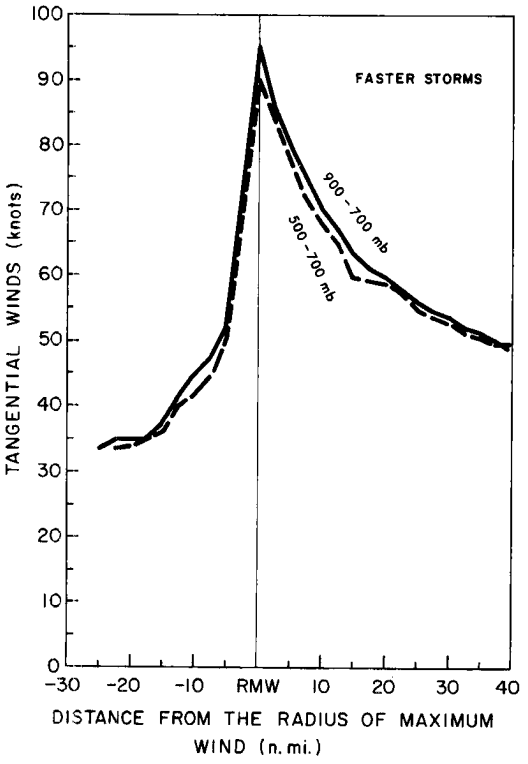

Fig. 74. Tangential wind profiles for faster storms (method I).

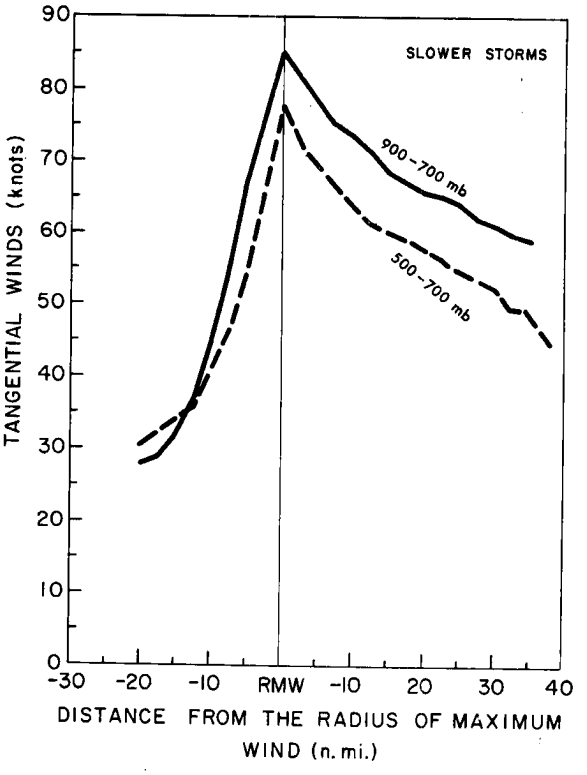

Fig. 75. Tangential wind profiles for slower storms (method I).

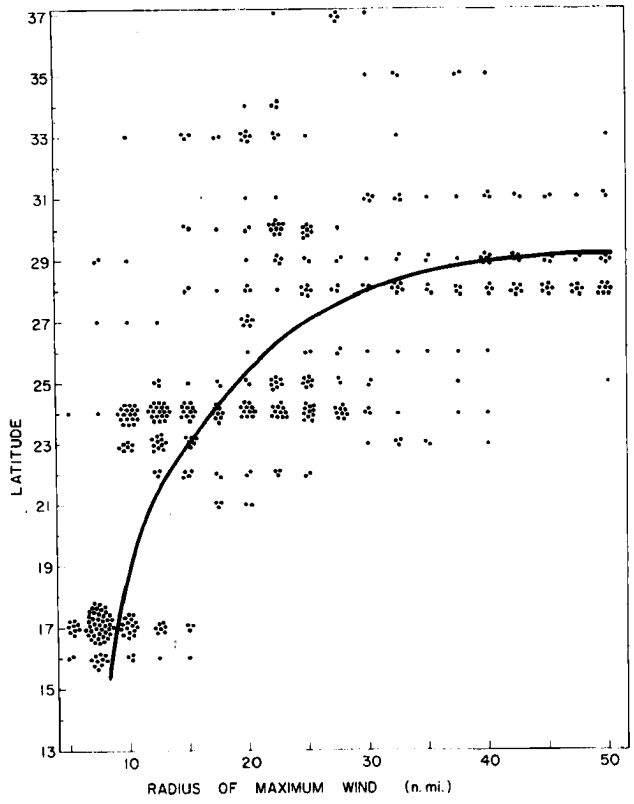

Fig. 76. Variation of the RMW with latitude for all lower tropospheric data. The best fit curve is indicated by the heavy line.

Fig. 79 shows the number of occurrences and frequency of the RMW's for all radial legs in the lower half of the troposphere. The mean maximum wind for each radii is shown at the top of each radii band. In most instances, the radius of maximum wind is inside 30 n. mi. As noted above, the highest wind speeds occur at radii close to the storm center.

Fig. 80 presents a scatter diagram of maximum wind speed versus central pressure. As expected in the statistical average surface pressure is inversely correlated with wind speed. There is, however, a large variability in maximum winds at various central pressures. Central pressure gives only a rough approximation to storm intensity.

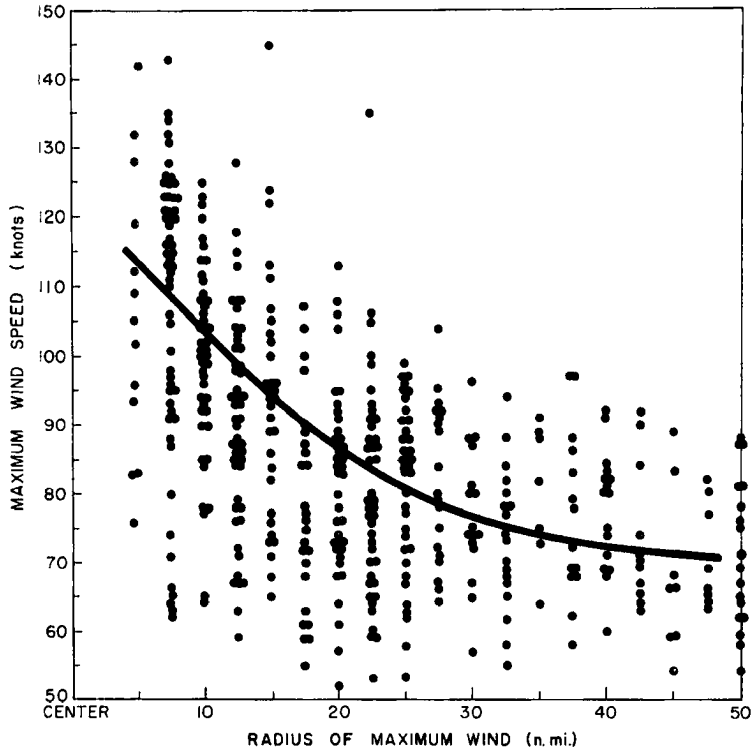

Fig. 77. Variation of the maximum wind with RMW for lower tropospheric data. The best fit curve is indicated by the heavy line.

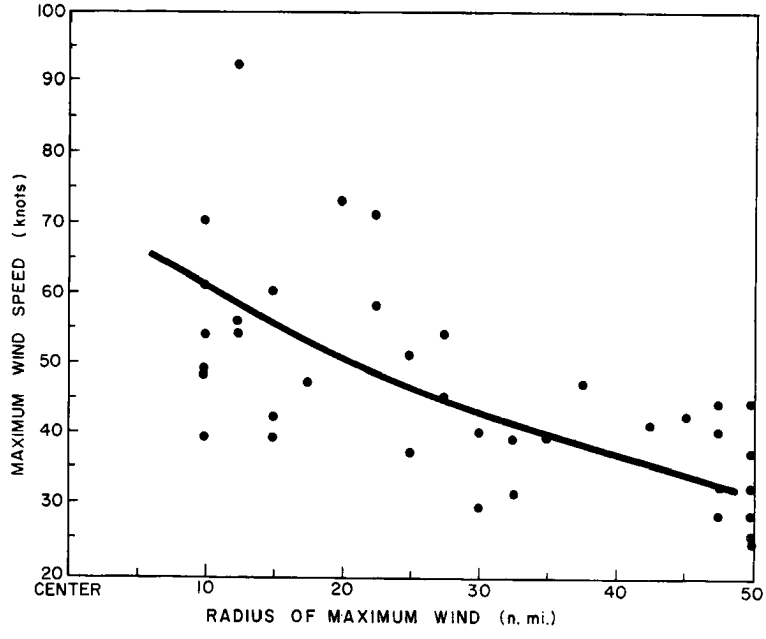

Fig. 78. Same as Fig. 73 except for upper tropospheric data.

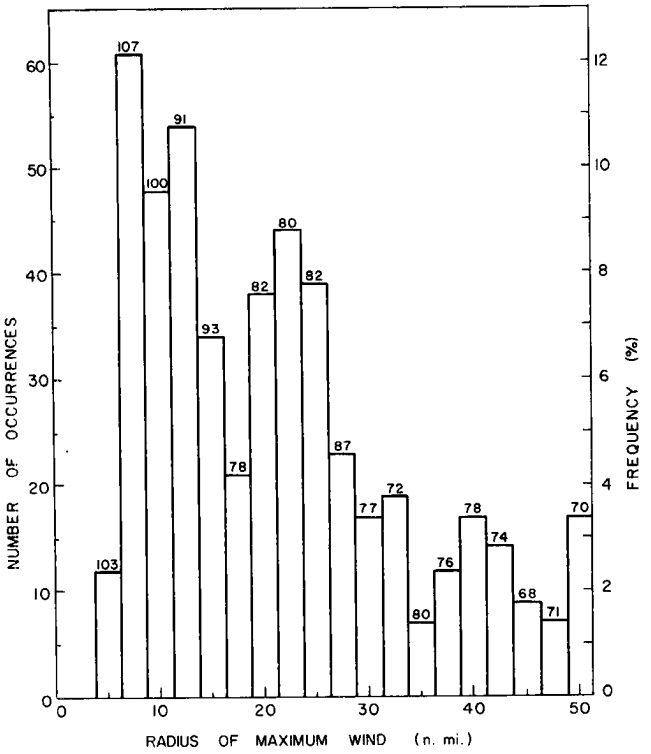

Fig. 79. Frequency distribution of the occurrence of the maximum wind at various radii. The mean maximum wind (in kts) at each radii is indicated at the top of each radii band.

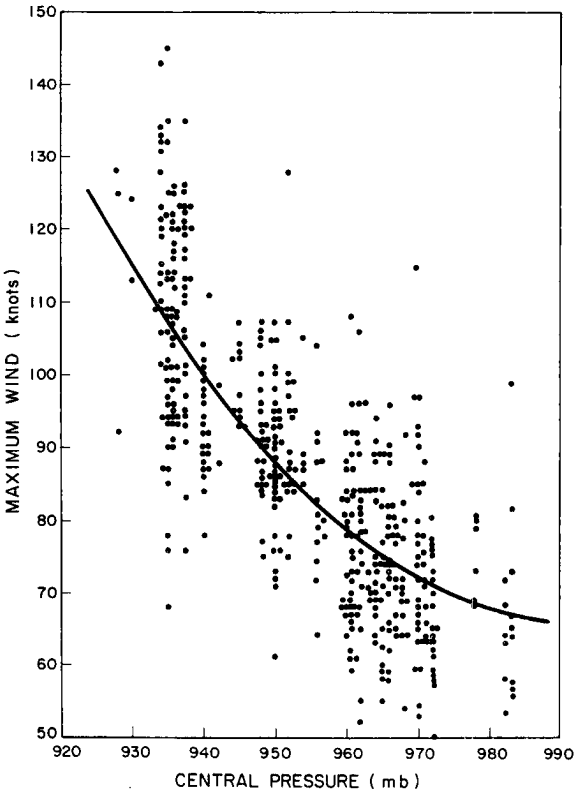

Fig. 80. Variation of the maximum wind with central pressure for all lower tropospheric data. The best fit curve is indicated by the heavy line.

VI. SUMMARY

The data when composited with respect to the radius of maximum winds holds together quite well. Although this compositing technique has shortcomings, it is felt that the characteristics which remain after averaging are the most significant and persistent features of the hurricane and merit close scrutiny.

Principal Results. A number of relevant features stand out:

i) The large variability of individual storms from the mean is the most striking general feature of this study.

ii) Maximum warming does not occur at the radius of maximum updraft. Thus the core heating cannot be thought of as resulting from direct sensible temperature diffusion from the updraft.

iii) Lapse conditions remain unstable in the inner core area. In cloudy areas a marked convective instability ($\partial \theta_e / \partial z < 0$) exists up to 750 to 700 mb. Areas where subsidence is present exhibit unstable conditions up to approximately 850 mb. Above this the moist instability is negative or much less than in the cloudy areas. Deepening storms show a deep unstable layer up to 625 mb, whereas, filling storms are unstable up to 800 mb.

iv) The discrepancy between the inner radar eye radius (IRR) and the radius of maximum wind (RMW) shows, rather dramatically, that the maximum winds occur within approximately 5-7 n. mi. of the cloud eye wall. In the most intense storms the difference between the IRR and the RMW is very small, whereas, in weak

storms the difference is large. Presumably this is due to the more concentrated and stronger subsidence which occurs in intense storms. This causes evaporation along the edge of the cloud eye wall.

v) The change of the RMW with elevation has been shown to be small and a function of storm intensity. Except for weak storms the RMW in the upper troposphere is almost directly above the RMW in the lower troposphere. In the lower half of the troposphere the RMW varies little with elevation, regardless of storm intensity. Physically, it is felt that the more intense convection in stronger storms is more effective in transporting the higher momentum at low levels to upper levels. This causes the cumuli to stand straighter and the maximum winds at upper levels to occur more directly above those at lower levels. This is not in good agreement with the hypothesis of Palmén (1956) who (from a physical argument based on thermal wind balance) hypothesized a significant slope to the eye wall clouds.

vi) The D-values of the mean symmetric storm exhibit a very symmetric pattern, whereas the wind field shows a larger degree of asymmetry. Analysis of the data used in this study shows that the winds to the right of the storm motion are generally super-gradient, whereas the winds to the left are sub-gradient. This agrees with earlier findings by Gray (1962) and LaSeur and Hawkins (1963). The advective terms of the total derivative account

for most of this difference between the right and left quadrant.

vii) Analysis of the frictionless, gradient wind equation shows that in the lower half of the troposphere the maximum winds at and just inside the RMW are super-gradient (even without a correction for water motion) by about 10 percent. With the Doppler correction for water motion the super-gradient character is increased even more.

viii) Vertical wind shears in the lower half of the troposphere are much less than the frictionless, thermal wind equation would indicate. In the region from the RMW outward to the RMW + 15 n. mi. the baroclinicity (B) is 40-60 percent larger than the inertial and wind shear term (W_rS) would indicate. In the upper half of the troposphere the W_rS term is 10-40 percent larger than the baroclinicity. This data verifies Gray's (1967) earlier finding concerning the unbalanced thermal wind in hurricanes. Deepening storms showed much larger thermal wind imbalance with small vertical shears. This may have an important operational potential.

ix) The largest convergence (20-25 x 10^{-5} sec^{-1}) and ascending vertical velocities ($\sim$ -50 x 10^2 mb/day) are concentrated in a narrow area centered at the RMW. Large divergence ($\sim$ 20 x 10^{-5} sec^{-1}) and subsidence is found approximately 6-7 n. mi. inside the RMW.

x) Tangential wind profiles in the lower half of the troposphere can, in the mean be approximated by equations of the form:

$$V_\theta r^{-1} = \text{constant (inside the RMW)}$$

$$V_\theta r^{0.5} = \text{constant (outside the RMW)}$$

The 0.5 exponent in the second equation coincides with that found by Riehl (1963). In the upper troposphere (240 mb) the magnitudes of the mean inner and outer exponents are larger than those at lower levels by approximately 50 percent.

xi) Composites of the tangential wind asymmetries in flight missions with approximately equally spaced radial legs verify that there is a natural asymmetry in hurricanes beyond that induced by motion as discussed by Sherman (1956). This amounts to roughly 15 to 25 percent of the wind speed.

VII. DISCUSSION

by William M. Gray

A number of unknown and heretofore undocumented features of the inner hurricane core have been revealed by the flight data. Some of the important physical characteristics can now be discussed.

Super-gradient Winds at Eye Wall. Figs. 35-39 clearly show the super-gradient nature of the winds at the RMW. These are present regardless of the magnitude of the Doppler wind correction for water motion. Maximum super-gradient winds are found at 900 mb just inside the RMW. These super-gradient winds must result from cross isobaric generation of the boundary layer inflow air exceeding the frictional dissipation. The inflow angle which allows for this cross isobaric generation can be further investigated from a Lagrangian frame of reference applied to the inflowing boundary layer particles.

The acceleration acting on an inflowing particle in the boundary layer is given by

$$\frac{dV}{dt} = -\frac{1}{\rho}\frac{\partial p}{\partial s} - F_s \qquad (1)$$

where V = velocity of an air particle

s = direction tangential to the particle motion

F_s = frictional acceleration acting on the particle equal to

$$\frac{-1}{\rho}\frac{\partial T_{szo}}{\partial z} = \frac{-C_D V^2}{\Delta z}$$

where T_{sz_o} (surface stress) = $C_D \rho V^2$, C_D is the surface drag coefficient, and Δz is the depth of the mechanical boundary layer over which the stress acts. The $(-\frac{1}{\rho} \frac{\partial p}{\partial s})$ term represents the acceleration by the pressure gradient acting along the direction of flow and F_s represents the deceleration by the retarding frictional acceleration. For the inflowing particle to increase its velocity $-\frac{1}{\rho} \frac{\partial p}{\partial s}$ must be larger than F_s.

As the storm's wind velocities increase towards the center (i.e., $V \frac{\partial V}{\partial s}$ is positive) super-gradient flow requires that the inflowing winds increase their velocity at a rate not only larger than that prescribed by wind-pressure balance but also at a rate larger than the advective increase (i.e., $V_g \frac{\partial V_g}{\partial s}$) where V_g is the gradient wind speed. Super-gradient winds thus require a positive value of $\frac{\partial V}{\partial t}$ where

$$\frac{\partial V}{\partial t} = \frac{1}{\rho} \frac{\partial p}{\partial s} - F_s - V_g \frac{\partial V_g}{\partial s} \qquad (2)$$

This equation can be examined in terms of the boundary inflow angle (α) defined as $\alpha = -\arcsin \frac{V_r}{V}$ where V_r is the radial wind velocity (positive outward).

Assuming a symmetric vortex and that the pressure gradient can be approximated by cyclostrophic balance $(\frac{V_g^2}{r} + fV_g)$ then $\frac{-1}{\rho} \frac{\partial p}{\partial s} \approx \sin \alpha \frac{\partial p}{\partial r} \approx \sin \alpha \left(\frac{V_g^2}{r} + fV_g \right)$. In a similar manner

$$-V_g \frac{\partial V_g}{\partial s} \approx \sin \alpha \; V_g \frac{\partial V_g}{\partial r}$$

Equation (2) can now be written as,

$$\frac{\partial V}{\partial t} \left(\begin{array}{l} \text{required positive for super-} \\ \text{gradient winds} \end{array} \right) = \sin \alpha \left(\frac{V_g^2}{r} + fV_g - V_g \frac{\partial V_g}{\partial r} \right) - F_s \qquad (3)$$

Using the flight data it is possible to solve for the required inflow angle, α, such that the right hand side of (3) be positive. Taking a value (Fig. 81) of C_D of $\sim 3.0 \times 10^{-3}$ following the estimates of Miller (1962 1963) and Palmen and Riehl (1957) and assuming that two-thirds of the surface vertical stress gradient takes place over the sub-cloud layer (or lowest half km), the required inward crossing angle (α) for super-gradient winds can be estimated. Fig. 82 is a radial plot for the mean storm of the sub-cloud layer wind-pressure crossing angle (or inflow angle for a symmetrical pressure gradient) such that the low level air will accelerate at a rate greater than that required by gradient wind balance. These inflow angles are small at the inner radii, but are unrealistically high at larger radii (> 50 n. mi.).

Super-gradient winds are possible at the inner radii by virtue of the decreasing radius and very large pressure gradients which are required at inner radii where $\frac{1}{\rho} \frac{\partial p}{\partial r} \sim \frac{V^2}{r}$. F_s on the other hand, is not dependent on radius and is proportional only to $\frac{C_D}{\Delta z} V^2$. The ratio of $\frac{1}{\rho} \frac{\partial p}{\partial r} \; / \; F_s$ is thus $\frac{\Delta z}{C_D} \frac{1}{r}$. If $\frac{\Delta z}{C_D}$ does not vary

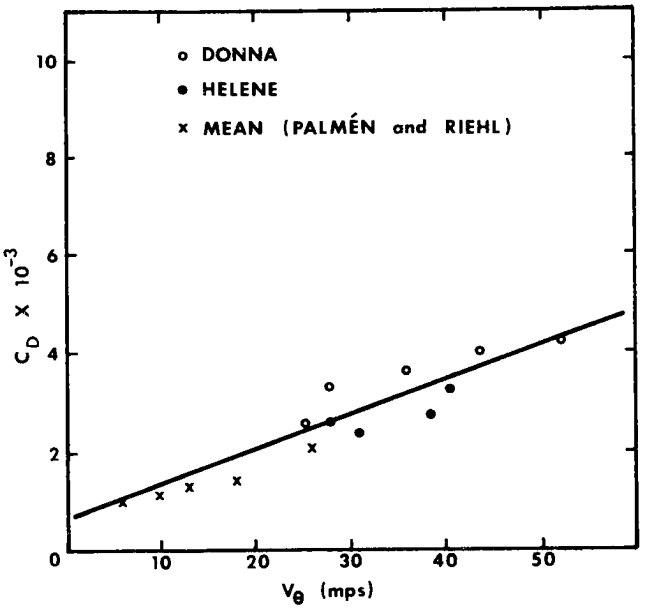

Fig. 81. Drag coefficient as a function of wind speed (Miller, 1963).

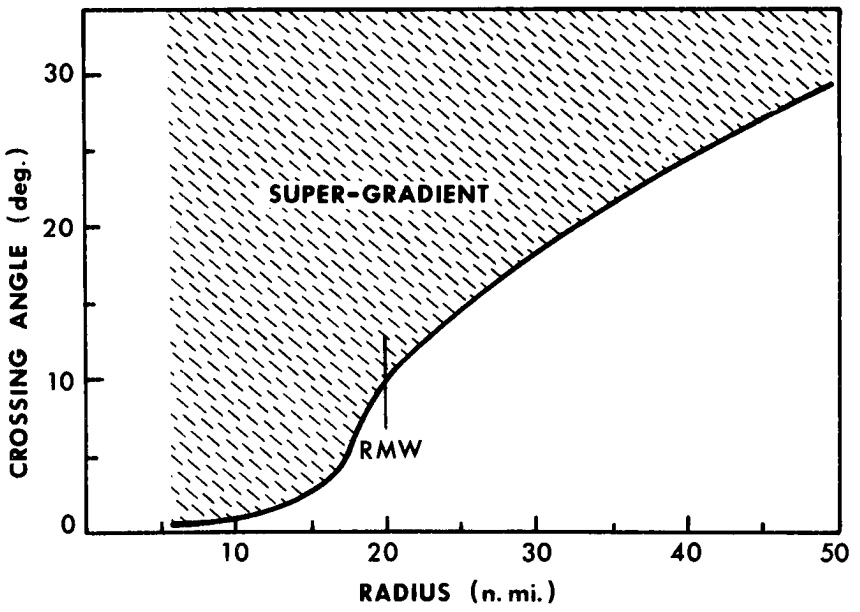

Fig. 82. Boundary layer inflow angle vs. radius which is required for super-gradient flow.

very much with radius then it is readily seen that the ratio of the pressure gradient to frictional acceleration becomes excessively large at inner radii. Inflowing air can thus receive much larger acceleration at inner radii than that which would be possible further out. Thus, super-gradient winds are both observed and possible only at small (less than 20-30 n. mi.) radii. As will be discussed later and as was earlier anticipated by Malkus (1958) eye wall formation is dependent on super-gradient winds. It is an observed fact that hurricane eye formation is typically restricted to radii inside of 20-30 n. mi. radius where super-gradient flow is possible. The importance of the magnitude of the inflow angle for hurricane intensity has been previously discussed by Malkus and Riehl (1960).

Role of Super-Gradient Winds. The primary purpose of the super-gradient winds is to act as a brake on the frictionally forced boundary layer convergence. The concentration of eye wall convection and other model work (Gray, 1967) shows that the boundary layer air penetrates to small radii and then suddenly slows down and releases itself in eye wall convection. The radius of sharp decrease of inward radial flow corresponds well with the radius of super-gradient flow. The rapid acceleration of the inflowing winds to super-gradient velocities at the inner radii produces a sudden outward acceleration which balances the inward acceleration of the surface friction. No further inflow is possible. The eye size is determined by the radius at which this balance is obtained.

These "overshot" air particles are now advected in the cumulus to higher levels where (due to decreasing wind with height) a smaller but still positive super-gradient wind is maintained (Figs. 36-38). It is especially at the RMW in the right quadrant that super-gradient winds are very large. Here the actual wind may exceed the gradient wind by perhaps 40-50 percent.

By similar reasoning, one might also hypothesize that tornado vorticies may have strong super-gradient winds at their RMW.

Eye-Region Ventilation. The very strong horizontal wind shears at the boundary of the eye and eye wall region induce a high degree of turbulent mixing and horizontal momentum transfer into the eye. The winds on the edge of the eye must thus become super-gradient and be accelerated outward into the wall cloud. This outward directed air from the eye requires a compensating mass replacement from higher levels into the eye. The outward measured mean radial winds just inside the RMW at all lower tropospheric levels (averaging about ~ 1 m/sec - See Figs. 9-12) verify this eye area sinking and outward directed eye mass transport. This was anticipated by Malkus (1958).

The measured mean eye divergence below 525 mb (i.e., divergence in the area with radii less than RMW - 5 n.mi.) shows an average value of $\sim 4\text{-}5 \times 10^{-5} \text{sec}^{-1}$ or total eye mass replace in about 5-6 hours. The eye will typically move the distance of its diameter in about two to three hours. This means, that on the average, only about a half of the eye mass remains within the center of the moving storm after it

moves the distance equivalent to its eye diameter. The eye is continually ventilated and reforming itself by new sinking and warming as it moves. Fast moving and intense storms with small eye diameters will ventilate their eye at a much more rapid rate, some in less than an hour. Slower moving and weaker storms with wide eye diameters have very slow eye ventilation rates. A flight into a near stationery storm (Hurricane Gladys 20 September, 1964 - central pressure 960 mb) showed no eye wall convection. The warm cyclone center air was stagnate. Without storm motion there was no need to cycle air through the storm's center. By comparison, the radiation and purely turbulent diffussion heat losses were small.

These observations do not support the "stagnate eye" hypothesis where the eye particles move with the storm for long periods without mixing. The central region of the moving hurricane with eye wall convection may thus be thought of as a "driven" and "mixed" inner core area with considerable eye and eye wall cloud exchange. The magnitude of the mixing induced eye outflow at low levels determines the eye intensity by regulating the amount of upper level air from the cumulus which will have to flow back into the eye and not be caught up in the upper tropospheric outflow.

Eye Compressional Heating and Evaporation for Mean Storm.

Averaging the sinking air motion of Fig. 46 over the whole inner eye region (i.e., radii inside of RMW - 5 n. mi.) one obtains a mean 525 mb to surface average compressional warming of about 3°C per hour. For steady conditions this must be mostly balanced by evaporation from inward turbulent mixing of cloud liquid water from the eye wall. Averaging over the eye area this evaporation amounts to about 0.6 gm/cm^2 per hour. At the places of maximum downward motion near the cloud edge, this evaporation may average over 2-3 gm/cm^2 per hour. For stronger and faster moving or weaker and slower moving storms, these values will be correspondingly larger or smaller. With the eye measured temperatures and the calculated sinking motion shown in Fig. 46, the following mean eye area relative humidities will permit an evaporation rate such that the compressional heating is nearly balanced (with small one hour eye ventilation effects subtracted out) and an eye averaged steady state can be maintained.

Pressure (mb)	Temperature (°C)	Relative Humidity (%)
525	2	50
630	9	60
750	14	75
900	21	90

These are about the relative humidity values expected in the eye as reported by Jordan (1958b, 1961) from eye dropsonde data.

Potential Buoyancy of the Cloud Wall Convection. Some researchers feel that within the area of eye wall convection the relative humidities are nearly 100 percent, that small θ_e vertical gradient exists, and that there is thus little potential moist buoyancy. The cumulus convection would then be primarily a result of the low level frictionally forced convergence with little or neutral moist buoyancy.

Observing the intensity of the individual eye wall cumulonimbus this assessment does not seem physically valid. At the radius of maximum convection, the percentage area covered by active up-drafts may only be about 10-20 percent. With the sinking motion around the cumulus and the outward advection of dryer air from the eye, it is likely that the relative humidity at this radius (averaged around the storm) is considerably less than 100%. The observations of vertical temperature gradient with various assumed relative humidities (as reported in the previous section) support substantial potential moist buoyancy (i.e., $\frac{\partial \theta_e}{\partial z} < 0$) up to 600-700 mb at the radius of maximum convection at the RMW. Only filling storms (Fig. 64) had small or positive change of θ_e with height starting as low as 800 mb. One has to go into the upper troposphere to find θ_e values as high as the values which would exist at the surface with air temperatures of 25-26°C and relative humidity of 90 percent - See Fig. 48.

Implication for Inner-Core Warming Mechanism. Figs. 51 and 52 clearly portray the correspondence of the RMW with both the radius of

maximum vertical motion and the radius of maximum horizontal temperature gradient, not maximum temperature. The positive temperature departure from surroundings at the radius of maximum vertical motion is only half the magnitude of the positive temperature departure inside the eye. One cannot explain the inner eye warming from direct diffusion of sensible temperature from the cumulus, or Cb, updraft. This warming, of necessity, must come from the sinking motion inside the radius of cumulus activity. The downward motion shown in Fig. 46 just inside the eye wall will support a large compressional warming. This heating is spread by turbulence outward from the eye into the cloud area.

Most of the air for the sinking in the center comes from the eye wall cloud air which rises and is not advected away in the upper level outflow but drifts further inward and sinks inside the eye wall cloud. This produces the eye wall warming and the inner temperature rises.

The latent heat released from the cumulonimbus, or cumulus, goes primarily into potential energy gain and increasing the temperature of the rising parcel to that of the environmental temperature. The small extra, above environment, temperature increase of 1^{o} to 2^{o} of the rising parcel, which is required for buoyancy, does not warm the environment unless it directly mixes out from the cloud at a higher temperature. The rising parcel typically continues rising until it loses its buoyancy and temperature excess. It then mixes to the environment at

a temperature little different than that of the environment. This does not warm the environment. Any diffusional or advective heat transports out from the rising, and warmer, cloud parcel are more than overcome by the evaporation of the residual cloud liquid water particles around the cumulus or in downdrafts. Individual hurricane cumulonimbus last only about 30-35 minutes. Any residual liquid particles which remain after the vertical motion in the cumulus has stopped cool the environment in and around the dying cloud at a rate of 2.4°C for every gm/Kg evaporated. Thus, the cumulus or Cb cloud directly cools the environment around which it exists.

Being an open system, the typical cumulonimbus converts nearly all its condensation heat to potential energy and exports this to the immediate surroundings. Even though heavy rainfall may have occurred, there is typically no immediate warming at the place and time of the precipitation. Usually there is a slight cooling. This is not to say that the total effect of the condensation to the more "closed system" of the entire hurricane environment has not been one of warming. It has. The dry adiabatic sinking within the eye or at larger radius more than compensates for the local evaporation cooling around the clouds. In this way the cumulus acts in a delayed action sense. The sometimes envisaged cumulus warming mechanism of heat mixing to the environment from a slightly warmer updraft is not the warming mechanism operating in the inner hurricane area. The positive temperature

anomalies at the radius of maximum convection results from warm advective and turbulent mixing outward from the eye.

Eye - Eye Wall Cloud Transfers. Fig. 83 shows the direction of the advective and turbulent radial exchanges of mass, momentum, enthalpy and moisture transfers between eye and eye wall region which must take place in the lower half of the troposphere to maintain the inner hurricane circulation. The advective and turbulent momentum transfers go opposite to each other as do also the liquid water and vapor transfers.

Summary. The eye and eye wall convective region appears to be a dynamically forced circulation which is dependent on the surrounding broader scale flow. The changing character of the eye and eye wall circulation over periods of but a few hours imply a response to an outside forcing mechanism and not vice versa. Eyes do not form in just "any old kind of surrounding flow". The crucial physical feature to be understood appears to be the character of the accelerating inflowing boundary layer wind. Why will the inflowing air penetrate to radii of 5 to 10 n. mi. in some cases, and in other situations to radii of but 20 to 30 n. mi. ? What establishes the various magnitudes of low level wind-pressure crossing angle? These appear to be the crucial parameters in specifying inner-core storm differences. The author surmises that these differences should be related to the surrounding broader scale flow patterns. If this proves to be the case, then it may

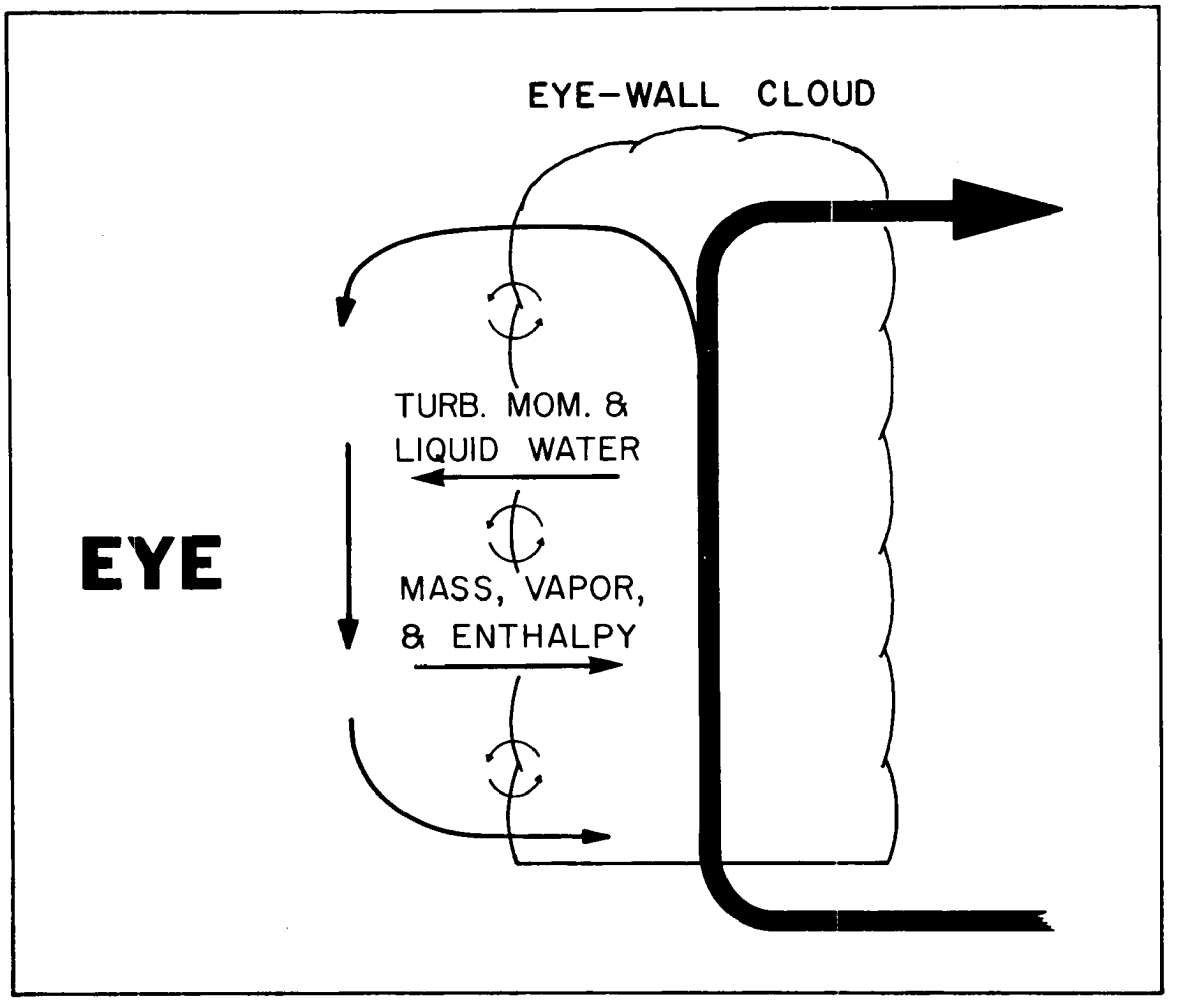

Fig. 83. Direction of the turbulent transfer of mass, momentum, enthalpy, water vapor and liquid water between the eye and eye wall cloud area.

be possible to develop a degree of short term eye intensity forecasting skill.

Future Research. There are many more radial legs to be looked at as the data processing proceeds. It is hoped that some data compositing can be accomplished with the moisture values and with the character of the individual radar eye cloud fluctuations. In addition, the structural and dynamic differences of the individual storm from the mean storm have to be more explicitly described.

BIBLIOGRAPHY

Black, P.G., J.J. O'Brien and B.M. Lewis (1967): Ocean motion beneath a hurricane and its influence on the operation of Airborne Doppler Radar. 40 pp. (unpublished manuscript).

_____, and R.A. Anthes (1971): On the asymmetric structure of the tropical cyclone outflow layer. J. Atm. Sci. 28, 1348-1366.

Colón, J.A. (1963): On the evolution of the wind field during the life cycle of tropical cyclones. National Hurricane Res. Proj. Rept. No. 65, 36 pp. (available from NOAA Weather Bureau, Miami office).

_____, (1964): On the structure of hurricane Helene (1958). National Hurricane Res. Proj. Rept. No. 72, 56 pp. (available from NOAA Weather Bureau, Miami office).

_____, and Staff, NHRP (1961): On the structure of hurricane Daisy (1958). National Hurricane Res. Proj. No. 48, 102 pp. (available from NOAA Weather Bureau, Miami office).

Friedman, H.A., F.S. Cicirelli and W.J. Freedman (1969): The ESSA Research Fligh Facility: Facilities for airborne atmospheric research. ESSA Technical Report ERL 126-RFF1 89 pp.

Gentry, R.C. (1964): A study of hurricane rainbands. National Hurricane Res. Proj. Rept. No. 69, 85 pp. (available from NOAA Weather Bureau, Miami office).

Gray, W.M. (1962): On the balance of forces and radial accelerations in hurricanes. QJRMS 88, 430-458.

_____, (1965a): Calculations of cumulus vertical draft velocities in hurricanes from aircraft observations. J. App. Meteor. 4, 463-474.

_____, (1965b): On the scales of motion and internal stress characteristics of the hurricane. National Hurricane Res. Lab. Rept. No. 73, 121 pp. (available from NOAA Weather Bureau, Miami office).

_____, (1966): On the scales of motion and internal stress characteristics of the hurricane. J. Atm. Sci. 23, 278-288.

Gray, W.M. (1967): The mutual variation of wind, shear and baroclinicity in the cumulus convective atmosphere of the hurricane. Mon. Wea. Rev. 95, 55-73.

Grocott, D.F. (1963): Doppler correction for surface movement. J. of Instrument Navigation. 16: 57-63.

Hawkins, H.F. (1962): Vertical wind profiles in hurricanes. National Hurricane Res. Proj. Rept. No. 55, 16 pp. (available from NOAA Weather Bureau, Miami office).

_____, F.E. Christensen, S.C. Pearce, and Staff NHRP (1962): Inventory, use and availability of National Hurricane Research Project data gathered by aircraft. National Hurricane Res. Proj. Rept. No. 52, 24 pp. (available from NOAA Weather Bureau, Miami office).

_____, and D.T. Rubsam (1968a): Hurricane Hilda, 1964. I. Genesis, as revealed by satellite photographs, conventional and aircraft data. Mon. Wea. Rev. 96, 428-452.

_____, (1968b): Hurricane Hilda, 1964. II. Structure and budgets of the hurricane on October 1, 1964. Mon. Wea. Rev. 96, 617-636.

_____, (1968c): Hurricane Hilda, 1964. III. Degradation of the hurricane. Mon. Wea. Rev. 96, 701-707.

Hilleary, D.T., and F.E. Christensen, (1957): Instrumentation of the National Hurricane Research Project Aircraft. National Hurricane Res. Proj. Rept. No. 11, 61 pp. (available from NOAA Weather Bureau, Miami office).

Hughes, L.A. (1952): On the low level wind structure of tropical cyclones, J. Meteor. 9, 422-428.

Izawa, T. (1964): On the mean wind structure of typhoons. Japan Typhoon Research Laboratory. Tech. Note. No. 2, 45 pp.

Jordan, C.L. (1957): Mean soundings for the hurricane eye. National Hurricane Res. Proj. Rept. No. 13, 10 pp. (available from NOAA Weather Bureau, Miami office).

_____, (1958a): Mean soundings for the West Indies area. J. Meteor. 15, 91-97.

Jordan, C.L. (1958b): Vertical profiles of wind velocity in tropical cyclones. In AMS Technical Conference on Hurricanes, Miami, Fla., Nov. 1958. pp. E2-1 to E2-6.

_____, (1961): Marked changes in the characteristics of the eye of intense typhoons between the deepening and filling stages. J. Meteor. 18: 779-789.

_____, D.A. Hurt, and C.A. Lowry (1960): On the structure of hurricane Daisy of 27 August 1958. J. Meteor. 17: 337-348

LaSeur, N.E., and H.F. Hawkins (1963): An analysis of hurricane Cleo (1958) based on data from research reconnaissance aircraft. Mon. Wea. Rev. 91, 694-709.

Malkus, J.S. (1958): On the structure and maintence of the mature hurricane eye. J. Meteor. 15, 337-349.

_____, and H. Riehl (1960): On the dynamics and energy transformations in steady-state hurricanes. Tellus 12, 1-20.

Miller, B.I. (1958): The three dimensional wind structure around a tropical cyclone. National Hurricane Res. Proj. Rept. 15, 41 pp. (available from NOAA Weather Bureau, Miami office).

_____, (1962): On the momentum and energy balance of hurricane Helene (1958). National Hurricane Res. Proj. Rept. No. 53, 19 pp. (available from NOAA Weather Bureau, Miami office).

_____, (1963): On the filling of tropical cyclones over land. National Hurricane Res. Proj. Rept. No. 66, 82 pp. (available from NOAA Weather Bureau, Miami office).

Palmén, E. (1956): Formation and development of tropical cyclones. In "Proceedings of Tropical Cyclone Symposium, Brisbane", pp. 213-231. Australian Bur. Meteorol., Melbourne.

_____, and H. Riehl (1957): Budget of angular momentum and energy in tropical cyclones. J. Meteor. 14, 150-159.

Reber, C. and H. Friedman, (1964): Manual of meteorological instrumentation and data processing of the research flight facility. U.S. Weather Bureau (available from Miami, Fla.).

Riehl, H. (1954): Tropical Meteorology, Chapter 11. McGraw-Hill New York.

Riehl, H. (1961): On the mechanisms of angular momentum transports in hurricanes. J. Meteor. 18, 113-115.

_____, (1963): Some relations between wind and thermal structure of steady-state hurricanes. J. Atm. Sci. 20, 276-287.

_____, and J.S. Malkus (1961): Some aspects of hurricane Daisy, 1958. Tellus, 13, 181-213.

Sheets, R.C. (1967a): On the structure of hurricane Janice (1958). National Hurricane Res. Lab. Rept. No. 76, 38 pp. (available from NOAA Weather Bureau, Miami office).

_____, (1967b): On the structure of hurricane Ella (1962). National Hurricane Res. Lab. Rept. No. 77, 33 pp. (available from NOAA Weather Bureau, Miami office).

_____, (1968): On the structure of hurricane Dora (1964). National Hurricane Res. Lab. Rept. No. 83, 64 pp. (available from NOAA Weather Bureau, Miami office).

_____, (1969): Some mean hurricane soundings. J. App. Metero. 8: 134-146.

Sherman, L. (1956): On the wind asymmetry of hurricanes. J. Meteor. 500-503.

Simpson, R.H. (1952): Exploring the eye of typhoon Marge 1, 1951. BAMS. 27: 324-327.

_____, and L.G. Starrett (1955): Further studies of hurricane structure by aircraft reconnaissance. BAMS. 36: 459-468.

Staff, Natl. Hurricane Res. Proj. (1958): Details of circulation in the high energy core of hurricane Carrie. National Hurricane Res. Proj. Rept. No. 24, 15 pp. (available from NOAA Weather Bureau, Miami office).

Wexler, H. (1945): The structure of the September, 1944 hurricane when off Cape Henry, Virginia. BAMS. 26: 156-159.

ACKNOWLEDGEMENTS

The author wishes to express his gratitude to Professor William M. Gray who proposed this research topic and whose guidance and encouragement made this study possible. Special thanks are to be given to Miss Peggy Hermann, Mrs. Barbara Brumit and Mr. Larry Kovacic who offered considerable assistance in the data reduction, analysis and in the manuscript typing and drafting.

APPENDIX I

Sample Radial Leg Data

Fig. A1 shows a sample radial leg data printout. The code explanations are:

STORM - name of the storm

DATE - date on which the data was obtained (yr./mo./day)

ZLVL - plane's pressure altitude (feet)

PLVL - plane's pressure altitude (mb)

TIME INTERVAL - time interval over which the data was taken in GMT

I-O - denotes whether the plane was flying in (I) toward the center or out (O) from the center of the storm

LAT - LONG - latitude and longitude of the storm

DIR - storm direction in degrees

SPD - storm speed (knots)

TH - plane's true heading (approximate) in degrees

QN - octant of the storm in which the plane was flying w.r.t. geographic north

QSTM - octant of the storm in which the plane was flying w.r.t. storm motion. 1-plane is in front octant; 3-plane is in the octant which is at a right angle to storm motion etc., (See Fig. A2)

STORM	DATE	ZLVL	PLVL	TIME INTERVAL	I-O	LAT	LONG	STORM DIR	STORM SPD	TH	QN	QSTM	ARL	ID	RDR EYE RADIUS	CENT. PRES	VATX	RMW	VRTX
INEZ	660928	8090	763	2216-2235	I	17	66	275	12	350	S	7	170	214	7	928	144	7.5	131

RADIUS	VAT	VAR	VRT	VRR	D-VALUES	TADJ
5.0	116	-6	104	-6	-1790	16.0
7.5	144	-3	131	-4	-1330	15.7
10.0	124	-4	111	-6	-900	14.2
12.5	107	-8	94	-10	-670	13.4
15.0	105	1	92	-1	-490	13.0
17.5	92	2	79	-1	-370	12.8
20.0	83	3	70	0	-300	12.7
22.5	84	5	71	2	-210	12.7
25.0	79	0	66	-3	-150	12.6
27.5	75	1	63	-2	-110	12.2
30.0	68	-1	55	-4	-70	11.7
32.5	67	5	53	2	-20	11.8
35.0	58	-1	45	-3	-10	11.5
37.5	62	0	49	-3	40	11.7
40.0	62	1	49	-2	40	11.7
42.5	65	4	52	1	90	11.9
45.0	58	6	45	3	100	11.8
47.5	55	10	42	7	130	11.6
50.0	56	14	43	10	140	11.5

Fig. A1. Sample data printout for an individual radial leg.

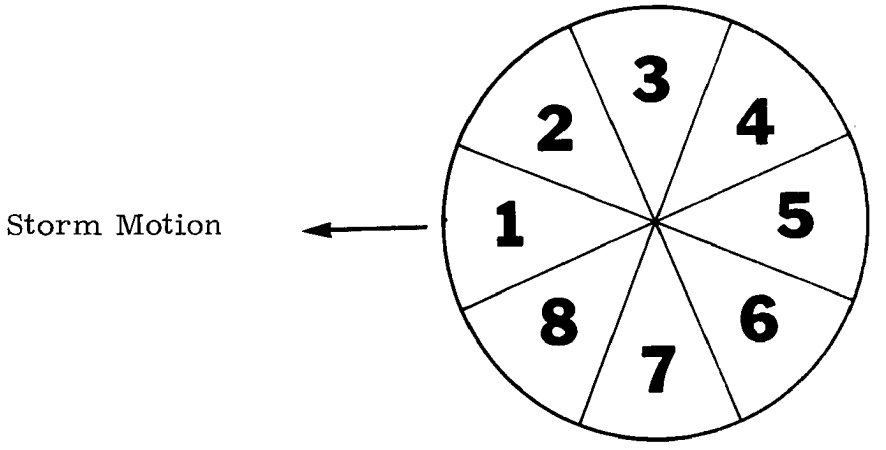

Fig. A2. Code numbers which indicate the octant which the plane was flying. The arrow indicates storm motion.

ARL - azimuth angle of the radial leg (approximate) relative to the direction true north

ID - arbitrary identification number assigned to each radial leg

RDR EYE RADIUS - inner radar eye radius (n. mi.); the letter following the number indicate whether the radar eye radius is approximate (A), well defined (WD), poorly defined (P)

CENT PRES - storm's approximate central pressure (mb)

VATX - maximum actual tangential wind

VRTX - maximum relative tangential wind

RMW - radius at which the maximum winds occur

RADIUS - distance from storm center (n. mi.)

VAT - actual tangential velocity (kts)

VAR - actual radial velocity (kts)

VRT - relative tangential velocity (kts)

VRR - relative radial velocity (kts)

D-VALUES - D-values (feet)

TADJ - adjusted temperature (no virtual temperature correction)

APPENDIX II

The temperature and D-value data used in this report are considered to be quite reliable— in the statistical average. In order to check this assertion, area weighted radial vortex temperature gradients were compared with temperature gradients calculated from flight D-value thickness gradients through use of the hydrostatic equation, thus

$$\Delta T_{cal} = \int_{\text{RMW-10 n. mi.}}^{\text{RMW + 30 n. mi.}} \frac{\partial T}{\partial r}\, dr = \frac{g}{R} \ln \frac{P_1}{P_2}\, \Delta D_{obs}$$

and

$$\Delta T_{obs} = [\, \Delta T_{upper} + \Delta T_{lower} \,] / 2$$

where ΔT_{cal} is the calculated radial temperature gradient

ΔD_{obs} is the observed radial thickness gradient between levels 1 and 2

P_1, P_2 is the upper and lower pressure levels

g is the acceleration of gravity

R is the gas constant

ΔT_{obs} is the mean observed radial temperature gradient

ΔT_{upper} is the observed radial temperature gradient in the upper pressure level

ΔT_{lower} is the observed radial temperature gradient in the lower pressure level

The calculations were performed on all the double level flights which

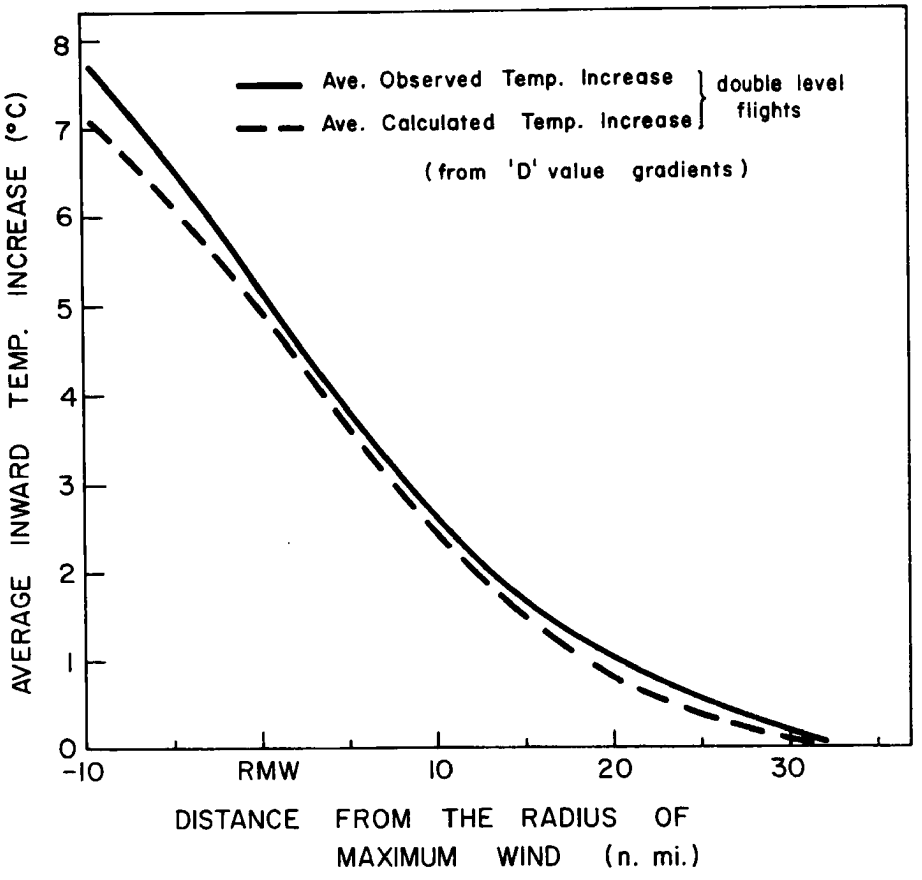

Fig. A3. Composited observed and calculated temperature gradients. Temperature increases were measured from 30 n. mi. outside the RMW to 10 n. mi. inside the RMW (method I).

occurred exclusively in the lower half of the troposphere. The composited (method I) results are shown in Fig. A3. It is obvious that, in the mean, the calculated and observed radial temperature gradients are quite close.

APPENDIX III

IN-OUT Stratification

A few researchers (e.g., Colón, 1964) have asked how individual parameters (temperature, D-values, radial winds) might vary as data is gathered by inward (IN) plane penetration as opposed to outward (OUT) plane penetration of the inner core area. In order to investigate this, each radial leg was classified as to whether the plane was flying IN or OUT. Figs. A4, A5 and A6 show the results for the temperatures, D-values and radial winds respectfully. In the statistical average no systematic differences are noted in any of the parameter profiles. The temperature and D-value gradients for the IN and OUT legs are remarkably similar. The radial wind profiles differ but not in any consistent fashion.

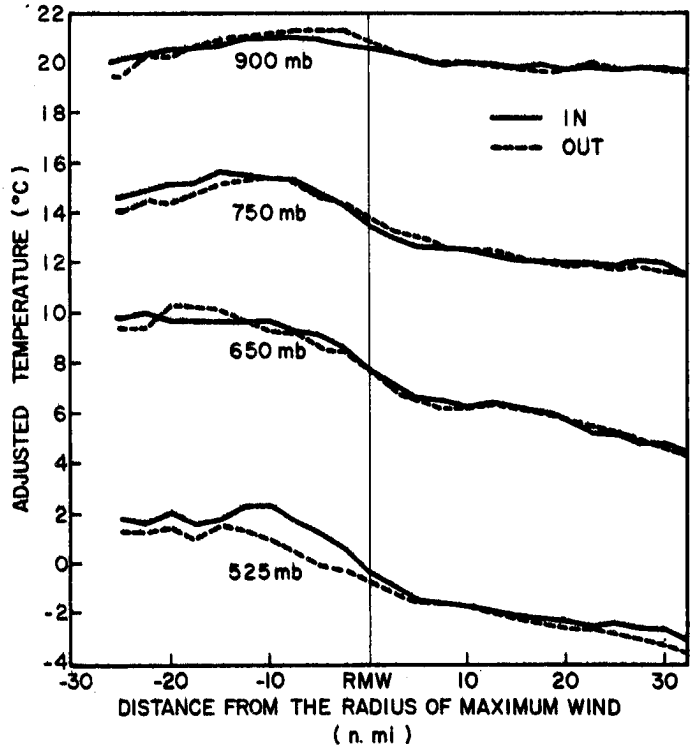

Fig. A4. Composited temperature profiles for IN and OUT radial legs (method I).

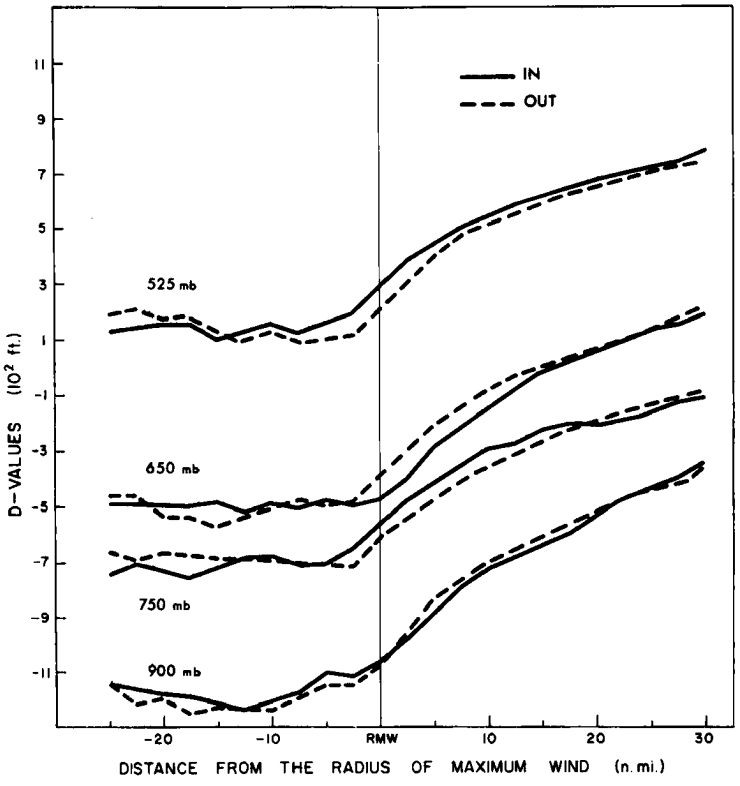

Fig. A5. Composited D-value profiles for IN and OUT radial legs (method I).

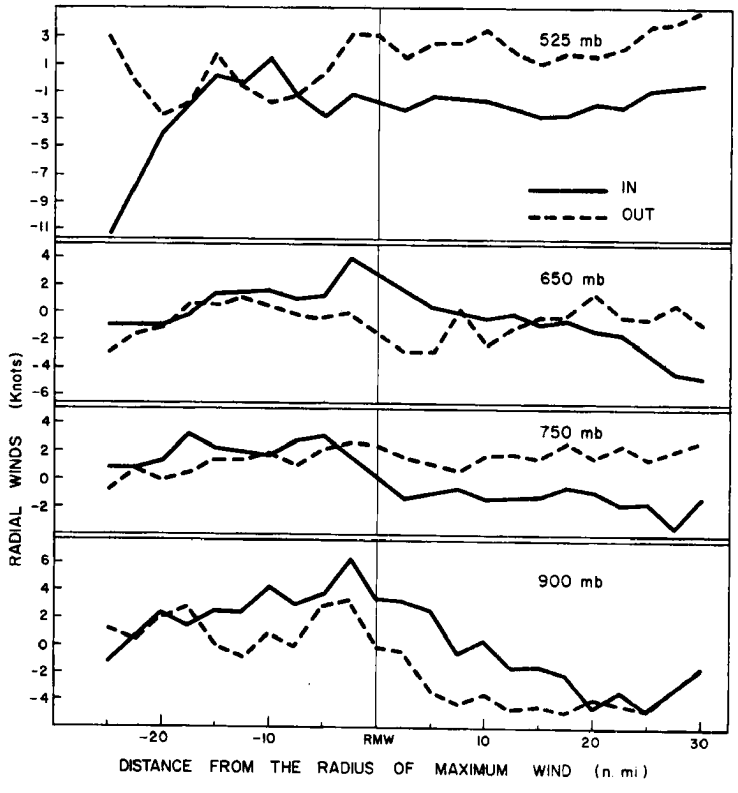

Fig. A6. Composited radial wind profiles for IN and OUT radial legs (method I).